Graduate Theses and Dissertations   Graduate School

January 2013

Modeling, Analysis and Control of Voltage-Source Converter in Microgrids and HVDC

Ling Xu
University of South Florida, lxu@mail.usf.edu

www.manaraa.com

Modeling, Analysis and Control of Voltage-Source Converter in Microgrids and HVDC

by

Ling Xu

A dissertation submitted in partial fulfillment
of the requirements for the degree of
Doctor of Philosophy
Department of Electrical Engineering
College of Engineering
University of South Florida

Major Professor: Lingling Fan, Ph.D.
Christos Ferekides, Ph.D.
Fangxing Li, Ph.D.
Zhixin Miao, Ph.D.
Lee (Elias) Stefanakos, Ph.D.
Yu Sun, Ph.D.

Date of Approval:
November 12, 2013

Keywords: Impedance model, Renewable energies, Resonance, Stability, VSC

Copyright © 2013, Ling Xu

DEDICATION

To my wife, my parents, my son, my friends and my teachers.

ACKNOWLEDGMENTS

There are many people I would like to express my thanks to during my Ph.D. studies. It is impossible to complete this dissertation without their support.

First of all, I would like to express my sincere gratitude to my advisor Dr. Lingling Fan for her guidance, training and support. The experience as her Ph.D. student is the most important and enjoyable part during my long years' study. The research facilities provided by the lab is an amazing treasure otherwise the dissertation is not possible to complete. She is always available to discuss the research issues and taught me how to become a researcher, which is the essential part of Ph.D. study.

Secondly, I would like to thank the rest of my committee members: Dr. Christos Ferekides, Dr. Fangxing Li, Dr. Lee (Elias) Stefanakos and Dr. Yu Sun, for their encouragement and constructive comments especially during my Ph.D. proposal. I also would like to express my sincere gratitude to Dr. Zhixin Miao for his unlimited help and guidance during my research and project work.

I owe my thanks to my colleagues from the smart grid power system lab: Yasser Wehbe, Lakanshan Prageeth Piyasinghe, Mohemmed Alhaider, Vahid Rasouli Disfani and Javad Khazaei, for the discussions, help and enjoyable atmosphere in the lab.

Last but not the least, I would like to thank my wife, Ying Liu, my parents, Qimao Xu, Huizhen Yin and my son Jason Xu for their endless love and support during my studies. Especially, I would like to thank my son's lovely smiling face which always encourages me to move forward.

TABLE OF CONTENTS

i

LIST OF TABLES

LIST OF FIGURES

viii

ABSTRACT

The objective of this dissertation is to carry out dynamic modeling, analysis and control for Voltage-Source Converters (VSC). Two major applications of VSC will be investigated in this dissertation: microgrid application and High Voltage Direct Current (HVDC) application.

In microgrid applications, VSC is used to integrate distributed energy sources such as battery and provide system functions: such as real and reactive power regulation, voltage and frequency support during islanding condition, and abnormal system condition mitigation. In HVDC applications, VSC is used to interconnect dc systems with ac systems. The functions supplied by VSC are similar to that in microgrids. However, the transfer capability and stability in such kind of system are of major interests.

Therefore, Part I of this dissertation focuses on VSC's applications in microgrids. A battery's inverter can be operated in both grid-connected PQ regulation mode and voltage and frequency support mode during islanding condition. Transition scheme between these two control modes is firstly investigated to guarantee a smooth dynamic performance. Secondly, a coordinated control strategy between battery's and PV station's VSCs is developed to improve microgrid's power flow. Thirdly, power quality improvement through the battery's inverter is investigated. VSC's control and capability for microgrid operation at normal, transient, and abnormal conditions will be modeled and analyzed.

Part II of this dissertation focuses on VSC's applications in HVDC. The following topics are investigated in this dissertation: (i) how to design VSC-HVDC's controller using system identification method? (ii) How to coordinate VSCs in multi-terminal HVDC scenarios? And (iii) how to determine VSC-HVDC system's transfer capability based on stability limits? High-fidelity simulation technology is employed to tackle control validation while frequency domain impedance modeling technique is employed to develop analytical models for the systems. With linear system analysis

x

tools such as Nyquist plots and Bode plots, stability limits and impacting factors of VSC-HVDC systems can be identified.

This dissertation led to four journal papers (two accepted, one request of revision, one to submit) and five conference papers. The major contributions of this dissertation include: 1) Developed VSC and microgrid models in high-fidelity simulation environment. Developed and validated VSC control schemes for variety of microgrid operations: normal, abnormal, and transient. The developed technologies can facilitate a battery to make up solar power, improve system dynamic performance during transients, and improve power quality. 2) Developed VSC-HVDC simulation models, including two-terminal HVDC and multi-terminal HVDC. Developed VSC-HVDC control schemes for two-terminal and multi-terminal systems. Developed analytical impedance models for VSC-HVDC systems and successfully carried out stability limit identification.

CHAPTER 1

INTRODUCTION

1.1 Background

Due to the development in power electronics industry, the capacity and switching speed of Insulated-Gate Bipolar Transistors (IGBTs) have been improved. IGBTs now meet the requirements of high power industry. The switching of IGBTs is controlled by gate voltage, and does not require external circuit to turn off. This advantage makes the IGBTs a suitable choice to regulate ac and dc networks without any complicated turn-off control circuit like the thyristors. Since the dc voltage of IGBTs is controllable via proper switching on gate, and a capacitor is usually parallel connected at the dc side which makes the dc voltage stable, the converter consists of IGBTs is normally known as Voltage-Source Converters(VSC).

The VSC discussed in this dissertation normally consists of six IGBTs, which form a three-phase ac to dc converter. Fig. 1.1 presents a common three-phase ac/dc converter using IGBTs. Since each IGBT has a reverse parallel diode, the current has the capability to flow back and forth between ac and dc side. Therefore, the VSC could either operate as a rectifier or an inverter without any topology change. Proper control algorithms are needed to be designed to make it possible.

Renewable energies such as wind, solar and fuel cell require advanced integration technologies. Unlike traditional energy resources such as gas, coal and oil, the output of renewable energies depends on various factors including wind speed, sunlight irradiance and temperature. Hence, power generated from renewable energies is not constant and varies from time to time, which is a big challenge from a power system operator's view. Moreover, the output of solar and fuel cell energies are normally dc power, which is not compatible with an ac power system. However, thanks to the development of power electronics technology, it is now a preferred solution to utilize VSC to

1
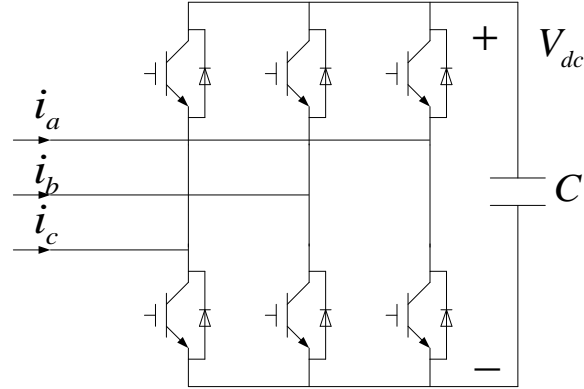
Figure 1.1. Configuration of a three-phase ac/dc converter.

integrate those renewable energies into power system. Due to high freedom control capabilities of VSC, wind, solar and fuel cell energies could be integrated into power system via proper back to back, or dc/ac converters.

In order to coordinate with time variant renewable energies and make power supply reliable, energy storage devices need to be installed along with renewable energies. Traditional energy storage technology including water pumping which requires high investment and is limited by geographic conditions. Battery and super capacitor are two growing solutions to store energy for power grids. Both need VSC to interface with power system. Since the output of a battery and a super capacitor are both dc power, a dc/ac inverter is required to connect them with ac grids.

Another benefit from VSC is the passive network supply capability, which is critical for microgrid applications. Microgrid is usually supplied by several distributed generations whose power capacity is relative low. A tie between a microgrid and the main ac grid is the major support for voltage and frequency. In case the tie is cut off due to any severe fault, the microgrid may loss voltage and frequency stability. However, if the VSC has proper controller designed, it will be able to switch from power control to voltage and frequency control. The microgrid can still operate stably.

The full controllability of VSC is also valuable for long distance high power transmission. For the integration of offshore wind farms, the loss on ac transmission is very high and the onshore terminal voltage may drop dramatically, which makes the integration with grid impossible. The underwater dc transmission is very efficient comparing to ac transmission. The VSC could control

2

the power transmission from wind farm and compensate reactive power, which secures the power system.

The dissertation will focus on the various applications of VSC on renewable energies, energy storage and power transmissions. The proper control algorithms for each application will be analyzed and designed. Computer simulations conducting in PSCAD/EMTDC and MATLAB/SimPowerSystems will be implemented and verify the proposed controllers.

In order to identify power transfer capability, detailed analysis including impedance modeling of VSC will be conducted and the stability and resonance issues will be addressed.

1.2   Statement of the Problem

The dissertation focuses on the applications of VSC for renewable energies including microgrid and VSC-HVDC. The following challenges are studied.

First, renewable energies such as wind, solar can be integrated into the system via VSC, which can also form a microgrid. Due to the intermittence of renewable energies, a storage device like battery has to be installed to improve the microgrid operation. The respective control strategy is designed. Additionally, a control algorithm is needed to optimally coordinate the battery and renewable energy in order to improve the reliability of microgrid. The islanding operation mode of microgrid is also studied.

Second, the power quality of microgrid is a critical issue for the customers since the system usually has unbalanced load and uncontrolled power electronics devices. To improve the power quality such as mitigate the negative sequence and low order harmonic currents with lowest cost is an urgent need of the customer and utilities companies.

Third, another application of VSC, VSC-HVDC, is more complicated and more critical for grid security since it is dealing with high voltage system. The controller design and parameters tuning is complicated and time consuming. Finding an efficient approach to determine the controller parameters with desired system performance is valuable for the system designer.

3

Fourth, offshore wind farms integration is a big challenge for the utility. Multi-terminal VSC-HVDC topology is a suitable solution, however, the power flow between each station and the fault ride through capability have to be addressed.

Fifth, the inherent cause of stability and resonance issues of VSC-HVDC is a key point which can help engineers understand the inside of the system. Since the system is hybrid which includes both ac and dc part, the analysis has to be take both side into account.

1.3   Approach

The controller design and analysis of system needs the application of control theory. The models designed within this dissertation are built in details which means the dynamics of the power electronics devices are included.

Two time-domain Electro-Magnetic Transients programs are adopted to build and verify the models, which are PSCAD/EMTDC and MATLAB/SimPowerSystem. Both tools are able to simulate the transients of power electronics devices during switching so the model is more accurate and more closer to the actual system than average models. PSCAD/EMTDC is a standard tool in power engineering industry and is widely used in utility companies and academia. The results tested with this tool is widely accepted and can be considered consistent with the real system. MATLAB/SimPowerSystem not only has detailed power electronics models but also has more specific toolboxes for controller design, such as the system identification toolbox. The controller design with MATLAB environment is friendly and is more powerful. Therefore, the combination of those two tools can facilitate the research in this dissertation.

Depending on the system complexity, the simulations conducted in PSCAD/EMTDC and MATLAB/SimPowerSystem can take very long time and sometimes may exceed the system capability due to the limit of memory. A Real-Time Digital Simulator (RT-LAB) is used to overcome the limitations. RT-LAB is a powerful super computer with fast processors and large memories, so it can handle very large power system and detailed power electronics models. FPGA is utilized in the system to manage the I/O between RT-LAB and other equipments, so that the simulation can

4

run in real-time. This feature is very favorable for large system simulation such as the studies in this dissertation.

1.4   Outline of the Dissertation

The structure of the dissertation is organized as follows.

Chapter 1 gives a brief introduction of the research issues including background information, statement of problem, and approach adopted in this dissertation.

Chapter 2 presents a detailed literature survey on the applications of VSC in renewable energies integration, which includes microgrid and VSC-HVDC. The various controllers for VSC are introduced, and the technical challenges in microgrid and VSC-HVDC's applications are also presented.

The dissertation can be divided into two parts. Chapter 3 to 5 is the first part which investigates the applications in microgrid.

Chapter 3 develops a control strategies for a battery system to improve operation of a microgrid. The control strategies will not only provide system requirements but also take safe operation of a battery into consideration. A comprehensive model for a microgrid without synchronous generators, with a battery system, an induction machine and passive loads will be built in PSCAD/EMTDC. Control strategies will be developed and verified through simulation studies.

Chapter 4 studies the control strategies for a microgrid with both a battery group and a PV array. The study approach is detailed model based simulation. The focus of this chapter is control strategies at the autonomous mode. In this chapter, the research is expanded to include a PV array in the microgrid. Coordination among different DERs will be taken into consideration.

Chapter 5 develops a control strategy for the inverter of a battery to compensate unbalanced and harmonic currents under various grid voltage conditions for a microgrid. A PR controller and HC controllers for specific order of harmonic currents are designed and tested under different cases, in which the grid voltage has different level of unbalanced component. The case studied in RT-LAB shows the battery inverter can successfully compensate unbalanced and odd harmonic currents when the grid voltage has 0.5% and 2% negative sequence component.

5

The second part of this dissertation is Chapter 6 to 9, which presents the research in HVDC's applications.

Chapter 6 proposes to use MATLAB system identification toolbox to identify the open-loop system model for dc-link voltage control design for VSC-HVDC system. The d-axis current reference is treated as the input while the dc-link voltage is treated as the output. With the simplified linear model determined from the toolbox, a dc-link voltage controller's parameters can be determined accurately. Simulation results indicate that the identified model is accurate and the controller could meet the performance requirements.

Chapter 7 investigates the modeling and simulation of a four terminal VSC-HVDC system under both normal and fault scenarios. The Multi-terminal HVDC (MHVDC) system includes two DFIG wind farms. The control strategies of both wind farm side converter (WFVSC) and grid side converter (GSVSC) are described. Simulations of the system are carried out in a Real-Time digital simulator RT-LAB. The system response under grid side ground fault is also studied, and an approach to mitigate the over-voltage during fault is proposed and tested.

Chapter 8 investigates the resonance stability of VSC-HVDC system at ac side (the rectifier side ac grid and the inverter side ac grid). Typical VSC-HVDC is adopted and impedance models of the systems is developed with the inner and outer converter control loops included. Nyquist stability criterion and impedance frequency responses is then be applied to detect resonances. Impacting factors on stability such as feed-forward filter structure, line length and power transfer levels are identified.

Chapter 9 investigates the dc resonance issues for a two-terminal VSC-HVDC system. Typical VSC-HVDC controls and a practical dc transmission line is adopted. Frequency domain analysis is applied to examine the characteristics of the derived dc impedance models. The models are verified by comparing with the frequency responses obtained from detailed VSC-HVDC system simulations in a real-time digital simulator. Real-time digital simulations are also used to validate the dc resonance analysis on the impact of dc capacitor and power transfer levels.

Chapter 10 summarizes the research conclusions of this dissertation and proposes some suggestions for the future work.

CHAPTER 2

REVIEW OF RELEVANT LITERATURE AND RESEARCH

2.1 VSC Control

The VSC controls have been extensively studied in the literature, the most popular and mature control methodology is call nested loop dq current control [1, 2]. There are some other control schemes including Direct Power Control [3] and Sliding Mode Control [4]. The various control algorithms will be described briefly as follows:

1. Conventional dq Control. The classical control algorithm for VSC is based on the nested loop dq control scheme, which normally includes a outer control loop, either power control or dc voltage control, and an inner current control loop [1]. Fig. 2.1 demonstrates the conventional dq control algorithm. In which, the outer loop controls the active power and ac voltage while the inner loop controls the dq currents. A frame of reference transformation is required for this control. The ac voltages and currents are first transformed into dq quantities via Park's transformation, and the outer control loop generates the respective dq current references depending on the control objectives. The inner current control loop regulates the dq currents and generate the appropriate switching pulses for converters.

2. Direct Power Control. The Direct Power Control(DPC) eliminates the current control loop and regulates the active and reactive power directly [3, 5, 6, 7, 8]. Fig. 2.2 depicts the configuration of a Direct Power Controller, where the active power command is provided by a dc-bus voltage control block and the reactive power command is directly given. The errors between commands and feedback powers are input to the hysteresis comparators and digitized to the signals S_p and S_q. The phase of the power source voltage is also digitized to the signal θ_n. S_p, S_q and θ_n are the input to a switching table and generate appropriate

7
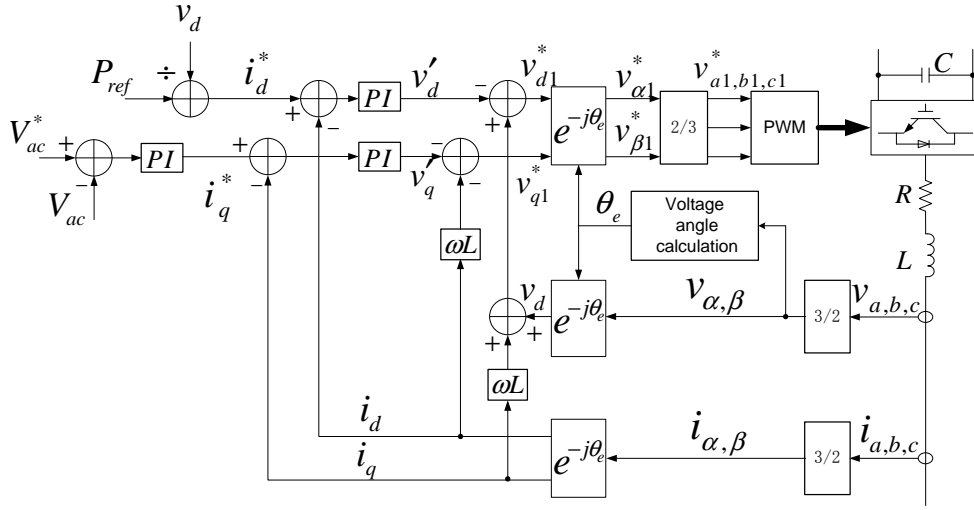
Figure 2.1. Conventional dq control for a VSC.

switching signals to converters. The advantage of DPC is its simple structure and direct control capability of powers. The controller is easy to be implemented.

3. Sliding Mode Control. Comparing to conventional PI control, the Sliding Mode Control(SMC) does not need an accurate mathematical model of the objective to be controlled, but offers better stability regardless the plant parameters and load variations [9, 10, 4, 11]. Fig. 2.3 demonstrates a Sliding Mode Controller for a boost inverter. The SMC first needs to select appropriate state variables, and the input current i_{L1} and output voltage V_1 are selected. ϵ_1 and ϵ_2 are the state variable errors of i_{L1} and V_1, which forms a sliding surface equation

$$S(i_{L1}, V_1) = K_1 \varepsilon_1 + K_2 \varepsilon_2 = 0 \tag{2.1}$$

The value is input to a hysteresis block H_1 and generate the switching signals S_1 and S_2.

2.2 VSC Applications

VSC has various applications in microgrid and HVDC fields, which will be discussed as follows.

8
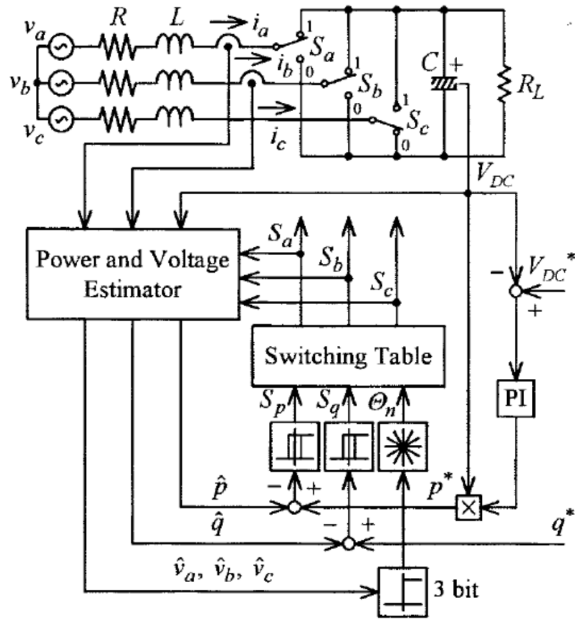
Figure 2.2. Configuration of Direct Power Controller [3].
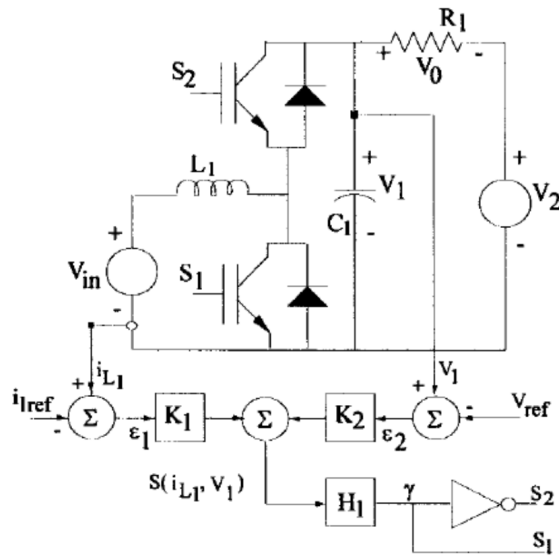
Figure 2.3. Configuration of Sliding Mode Controller [9].

9

2.2.1 Microgrid Applications

2.2.1.1 VSC Interfaced Battery

Microgrid is an important technology to integrate distributed energy resources, including wind turbines, solar photovoltaic panels and energy storage devices such as battery [12, 13, 14, 15, 16]. A microgrid can either operate at the grid connected or autonomous modes [17, 18].

At autonomous modes, voltage and frequency should be supported by a microgrid itself, usually through synchronous generators. For a microgrid without synchronous generators, the system voltage and frequency would be difficult to maintain without the support of the ac grid. One solution is to use a VSC controlled by a pulse width modulation (PWM) scheme to provide voltage and frequency control [19]. A battery is interconnected to a grid through a VSC and hence batteries can improve the operation of microgrids through VSC control. In [19, 20, 21], battery systems are applied to restore system voltage and frequency quickly (several cycles). In practice, applications of battery storage system for grid frequency regulation have been deployed in [22], the maximum capacity has reached 20MW.

For microgrids operating at grid-connected modes, VSCs of battery systems can work at power control mode. Depending on the state of charge (SOC) of battery and active power requirement by the microgrid, a battery may operate at either charging or discharging condition. The VSC connected between the battery and the microgrid regulates power flow only and does not participate in system frequency control. In [23] and [24], applications of battery energy storage systems in grid power balance at grid-connected modes are demonstrated.

Research work has been conducted on development of control strategies for batteries in microgrids [17, 18, 19]. An ideal dc voltage source is assumed for a battery. In reality, a battery has operation limits. For example, the SOC cannot be lower than a threshold; the Depth of Discharge (DOD) may affect the life time of a battery [22]. Therefore, there is a need to model a battery adequately and develop control strategies based on the adequate battery model with battery status information collected.

10

Detailed battery models have been developed in the literature. In [25], a battery model is described by partial differential equations. [13] adopted the same model to simulate a wind farm with a Lead-acid battery system. From [22], a Li-ion battery has been a suitable choice for high power application due to breakthroughs on materials. Reference [26] describes a detailed Li-ion battery model with parameters and has verified the validity through experiments. Though the battery studied in [26] is for a low voltage level, serial and parallel connections could make a high voltage and high power battery matrix possible, which could be used in power system [27].

2.2.1.2 VSC Interfaced PV Station

PV model has been investigated thoroughly in the literature. The current source and anti-parallel diode model has been proved to be able to simulate the V-I characteristics of a solar cell accurately. For the PV and battery combined systems, [28] proposed a power management mechanism that could optimize the power flow. [29] utilizes batteries to reduce the fluctuations of PV output. [30] presents the power scheduling within PV and battery system from the power system's point of view. Besides the PV and battery combined system, PV and capacitor combined system is also examined by [31, 32, 33]. Capacitors are also could be used to reduce the power fluctuation of PV, or participate in frequency control.

2.2.1.3 Harmonics Reduction with VSC

Harmonic currents due to power electronics switching have been widely investigated in the literature. Active filter is a mature solution to mitigate the harmonic currents [34, 35, 36, 37]. The current control strategies are discussed and compared in [38], which include linear current control, digital deadbeat control and hysteresis control. The linear current control utilizing dq synchronous frame control has been proposed and tested [34, 35, 39, 40]. Another control method developed in [40, 41] is called Proportional-Resonant (PR) controller. With PR control theory, the complexity of harmonic current control system can be effectively reduced for both positive and negative sequences. Uncontrolled power electronics devices with load can produce non-negligible low orders harmonic currents to microgrid. In [42], even small percentage of grid voltage unbalance

11

would lead to additional high 3rd order harmonic currents from rectifiers. In order to eliminate the harmonic currents, a appropriate control strategy has to be developed.

2.2.2 VSC-HVDC Applications

2.2.2.1 LCC-HVDC vs VSC-HVDC

The first modern commercial HVDC transmission project was built between Gotland and mainland Sweden in 1954 [43]. The power capacity was 10-20 MW, and was constructed based on Thyristor-based line-commutated converters (LCC), which require external circuit to force the current to zero and turn them off. The technology is mature and widely used nowadays. LCC-HVDC is suitable for long distance bulk power transmission since the major LCC valves, thyristors, are reliable and with high power capability. The longest HVDC project reported is the Xiangjiaba-Shanghai 2,071 km (1,287 mi) 6400 MW link connecting the Xiangjiaba Dam to Shanghai, in China [44].

The VSC-HVDC was introduced when high power IGBTs were available for use. The advantage of a VSC-HVDC comparing to LCC-HVDC include: much less harmonics thus large size filters are not required; reactive power supply capability; and multi-terminal applications. The IGBT could turn on or off depends on the voltage signal applied on the gate port, thus the PWM is utilized to control the converters. Therefore, the magnitude and phase of the output voltage are both fully controllable. Therefore, VSC could compensate reactive power to the grid, to support ac voltage stability. Due to the fully controllability of output voltage, the power flow within VSC-HVDC is fully controllable as well, which enables flexible power flows between grids. Since there is no ac voltage source required to operate like the LCC HVDC does, the VSC-HVDC could support passive network, which is ideal for remote loads and renewable energies integration. An undergoing VSC-HVDC project is the 165 km, ±320 kV and 800 MW connection between DolWin Alpha and Dörpen/West in Germany [45].

The comparison of LCC-HVDC and VSC-HVDC is listed in Table 2.1.

12

Table 2.1. Comparison of LCC-HVDC and VSC-HVDC

	LCC-HVDC	VSC-HVDC
Converter Technology	Thyristor based	IGBT based
Voltage Polarity	Both	Does not change
Current Direction	Does not change	Both
Turn On	Controllable	Controllable
Turn Off	Rely on external circuit	Controllable
Power Capacity	Higher	Lower
ac System Requirement	Strong	Strong and weak
Reactive Power Requirement	Yes	No
Station Losses	Lower	Higher
Cost	Lower	Higher
Reliability	Higher	Lower
Technology	More mature	Less mature

2.2.2.2 Multi-terminal VSC-HVDC

One of the advantages of VSC-HVDC transmission is the multi-terminal topology, which is easy to be implemented. This feature could benefit the grid integration of offshore wind farms, since the physical distance of each wind farm could be far and the grid integration station may have only few choices. The multi-terminal VSC-HVDC system could integrate several wind farms to one or multiple grid side converter stations, which provides high flexibility for power planning and construction [46, 47].

Depending on the topology of multi-terminal VSC-HVDC, the control objective of each converter station varies. When the multi-terminal VSC-HVDC is used to integrate offshore wind farms to grid, the rectifier stations usually operates in passive network support mode, i.e., the magnitude and frequency of ac output voltage of the converters will be controlled. Regarding the inverter station that connecting to the ac grid, the major control objective is to regulate the dc voltage, which ensures the active power generated from wind farms could be delivered to the grid to maintain power balance. In the case of multiple inverter stations, power droop control strategy should be implemented to dispatch the active power to each station.

13

In the case of connecting between grids instead of integrating wind farms, the rectifier stations usually operate in power control mode, which regulate active and reactive power transfer. However, the inverter stations work in the same mode: dc voltage control mode.

Operation of multi-terminal VSC-HVDC (MHVDC) has appeared in the literature. E.g., [48] described the operation of a MHVDCs operation when one of the inverters is lost. The dc voltage will have a spike which can cause damage to power electronic devices. Fast blocking rectifiers and following up with a power balancing scheme among the rest of the converters will solve the problem.

MHVDC has also been proposed to deliver wind power. In [49], a multi-terminal VSC-HVDC system is proposed to integrate synchronous generator based offshore wind farms. The generator side converter control keeps the ac voltage constant and regulates the dc current based on wind speed. In [50], a four terminal MHVDC with two rectifier converters and two inverters is modeled in MATLAB/SimPowersystems. The control modes of the converters are described and tested for wind speed change in the paper. [51] presents two three-terminal MHVDC topology, control and normal system operation. System responses under fault scenarios have not been investigated.

2.2.2.3   VSC-HVDC Modeling

Several methods to derive the VSC model have been developed including averaging circuit analysis, small signal analysis and computer aid system identification. [52, 53, 54, 55] derived the VSC models based on averaging methods. The nonlinear IGBT switches are modeled as averaged voltage source, which are applied in the KVL and KCL equations while plugging in other system parameters. [56, 57] obtained the VSC-HVDC model via small signal analysis. A set of linearized fundamental converter equations was developed and combined with other system components, an eigenvalue analysis was conducted to determine the stability limitations. [58] obtained a transfer function representation of a fuel cell with its converter. The authors applied a step change on load and recorded the response on output voltage of fuel cell. The results were imported to MATLAB/Simulink System Identification Toolbox and a transfer function between load current and fuel cell voltage was estimated via various estimation algorithms. [59, 60, 61] proposed similar approaches to estimate a model representation of dc-dc converters.

14
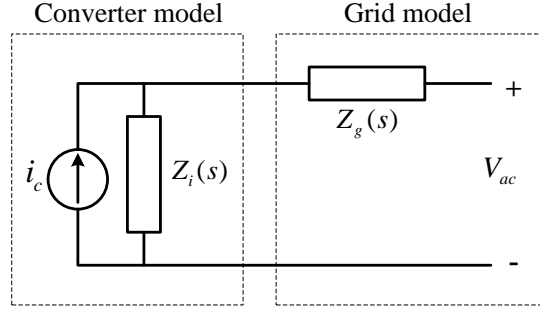
Figure 2.4. Impedance model of VSC and grid.

In order to study the stability issues of VSC, [62] developed an impedance model of VSC between wind turbines and the grid, which also included the detail modeling of Phase Lock Loop (PLL). An active damping controller was proposed to eliminate the resonance at 3rd and 4th harmonics. The approach Sun used [62] was to derive an impedance model of VSC with its respectively controller, which is called $Z_p(s)$ and $Z_n(s)$ corresponding to the positive and negative components. The grid is represented by a combination of voltage source and impedance called $Z_g(s)$. Fig. 2.4 shows the impedance model representation of VSC and grid. Nyquist criterion was applied to examine the stability of system based on $\frac{Z_g(s)}{Z_i(s)}$. [63] applied the similar technique to derive an impedance model and analyzed the stability issues.

Instead of using PLL, [64] proposed a power synchronization control to replace PLL, which avoids the instability caused by PLL especially in weak ac system condition. [65] investigated the models of VSC-HVDC connecting two very weak ac systems in detail. The model obtained which is called Jacobian transfer matrix has a Right-Half-Plane (RHP) zero that moves closer to the origin with larger load angles. Consequently, stability analysis was performed with the obtained model, and concluded that the RHP zero limits the bandwidth of VSC, which implies the converter stations shall not operate with too large load angles, and a higher dc capacitance is necessary to keep the dc voltage stable.

2.3   Summary

The dissertation has an opportunity to conduct research on the following issues since they have not been investigated in the literature.

1. Battery inverter control during microgrid transients

2. How to use battery inverter for power quality improvement in microgrids at distribution level

3. Comprehensive modeling of entire VSC-HVDC system (ac + dc modeling) to identify stability limits

<center>**CHAPTER 3**</center>

<center>**MODELING OF A MICROGRID WITH BATTERY CONNECTED**</center>

3.1 Introduction

In this chapter, the modeling of a microgrid with battery connected will be introduced [66].[1] Microgrid is an important technology to integrate distributed energy resources, including wind turbines, solar photovoltaic panels and energy storage devices such as battery [12, 13, 14, 15, 16]. A microgrid can either operate at the grid connected or autonomous modes [17, 18].

At autonomous modes, voltage and frequency should be supported by a microgrid itself, usually through synchronous generators. For a microgrid without synchronous generators, the system voltage and frequency would be difficult to maintain without the support of the ac grid. One solution is to use a VSC controlled by a PWM scheme to provide voltage and frequency control [19]. A battery is interconnected to a grid through a VSC and hence batteries can improve the operation of microgrids through VSC control. In [19, 20, 21], battery systems are applied to restore system voltage and frequency quickly (several cycles). In practice, applications of battery storage system for grid frequency regulation have been deployed in [22], the maximum capacity has reached 20MW.

For microgrids operating at grid-connected modes, VSCs of battery systems can work at power control mode. Depending on the SOC of battery and active power requirement by the microgrid, a battery may operate at either charging or discharging condition. The VSC connected between the battery and the microgrid regulates power flow only and does not participate in system frequency control. In [23] and [24], applications of battery energy storage systems in grid power balance at grid-connected modes are demonstrated.

---

[1]This chapter was published in Power and Energy Society General Meeting, 2012 IEEE, vol., no., pp.1,8, 22-26 July 2012. Permission is included in Appendix B.

<center>17</center>

Research work has been conducted on development of control strategies for batteries in micro-grids [17, 18, 19]. An ideal dc voltage source is assumed for a battery. In reality, a battery has operation limits. For example, the SOC cannot be lower than a threshold; the DOD may affect the life time of a battery [22]. Therefore, there is a need to model a battery adequately and develop control strategies based on the adequate battery model with battery status information collected.

Detailed battery models have been developed in the literature. In [25], a battery model is described by partial differential equations. [13] adopted the same model to simulate a wind farm with a Lead-acid battery system. From [22], a Li-ion battery has been a suitable choice for high power application due to breakthroughs on materials. Reference [26] describes a detailed Li-ion battery model with parameters and has verified the validity through experiments. Though the battery studied in [26] is for a low voltage level, serial and parallel connections could make a high voltage and high power battery matrix possible, which could be used in power system [27].

The objective of this chapter is to develop control strategies for a battery system to improve operation of a microgrid. The control strategies will not only provide system requirements but also take safe operation of a battery into consideration. A comprehensive model for a microgrid without synchronous generators, with a battery system, an induction machine and passive loads will be built in PSCAD/EMTDC. Control strategies will be developed and verified through simulation studies.

3.2 A Microgrid With a Battery and an Induction Generator

3.2.1 System Topology

This chapter investigates a microgrid consisting of two distributed energy resources (DERs). One is an induction generator driven by a bio-diesel machine (12 MW) and the other one is a battery (2 MWh). A strong ac grid is feeding the microgrid via a 69/13.8 kV transformer.

Three passive RLC loads are put into the microgrid to simulate the customer power consumption. Load 1 is located at Bus A close to the grid-connected transformer. Load 2 is located at the site of a diesel engine induction generator. Load 3 is connected at the output terminal of the battery system. Two 13.8 kV distribution lines based on the IEEE Standard 399-1997 [67] are also included in the model. The topology of the study system is shown in Fig. 3.1.

18
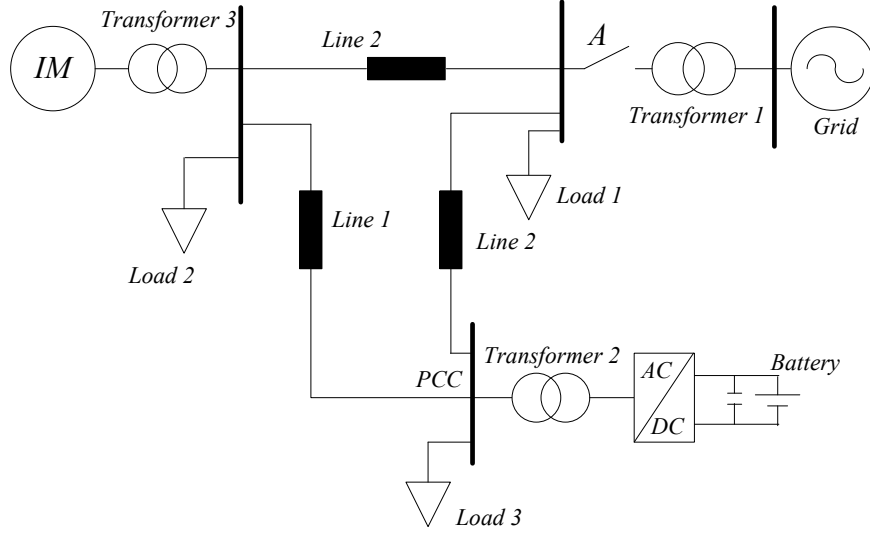
Figure 3.1. A microgrid with a battery system.

The study system is built in PSCAD/EMTDC. The battery system is modeled in detail. It consists of two battery groups in series, and each group has an open circuit dc voltage at 4.1kV. The peak active power output is 2MW for each group, and the capacity is 240Ahr, which implies that each battery group could inject a maximum 2 MW into the microgrid for 30 minutes.

The system parameters are listed in Table 3.1. At the grid-connected mode, the induction machine generates 8.9 MW active power, while the active power output command of the battery system is 0 MW. The microgrid absorbs 0.8MW active power from the main grid. At the autonomous mode, the battery system is expected to deliver 0.8MW to the microgrid since the supply from the main grid now is lost. The adjustment of active and reactive power generation from the battery will be achieved through inverter control.

3.2.2 Battery Model

The battery model includes two parts based on [26]. One part is the energy model and the other part is the circuit model as shown in Fig. 3.2.

The resistors and capacitors in the circuit model are used to emulate the dynamic responses of a battery. The parameters of the battery model have been verified through experimental results [26]. However, the battery model of [26] has a low voltage (4.1V) and small capacity (850mAhr).

19

Table 3.1. Simulation system parameters

Quantity	Value
ac grid voltage	69kV (L-L RMS)
Transformer 1	13.8kV/69kV, 20MVA, leakage 8%pu
Transformer 2	13.8kV/3.3kV, 10MVA, leakage 10%pu
Load 1	2.521MW+0.831MVar at 13.8kV
Load 2	4.994MW+1.029MVar at 13.8kV
Load 3	2.5MW+0.822MVar at 13.8kV
Distribution line 1	980ft, (0.044+j0.0359)ohm
Distribution line 2	1187ft, (0.052+j0.0436)ohm
Distribution line 3	1187ft, (0.052+j0.0436)ohm

Table 3.2. Induction machine parameters

Quantity	Value
Rated RMS phase voltage	8kV
Rated RMS phase current	0.5kA
Base angular frequency	60Hz
Stator resistance	0.066pu
First cage resistance	0.298pu
Second cage resistance	0.018pu
Stator unsaturated leakage reactance	0.046pu
Unsaturated magnetizing reactance	3.86pu
Rotor unsaturated mutual reactance	0.122pu
Second cage unsaturated reactance	0.105pu
Polar moment of inertia	1.0s
Mechanical damping	0.0001pu

20

For the battery used in the study system, we assume each battery group is constructed by 1000 individual pieces connected in series, and 70 in parallel. The voltage and current balance problems are neglected for the battery matrix. The total dc voltage from one battery group is 4.1kV and the total capacity is 240Ahr.

Fig. 3.2 shows the battery model [26].
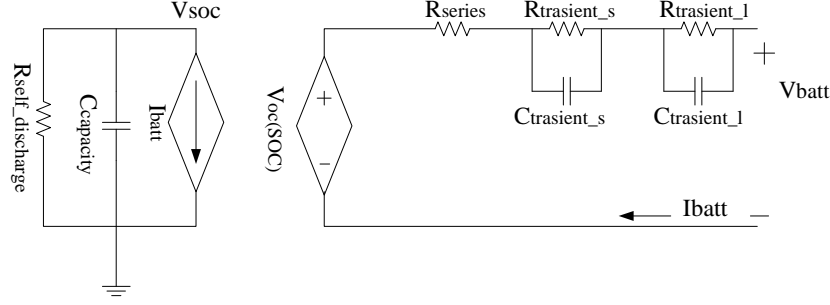
Figure 3.2. A detailed battery model [26].

Equation 3.1 gives the current and voltage relationship for the battery life time model, which is the left part in Fig. 3.2.

$$C_{capacity}\frac{dV_{soc}}{dt} + \frac{V_{soc}}{R_{self\_discharge}} + I_{batt} = 0 \tag{3.1}$$

Normally, the self-discharge resistor is very large and could be neglected. Hence, equation (3.2) could be derived to express the relationship between the battery output current and the SOC.

$$V_{soc} = -\frac{1}{C_{capacity}}\int I_{batt}\,dt + V_{soc}(0) \tag{3.2}$$

By setting the initial value of $V_{soc}(0)$ equal to 1V or 0V, the battery is initialized to fully charged or fully discharged. And the output current of battery will then either charge or discharge the battery by varying the value of V_{soc} depending on the external conditions. The full-capacity capacitor $C_{capacity}$ is a function of the battery capacity, charging and discharging cycles, and temperature. The expression of $C_{capacity}$ is shown in equation 3.3.

$$C_{capacity} = 3600 \cdot C_{capacity} \cdot f_1(Cycle) \cdot f_1(Temp) \tag{3.3}$$

21

$C_{capacity}$ will decrease in a considerable long time range comparing to the simulation period in this chapter. Therefore, $C_{capacity}$ is assumed to be constant in this chapter.

The circuit in the right part of Fig. 3.2 describes the output voltage and current characteristics of the battery. The open circuit voltage V_{oc} is a function of SOC as follows [26]:

$$V_{oc} = -1.031 \cdot e^{-35 \cdot V_{soc}} + 3.685 + 0.2156 \cdot V_{soc}$$
$$-0.1178 \cdot V_{soc}^2 + 0.3201 \cdot V_{soc}^3 \tag{3.4}$$

Fig. 3.3 is the graphic representation of the relationship between the open-circuit voltage and the SOC. It is observed that the voltage would rise at charging mode and would decrease in discharging mode.
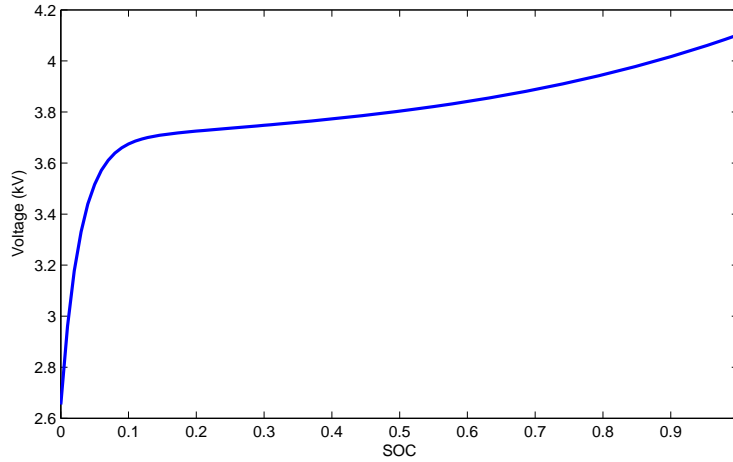
Figure 3.3. The relationship between open-circuit voltage and SOC [26].

$$\eta = \frac{\int_0^{discharge_end_time} v_b \cdot i_b \, dt}{\int_0^{charge_end_time} v_b \cdot i_b \, dt} \tag{3.5}$$

Another critical parameter of a battery is round trip efficiency, which is the ratio of the energy coming out from the battery and the energy that been charged into the battery. The round trip

22

efficiency can be calculated by equation (3.5), where v_b and i_b are the voltage and current measured at the battery dc terminal. Based on the curve in Fig. 3.4, the round trip efficiency is 98.14%. In Fig. 3.4, the charger dc voltage is 4.1kV, the source resistant R_s is 0.2ohm. Switch $S1$ is kept closed until SOC reaches 1. Once the SOC of the battery reaches 1, switch $S2$ will be closed, the load resistance is 8ohm.
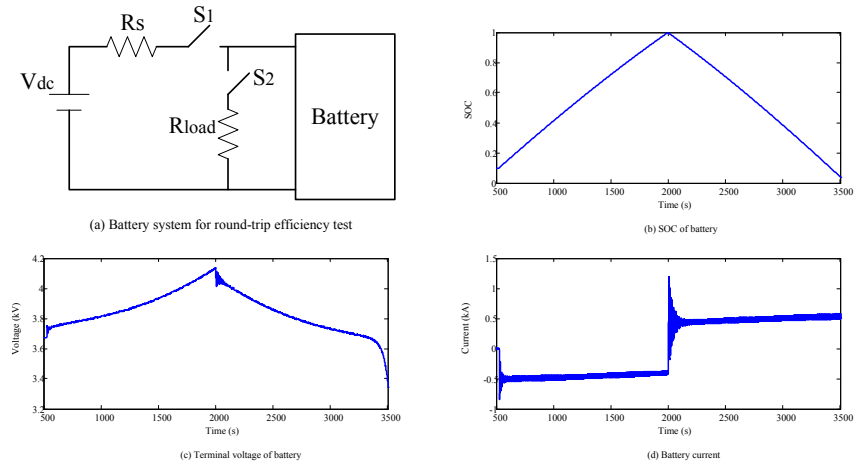
Figure 3.4. Part I: Round trip efficiency test of battery.

3.3 VSC Controls

Three control modes are considered for the battery: Power control, dc-link voltage control and voltage/frequency control. The former two modes can be used when the microgrid is grid-connected. The third control mode is applied when the microgrid is at its autonomous mode and there is no synchronous generator.

The control system of a VSC consists of two loops: inner current control loop and outer control loop. The outer control loop can be either active power control loop or dc-link voltage control loop when the microgrid is grid-connected. When the battery is supplying a standalone microgrid, the outer control loop will be switched to ac voltage and frequency control. The control loop diagram is presented in Fig. 3.6 and Fig. 3.8.

23

3.3.1 PQ Control and dc-link Voltage Control

Two charging or discharging strategies could be applied. One is constant dc-link voltage charging and the other is constant power charging. A decoupled d-q direct current control strategy has been developed in [2, 68]. Fig. 3.5 shows an equivalent model of a VSC inverter connected with ac sources.
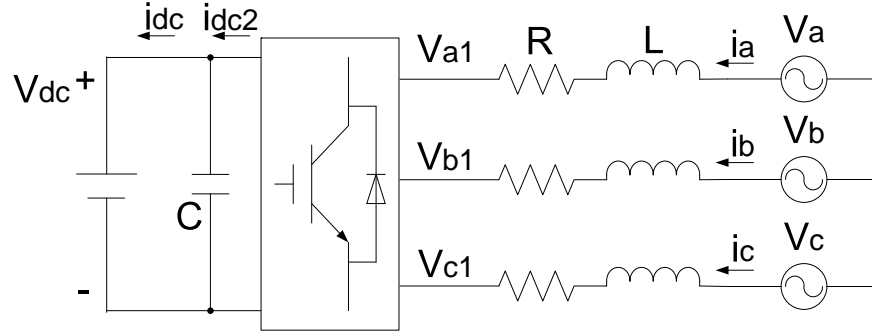
Figure 3.5. Equivalent model of a battery connected with ac sources.

Variables in the abc system in the above circuits can be transformed into a synchronous reference frame. The voltage and current relationship is shown in (3.6) and (3.7), where ω_s is the angular frequency of ac system, v_d, v_q, v_{d1}, and v_{q1} represent the d and q components of the point of common coupling (PCC) voltage (V_a, V_b, V_c)and VSC output voltage(V_{a1}, V_{b1}, V_{c1}), respectively, and i_d and i_q represent the d and q components of the current flowing between the ac system and the VSC.

$$v_{d1} = -(Ri_d + L\frac{di_d}{dt}) + \omega_s Li_q + v_d \tag{3.6}$$

$$v_{q1} = -(Ri_q + L\frac{di_q}{dt}) - \omega_s Li_d \tag{3.7}$$

The decoupled current control is shown in Fig. 3.6.

$$v_{dc}(C\frac{dv_{dc}}{dt} + i_{dc2}) = v_d i_d \rightarrow \frac{v_{dc}}{dt} = \frac{v_d i_d}{v_{dc}C} - \frac{i_{dc2}}{C} \tag{3.8}$$

24

dc voltage control is based on the balance of active power flow between the battery and the main grid as shown in (3.8). Apparently, the dc voltage can be regulated by the d axis current through a PI controller.

It is obvious from the relationship of the open-circuit voltage V_{oc} and SOC that the dc-link voltage tends to fall while the battery is discharging.

For constant power mode, the outer control loop will regulate the power. The only difference between a normal charging mode and a normal discharging mode is the power order is in different polarity.

In addition to the control strategy presented in Fig. 3.6, an upper level control scheme should be included to monitor SOC and protect the batteries. Fig. 3.7 shows the upper level control scheme, as long as the SOC is greater than minimal allowable value, the battery would continue operating at PQ mode. Otherwise, it should be disconnected, and more active power should be delivered from the main grid in order to keep power balance.
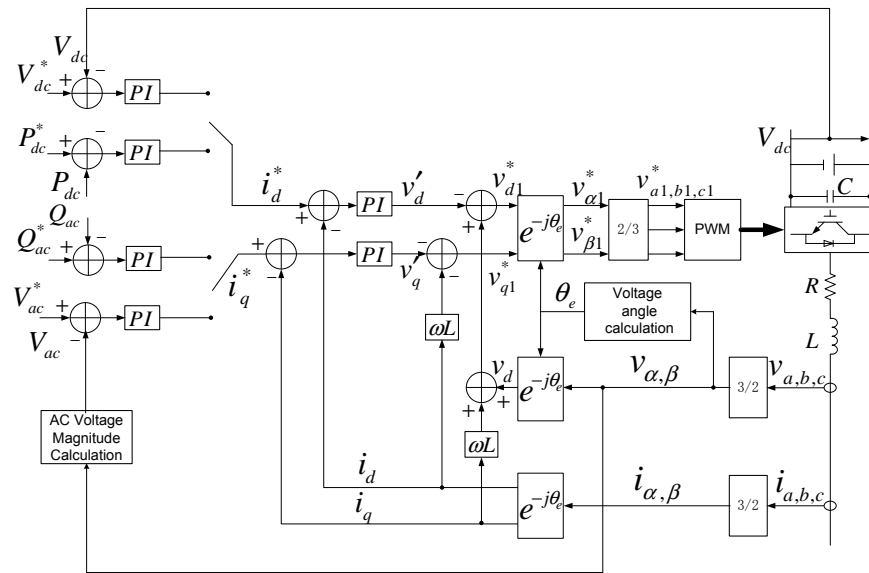
Figure 3.6. Normal charging and PQ control strategy.

Table 3.3. PI controller parameters of Fig. 3.6

	Kp	Ki
P control loop	2	10
Q control loop	2	10
dc voltage control loop	1	20
ac voltage control loop	1	20
Id control loop	1.5	100
Iq control loop	1.5	100
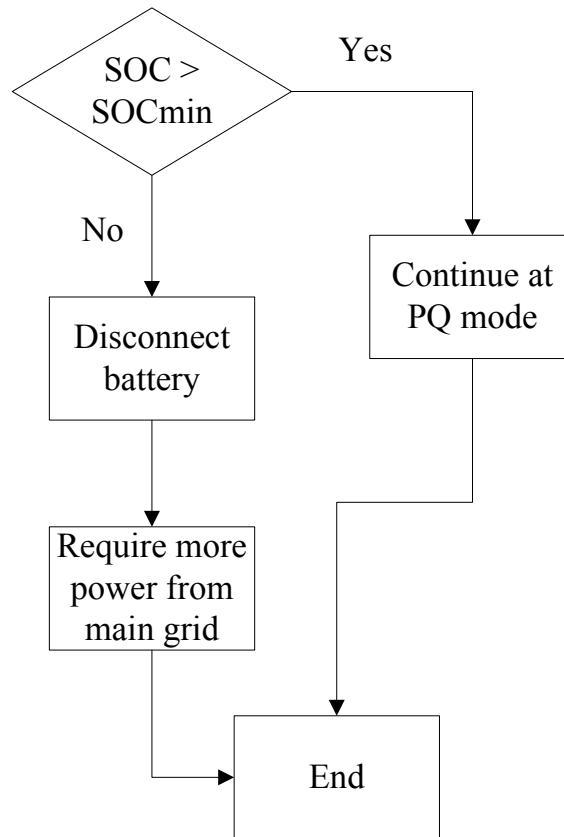
Figure 3.7. Upper level control considering SOC.

3.3.2 Voltage and Frequency Control

At autonomous modes, the microgrid is disconnected from the main ac grid and there is no synchronous generator to support system voltage and frequency. One advantage of VSC is its passive network supplying capability. In this study system, the VSC interfaced battery could support the microgrid's voltage and frequency by switching to ac voltage and frequency control. The basic control principles are based on decoupled current control [18, 69]. However, under steady-state and neglecting resistance R, (3.6) and (3.7) can be rewritten as (3.9) and (3.10) [20, 21]:

$$V_{d1} = \omega_s L I_q + V_d \tag{3.9}$$

$$V_{q1} = -\omega_s L I_d \tag{3.10}$$

PI controllers can be used to control the d and q axis components of the PCC voltage respectively. Fig. 3.8 depicts the ac voltage control strategy. The PCC three-phase voltages are measured and transformed into a $d-q$ reference frame, which is v_d and v_q in Fig. 3.8 respectively. Three-phase currents flowing between the loads and the inverter are measured and transformed to i_d and i_q respectively. With the comparisons of the dq voltages to their respective references, the resulting errors are sent to the PI controllers to generate the required output voltage of the VSC.
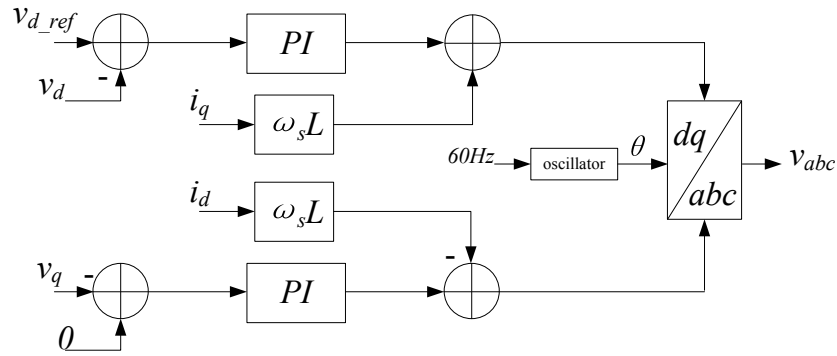
Figure 3.8. ac voltage control strategy of inverter.

The frequency of the ac voltage which supplies passive loads is also controlled by the VSC. An internal oscillator is used to generate the angle θ, which is used as the input of dq to abc

27

Table 3.4. PI controller parameters of Fig. 3.8

	Kp	Ki
Vd control loop	3	2
Vq control loop	3	10

transformation and ensures the frequency of output voltage is kept at 60Hz if PWM scheme applied [70].

A similar upper level SOC monitoring and battery protection scheme should be available when the batteries are working at islanding control mode. Fig. 3.9 shows the upper level control strategy at islanding modes. If the SOC is greater than the set point, the battery should operate at islanding mode and provide active power to the microgrid. Once the SOC reaches the pre-set point, the battery should be disconnected at the dc side to protect itself and the microgrid. The interfacing inverter can still work along with the dc link capacitor to provide a constant voltage with constant frequency. Once the battery is disconnected, there is no more active power could be injected into the microgrid. Therefore, in order to maintain stable frequency, load shedding is used to keep the active power balance.

3.4 System Evaluation in PSCAD/EMTDC

Simulation studies on the system in Fig. 3.1 are carried out in PSCAD/EMTDC. Two experiments are conducted to investigate not only the behaviors of batteries but also the overall system performance. The first experiment is to examine the power support capabilities of the battery with an ac grid connected. The second experiment investigates the system performance without any ac grid support. System voltage and frequency behaviors are analyzed.

One battery matrix consists of 7000 pieces of 4.1V small batteries, which form an equivalent battery of 4.1kV, 240Ah. Since the nominal voltage at ac side of inverter is 3.3kV, two battery matrixes in series are applied, which could supply 8.2kV at dc side.

28
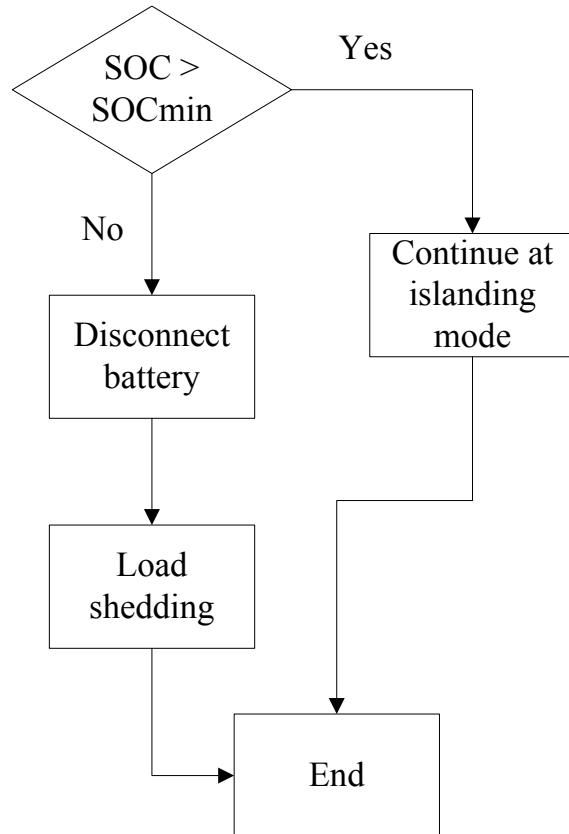
Figure 3.9. Upper level control scheme of islanding mode.

3.4.1 Power Support to the Microgrid from the Battery

In the first experiment, the study system in Fig. 3.1 is simulated at the grid-connected mode. The active power command of the battery system is to absorb 2MW before 10s, and then to send 0.5MW after 10s. At 15s, the active power command changes to absorbing 1MW.

Fig. 3.10 shows the active and reactive power delivered from the battery. The active power output is smooth and stable. The transition is fast and smooth. The reactive power reference is kept at 0 MVar. Variation in the reactive power is shown in Fig. 3.10(b). Fig. 3.10(c) shows the dynamic response of the battery current. Fig. 3.10(d) shows that the battery voltage decreases from 10s to 15s since the battery is sending out active power, while it is rising after 15s because of charging.
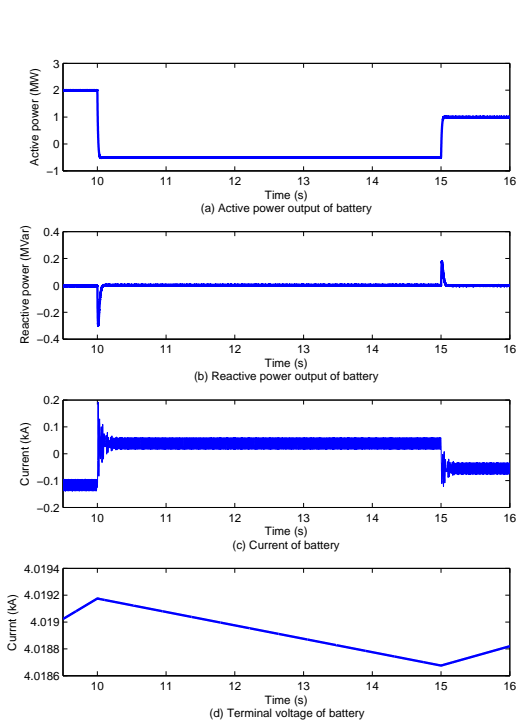
Figure 3.10. Performance of the battery at PQ mode.
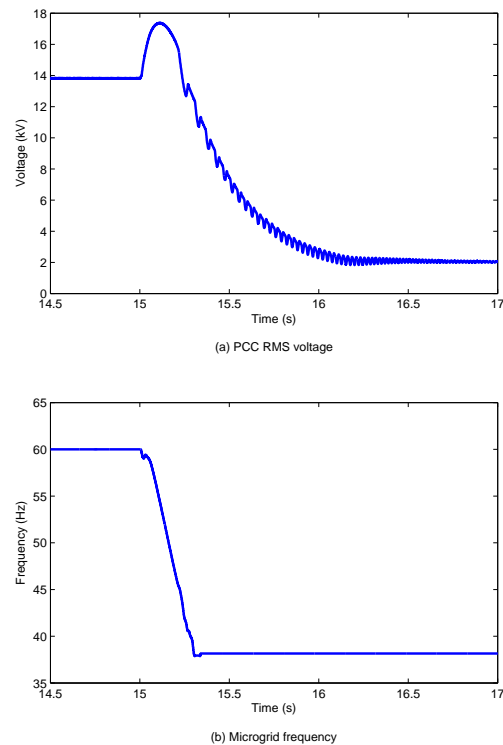
Figure 3.11. System behavior after islanding without control mode switching.

30

3.4.2 Voltage and Frequency Support to an Islanding Microgrid

When the microgrid loses its connection to an ac grid, the battery and its inverter system should switch to the ac voltage and frequency control mode as shown in Fig. 3.11. Without control mode switching, the frequency and the voltage of the microgrid will oscillate and lose stability. Fig. 3.11 illustrates the frequency and voltage responses following the grid disconnection at 15s without control scheme switch. The inverter still works at PQ control mode. The frequency and voltage oscillate dramatically and drop to a very low level. The microgrid can no longer operate.

Therefore, it is necessary for the inverter to transit to ac voltage and frequency control mode after an islanding event. Furthermore, since the battery is not an ideal dc voltage, the upper level control scheme in Fig. 3.9 should also be implemented.

3.4.2.1 During Islanding Transient Response

At 14.97s, the ac grid is disconnected by a switch to emulate the beginning of an islanding event of the microgrid. The islanding event is detected after 30ms, the required detection time is selected based on [71, 72], in which the range of detection time is from 20ms to 40ms. Subsequently the control system of inverter transits to ac voltage and frequency control mode at 15s.

Fig. 3.12(a) shows the PCC RMS voltage during the islanding process. Significant voltage sag occurs when the main grid is disconnected. However, after the control scheme transits to islanding mode, the voltage returns to the nominal value. Fig. 3.12(b) shows the frequency response at PCC. Similar to the PCC voltage, a deviation is followed by the disconnection of main grid. However, the frequency returns to 60Hz as desired after the islanding control mode triggered. The maximum frequency deviation is less than 1Hz.

These dynamic responses confirm the ac voltage and frequency support capabilities introduced by the inverter and battery. Fig. 3.12(c) shows that the terminal voltage of one battery group is dropping since it is responsible for the active power support after islanding. The battery current is shown in Fig. 3.12(d). The system frequency is fully controlled by the battery. Fast current regulation is expected as Fig. 3.12(d) shows. Meanwhile, the SOC keeps dropping since the battery is discharging as shown in Fig. 3.12(e).

31
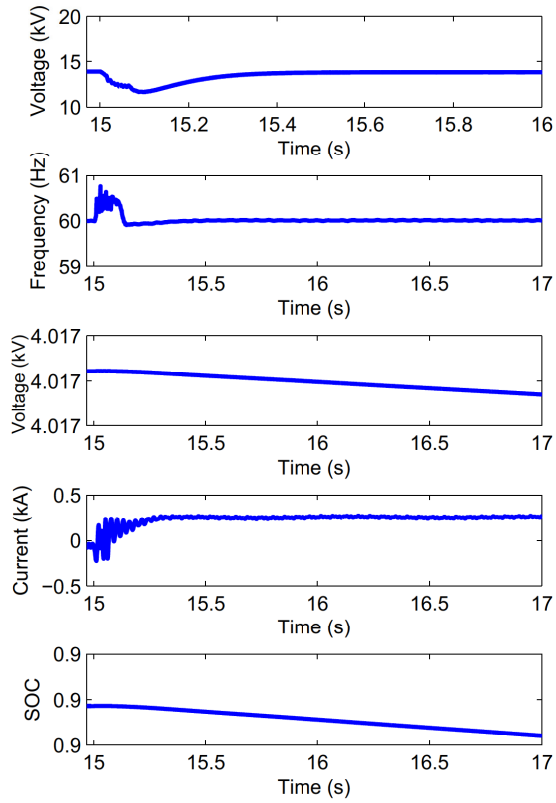
Figure 3.12. System behavior during island-ing.
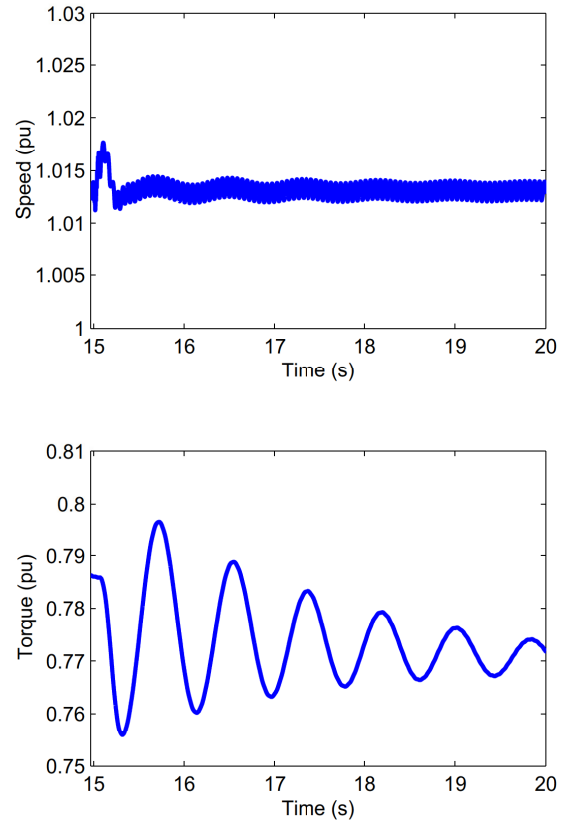
Figure 3.13. Performance of induction ma-chine during islanding.

32

Fig. 3.13 shows the dynamic responses of the induction machine during islanding. Oscillations occurred both on induction machine speed and torque. However, with the help of the battery system, they return to pre-fault value and remain stable.
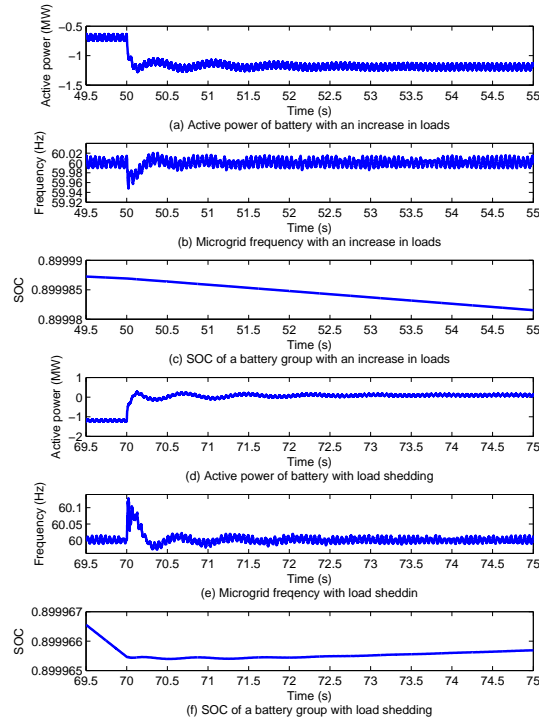
Figure 3.14. Performance of the microgrid with load changing after islanding.
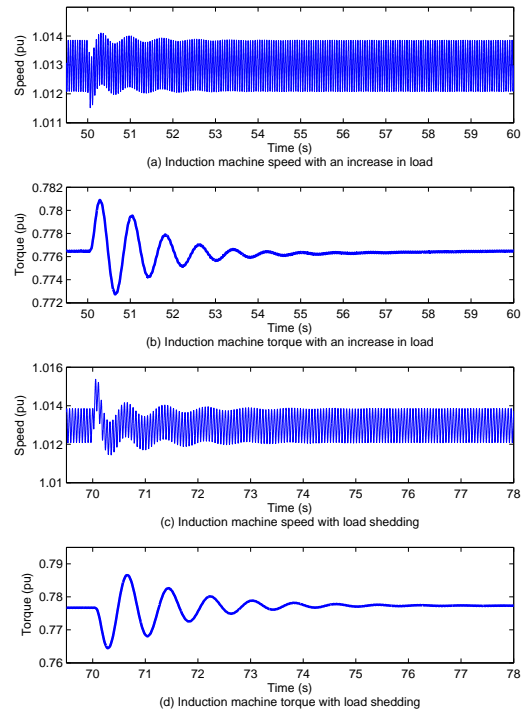
Figure 3.15. Performance of the IM with load changing after islanding.

3.4.2.2   Increase and Decrease in Loads

In order to validate the voltage and frequency regulation capabilities of the inverter and batteries after an islanding event, two load change scenarios are implemented.

At 30s, one load at the rating of 0.5MW and 0.164MVar is switched on. Fig. 3.14 shows the responses of battery output power and the microgrid frequency. The active power output of the battery increases 0.5MW instantaneously while there are transients in frequency. The microgrid frequency has a transient decrease (0.04 Hz) due to the increase of loads.

33

Load shedding is applied to evaluate the control system, which is shown in Fig. 3.14(d) and (e). At 40s, one load at the rating of 1.292MW and 0.356MVar is switched off, which simulates a load shedding. The batteries switch from a discharging state to a charging state. The frequency has a transient increase (0.12 Hz maximum) due to load shedding.

An induction generator driven by a bio-diesel machine is included in the microgrid. Fig. 3.15 demonstrates the performance of induction machine in the autonomous microgrid. A damped oscillation is occurred both on induction machine speed and torque. However, with the help of the battery system, they return to pre-fault value and remain stable. From Fig. 3.15, it is clear that the battery system could take the responsibility to regulate the power balance without adjustment on induction machine.

CHAPTER 4

COORDINATED CONTROL OF A SOLAR AND BATTERY SYSTEM IN A MICROGRID

4.1 Introduction

The objective of this chapter[1] is to study the control strategies for a microgrid with both a battery group and a PV array [73]. The study approach is detailed model based simulation. Detailed battery models have been described in Chapter 3. PV model has been investigated thoroughly in the literature. The current source and anti-parallel diode model has been proved to be able to simulate the V-I characteristics of a solar cell accurately. For the PV and battery combined systems, [28] proposed a power management mechanism that could optimize the power flow. [29] utilizes batteries to reduce the fluctuations of PV output. [30] presents the power scheduling within PV and battery system from the power system's point of view. Besides the PV and battery combined system, PV and capacitor combined system is also examined by [31, 32, 33]. Capacitors are also could be used to reduce the power fluctuation of PV, or participate in frequency control.

The above mentioned research work have focus on the grid-connected mode operation. The focus of this chapter is control strategies at the autonomous mode. The research was conducted on developing battery operating strategies based on a detailed battery model at both the grid-connected and the autonomous mode. The research results were summarized in Chapter 3. In this chapter, the research is expanded to include a PV array in the microgrid. Coordination among different DERs will be taken into consideration.

---

[1]This chapter was published in Transmission and Distribution Conference and Exposition (T&D), 2012 IEEE PES, vol., no., pp.1,7, 7-10 May 2012. Permission is included in Appendix B.

4.2 A Microgrid With a Battery, a PV Array and an Induction Generator

4.2.1 System Topology

The microgrid studied in this chapter consists of three DERs. An induction machine driven by a diesel engine works at the generating mode. It supplies active power to the loads within microgrid. A PV array is connected to the microgrid and supports the loads as well. A VSC interfaced battery station is included to store excess energy from the PV array or inject energy when there is a need. Fig. 4.1 shows the topology of the investigated microgrid where three distribution lines are used to connect each component. The topology complies with the IEEE Standard 399-1997 [67].
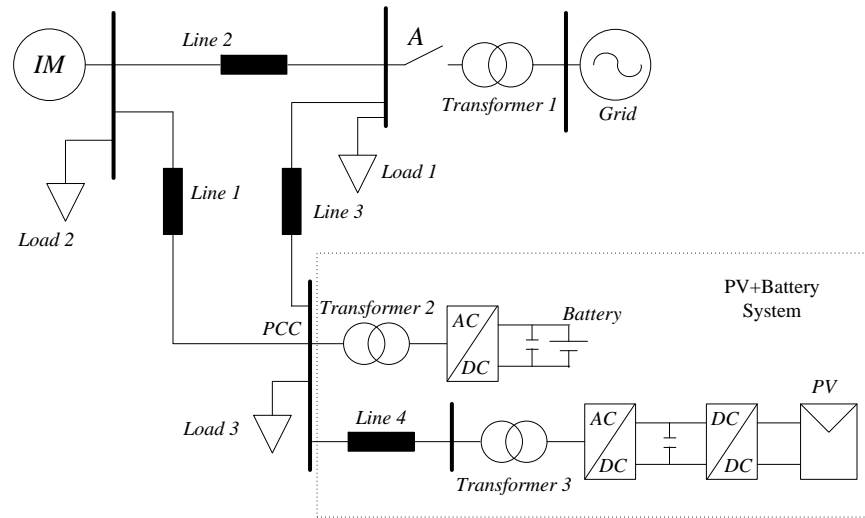
Figure 4.1. System topology.

The microgrid is built in PSCAD/EMTDC with all DERs are modeled in details. The battery station consists of two groups connected in series. Each group has an equivalent open circuit dc voltage at 4.1 kV. The maximum active power capability of which is 2MW for each group, and the energy capacity is 500kWh, which means the whole battery station could inject 4MW active power to the microgrid for 15 minutes.

The PV array consisted of many small PV panels, which could build up an open circuit dc voltage to 6 kV for the whole array. The short circuit dc current under nominal insolation level is set to 1 kA. The PV array is connected to a dc/dc converter, which is controlled by Maximum

Power Point Tracking (MPPT) algorithm. A dc/ac inverter which utilizes IGBTs connects the dc/dc converter to the microgrid.

An induction machine which runs on the generator mode is included in the microgrid. It is driven by a diesel engine. The nominal phase voltage and current are 8kV and 0.5kA respectively. Some other system parameters are listed in Table 4.1.

Table 4.1. Simulation system parameters

Quantity	Value
ac grid voltage	69kV (L-L RMS)
Transformer 1	13.8kV/69kV, 20MVA, leakage 8%pu
Transformer 2	13.8kV/3.3kV, 10MVA, leakage 10%pu
Transformer 3	13.8kV/3.3kV, 10MVA, leakage 10%pu
Load 1	2.521MW+0.831MVar at 13.8kV
Load 2	4.994MW+1.029MVar at 13.8kV
Load 3	2.5MW+0.822MVar at 13.8kV
Distribution line 1	980ft, (0.044+j0.0359)ohm
Distribution line 2	1187ft, (0.052+j0.0436)ohm
Distribution line 3	1187ft, (0.052+j0.0436)ohm
Induction machine ratings	8kV (phase voltage), 0.5kA(phase current)
PV ratings	6kV, 1kA
Battery ratings	8.2kV, 120Ahr

Table 4.2. Induction machine parameters

Quantity	Value
Rated RMS phase voltage	8kV
Rated RMS phase current	0.5kA
Base angular frequency	60Hz
Stator resistance	0.066pu
First cage resistance	0.298pu
Second cage resistance	0.018pu
Stator unsaturated leakage reactance	0.046pu
Unsaturated magnetizing reactance	3.86pu
Rotor unsaturated mutual reactance	0.122pu
Second cage unsaturated reactance	0.105pu
Polar moment of inertia	1.0s
Mechanical damping	0.0001pu

4.2.2 Battery Model

The battery model that built in PSCAD/EMTDC includes two parts [26]. One part is the energy model and the other part is the circuit model. The detailed modeling of this battery is described in Chapter 3.

4.2.3 PV Model

The PV model is built based on well-known PV models in [74, 75, 76]. Generally, a PV array consists of many solar cells with each solar cell represented by a current source. The output current normally depends on sunlight and cell temperature. Practically, a solar cell can be modeled as a current source with an anti-parallel diode. A parallel resistor R_{sh} could represent the leakage current inside the cell, and a series resistor R_s could represent the conducting loss. Fig. 4.2 shows a practical model of solar cell based on the introduction above.
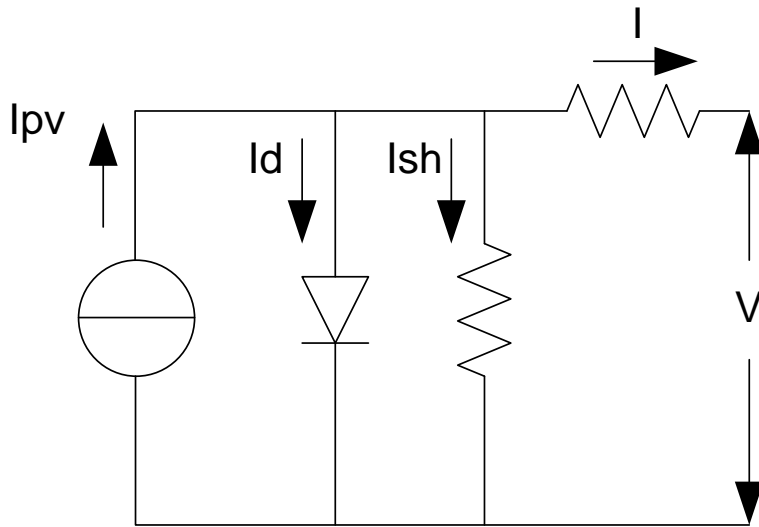
Figure 4.2. A solar cell model.

The basic equation that represents the relationship between the solar cell current I and voltage V is given in (4.1), which implies the actual output current of a solar cell not only depends on sunlight, but also depends on output voltage and other factors. In (4.1), I_{pv} is the internal current generated by sunlight on solar cell, I_o is the diode current, I_r is the leakage current through shunt

resistor, and V and I are output voltage and current of the solar cell respectively. Some constant values used in the equations and have shown in table 4.3. The diode saturation current I_o can be expressed by (4.2), where E_g is the band gap energy of semiconductor, T_n is the nominal temperature which is 298 Kelvin in this chapter. I_{on} is the nominal saturation current and is described by (4.3), where I_{sc} and V_oc are the short circuit current and open circuit voltage of solar cell respectively, V_t is the thermal voltage, which is described by (4.5), where N_s is the number os series connected cells in an array. The internal current generated by sunlight of solar cell can be expressed by (4.4), where K_i is the short circuit current/temperature coefficient, and G is the solar irradiation in W/m^2 and G_n is the nominal solar irradiation.

$$I = I_{pv} - I_o[exp(\frac{q(V + IR_s)}{\alpha KT}) - 1] - I_r \tag{4.1}$$

Table 4.3. Parameters of solar cell

Quantity	Value
q	$1.6 \times 10^{-19}C$
K	$1.38 \times 10^{-23}J/K$
α	1.5
E_g	1.2
K_i	$1.141mA/K$

$$I_o = I_{o,n}(\frac{T_n}{T})^3 exp[\frac{qE_g}{\alpha K}(\frac{1}{T_n} - \frac{1}{T})] \tag{4.2}$$

$$I_{o,n} = \frac{I_{sc}}{exp(\frac{V_{oc}}{\alpha V_t}) - 1} \tag{4.3}$$

$$I_{pv} = [I_{sc} + K_i(T - T_n)]\frac{G}{G_n} \tag{4.4}$$

$$K_t = \frac{N_s KT}{q} \tag{4.5}$$

Based on (4.1) - (4.5) and the parameters shown in Table 4.3, two graphs of the relationships between current, voltage and power of solar cells could be obtained. Fig. 4.3 (a) shows the relationship between output current and voltage of solar cell on different insolation levels, while

Fig. 4.3 (b) shows the relationship between output power and voltage of solar cell on different insolation levels. From those figures, generally, it is clear that current increases as the insolation increases, and the behavior of power has similar characteristic as well. There is one maximum power point for each insolation level, and it is desired for the operator that the maximum power could always be extracted and injected into grid. This process normally called MPPT and could be done by a dc/dc converter which will be elaborated later.
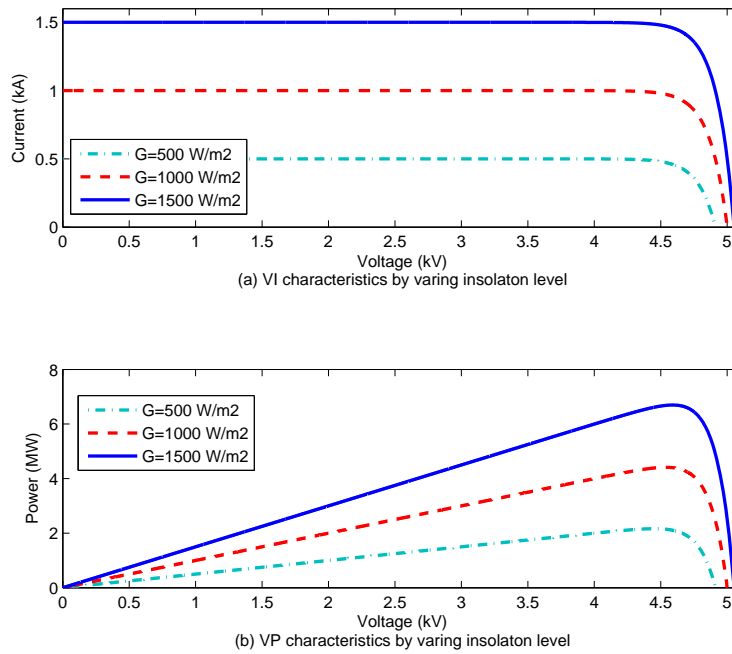
Figure 4.3. Output characteristics of PV array by varying insolation level.

4.3   System Controls

Both battery and PV arrays are connected to grid via VSCs, and a dc/dc converter is also utilized between the inverter and PV array terminals. Regarding the microgrid investigated in this chapter, two operating modes are considered. The first operating mode is the grid-connected mode, which means a strong ac grid is connected via a transformer and feed the microgrid. However, the tie between microgrid and the strong ac grid may be disconnected due to some faults, and therefore,

it is expected that the microgrid could be able to operate at the autonomous mode when such faults occur. Since there is no synchronous generator existed in this microgrid, the voltage and frequency will be supported by VSCs. As a result, depending on the operating mode of microgrid, the VSCs could either operate at PQ control mode at grid-connected or voltage/frequency (Vf) control mode when the microgrid is at autonomous mode. The control of PV arrays involves two kinds of converters, one is dc/ac inverter, while the other is dc/dc converter. Since the active power generated by PV array normally fluctuates as sunlight or other factors changes, it is not suitable to ask the VSCs of which to operate on Vf control mode. Hence, the VSCs of PV arrays always operate on PQ control mode, which implies that the VSCs should always deliver the active power generated by PV arrays to grid, and inject the reactive power depends on the need of microgrid. The dc/dc converter should extract the maximum power from PV arrays and send to the dc/ac inverter, which could be achieved by MPPT algorithm.

4.3.1 Battery Control

The battery control details are described in Chapter 3 and will be ignored in this chapter.

4.3.2 PV Array Control

Fig. 4.4 depicts the structure of PV array and its dc/ac inverter and dc/dc converter. The dc/dc converter is a boost converter, since the nominal dc-link voltage is 15kV which is always larger than the PV array voltage. Therefore, the control system of PV array consists of two part, which is VSCs control and dc/dc converter control.
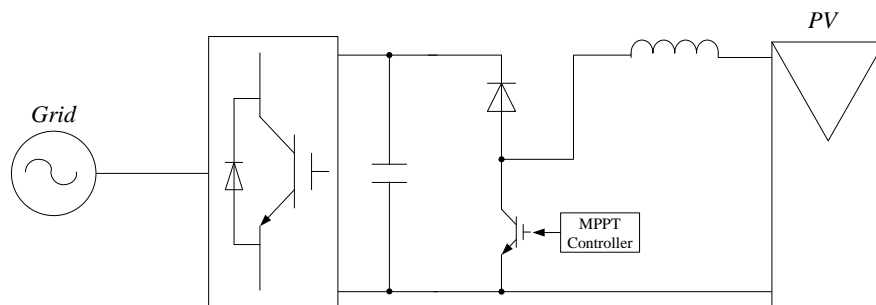
Figure 4.4. PV array and its respective converters.

41

4.3.2.1   PQ Control

The dc/ac inverter which consists of VSCs always operates at PQ control mode. Since the active power generated by PV array depends on sunlight and temperature and is not stable as conventional energy source. The VSCs should deliver the active power efficiently, otherwise the dc-link voltage between inverter and dc/dc converter will deviate from its reference value and may cause collapse.

4.3.2.2   MPPT Control

The critical control part of PV array is on dc/dc converter, which is expected to extract maximum power generated from PV array. There are several MPPT control algorithms in the literature [77, 78, 79]. The perturbation and observation (P&O) method has been used throughout this chapter. Basically, the operating points of reference voltage at different insolation level should be obtained first, which can be completed based on Fig. 4.3. The reference voltages are then called v_{mppt_ref}.

The control system measures the current output power of PV array and compare with the power recorded at previous step. If the current power is greater than previous one, it will compare the current output voltage with previous step. If the current voltage is larger, the reference voltage for dc/dc converter will be added by a pre-set step, which is $v_{mppt\_ref} + C$. The other control paths are similar and just in opposite direction.

Fig. 4.5 depicts the duty cycle controller of dc/dc converter. The PV output voltage reference is calculated from above $P\&O$ algorithm, and is compared with the current voltage. The error is the input of a PI controller and the respective output is the duty cycle command for dc/dc converter, which is then sent to the PWM generator.

Table 4.4. PI controller parameters of Fig. 4.5

	Kp	Ki
Duty cycle control loop	0.01	0.2
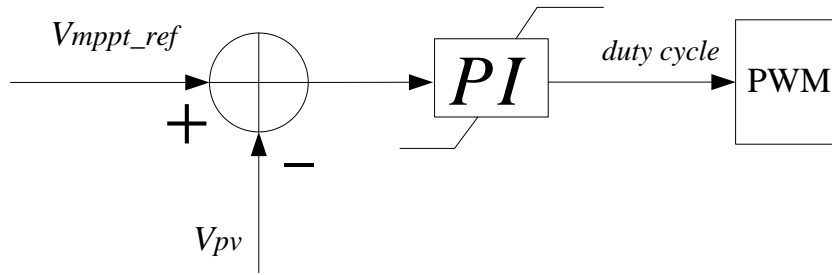
Figure 4.5. Duty cycle control of dc/dc converter.

4.3.2.3 Coordinated Control

Fig. 4.6 shows the power coordination mechanism of the PV and the battery system. ac grid voltage and frequency are the variables to be controlled. The output real power and reactive power of the battery system are dependent on the measured frequency error and voltage error. The total output power from the PV and the battery should meet the requirement of the microgrid.
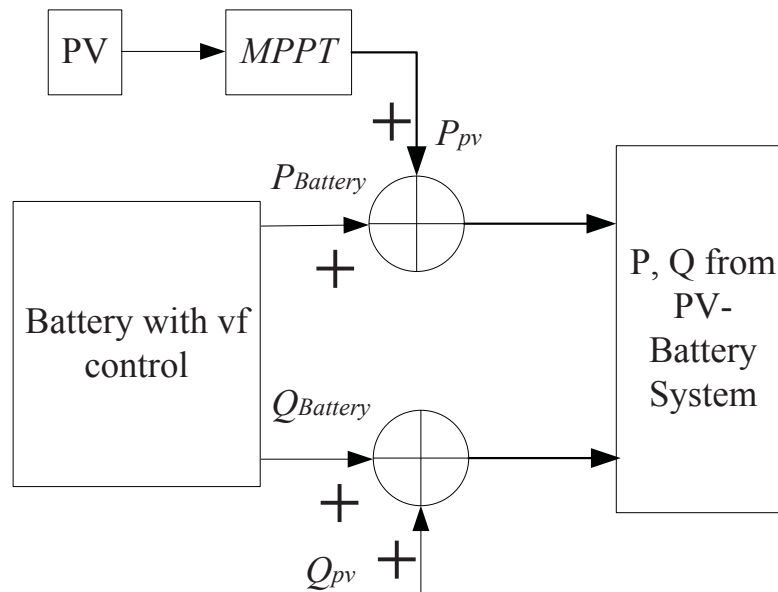
Figure 4.6. Coordinated control strategy of PV and battery system at autonomous mode.

43

4.4 System Evaluation in PSCAD/EMTDC

The studied microgrid is evaluated in PSCAD/EMTDC, which validates the efficiency of the designed controller both on grid-connected and autonomous mode. The simulations conducted are divided into two parts: 1) First, the microgrid operates on grid-connected mode, a strong ac grid with nominal voltage at 69kV is connected to the microgrid via a 69kV/13.8kV transformer. The battery is tested both on charging and discharging mode, and the PV array is tested for fast tracking capability of insolation variations; 2) Second, a pre-assumed fault occurred and forced the main breaker opened which disconnect the grid and microgrid. After certain period that is required for the controller to detect the autonomous event, the control system switched to autonomous control mode. The voltage and frequency of microgrid are monitored, which are proved that stay at nominal value after short oscillations. Several scenarios are designed to test the control system at autonomous mode, such as load increase, load shedding and insolation variations.

4.4.1 System Performance at Grid-connected Mode

During the simulation, the system is working at grid-connected mode before 15s. The battery is first charged with a ramp increased reference power that dragged from ac grid. After that, the battery starts to work at PQ control mode, the active power output changed from injecting 0.5MW to absorbing 1MW. Meanwhile, the insolation level for the PV array changes from $1000W/m^2$ to $2000W/m^2$.

Fig. 4.7 shows the waveforms of system variables at such scenario. Fig. 4.7 (a) describes the active power output of battery, which is increased from 0 to 2MW due to the ramp charging, and the output changed from charging to injecting 0.5MW into grid at 10s, at 12.5s, the active power reference changes to absorbing 1MW. Fig. 4.7 (b) shows the reactive power output of battery, which is set to 0 at grid-connected mode. In this chapter, power flowing from the grid are considered positive, while flowing into the grid are negative values.

The insolation level of PV is changed to test the controller of PV array and its converters. At 10s, the insolation level changes from $1000W/m^2$ to $2000W/m^2$, and Fig. 4.7 demonstrates the waveform of respective active power output, which increases from 3.23MW to 6.02MW at the same

44

time. The reactive power is set to absorbing 0.5MVar to the microgrid, which is shown in Fig. 4.7 (d).
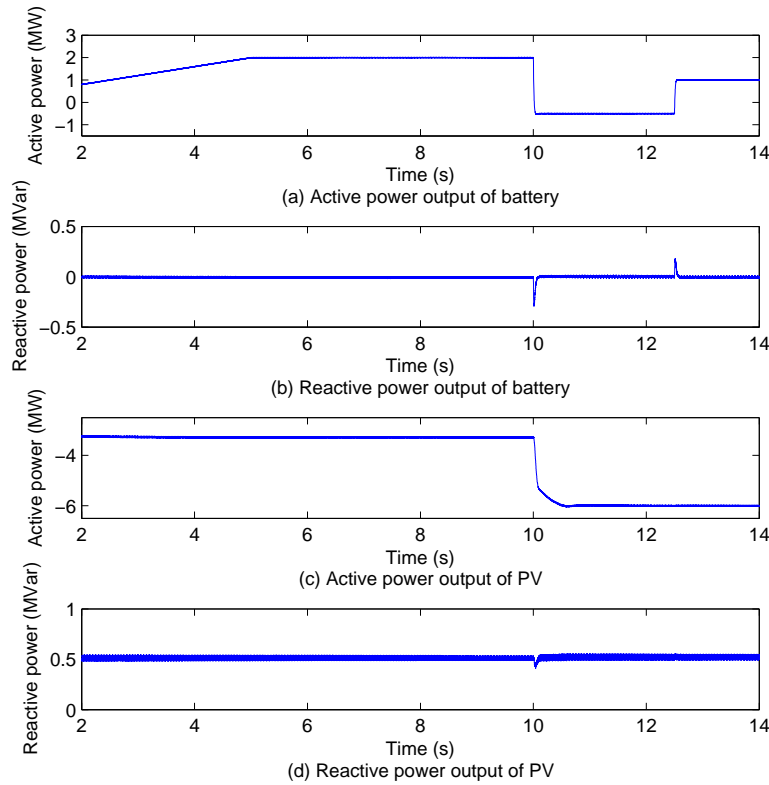
Figure 4.7. Power outputs of battery and PV at grid-connected mode.

4.4.2   System Performance at Autonomous Mode

At 14.97s, a pre-set fault is triggered which opened the breaker connecting microgrid and main ac grid. This incident leads to voltage and frequency collapse since there is no synchronous generator existed in the microgrid to provide support. After 30ms [71], the controller detects the islanding event and switches to autonomous control mode. At which, the controller of the VSCs between microgrid and battery switches to Vf control, which supports the PCC voltage and system frequency. Fig. 4.8 shows the transient behaviors, which indicates about 1.3kV voltage sag and 3kV overshoot occurred at PCC, and the frequency devastation is less than 1.5Hz and return to

45

60Hz after 0.5s. The active power of PV and battery system have small and short oscillations when breaker opened, and both return stable after around 0.5s. The transients of induction machine have similar behaviors, and only the torque needs a little bit longer time to be damped. Two other scenarios are performed to test the efficiency of designed controllers.
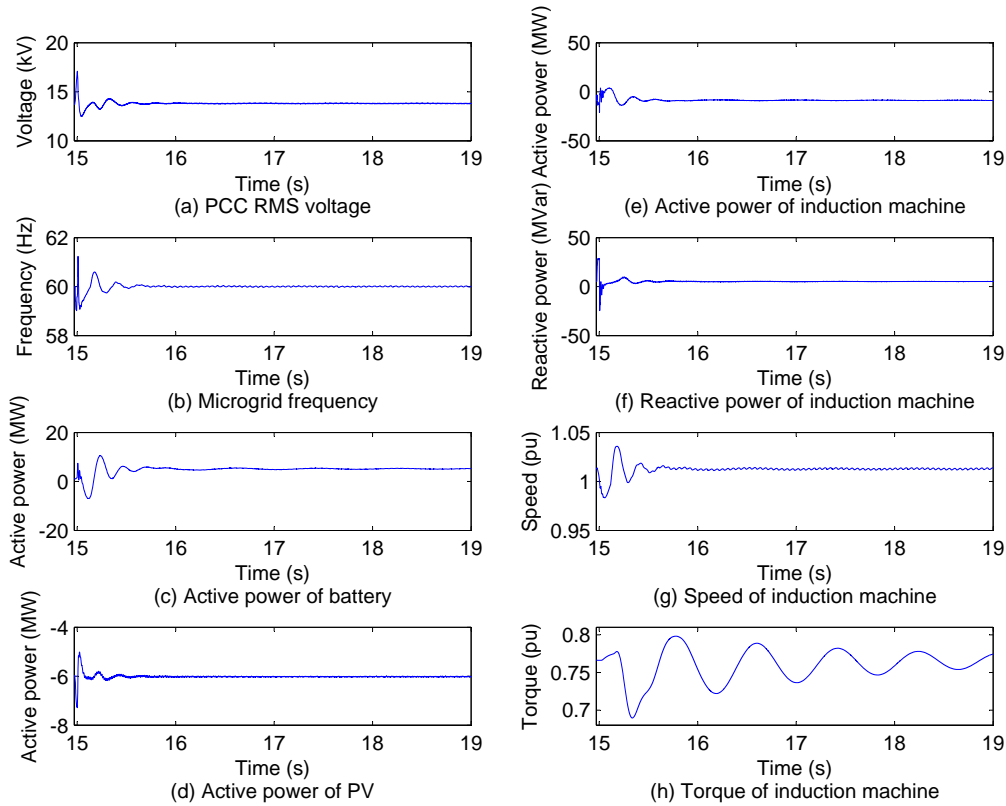
Figure 4.8. System transient during islanding event.

4.4.2.1   Insolation Variations

The insolation level varies from $2000W/m^2$ to almost $0W/m^2$ at 35s to test the capability of MPPT controller at autonomous mode. Fig. 4.9 (a) shows the waveform of active power from PV array, where the active power reduced from injecting 6MW to almost 0. Fig. 4.9 (b) shows the behaviors of battery, where the active power output of battery changes from absorbing 5MW to generating 1MW due to the loss at PV side. The microgrid frequency stays at its nominal reference

46

with only less than 0.5Hz drop at that transient. Fig. 4.9 (d) demonstrates that SOC is increasing when absorbing power from microgrid and decreasing if injecting power. The response of induction machine is similar with the case at islanding event occurred, since the power transition of PV side is significant.
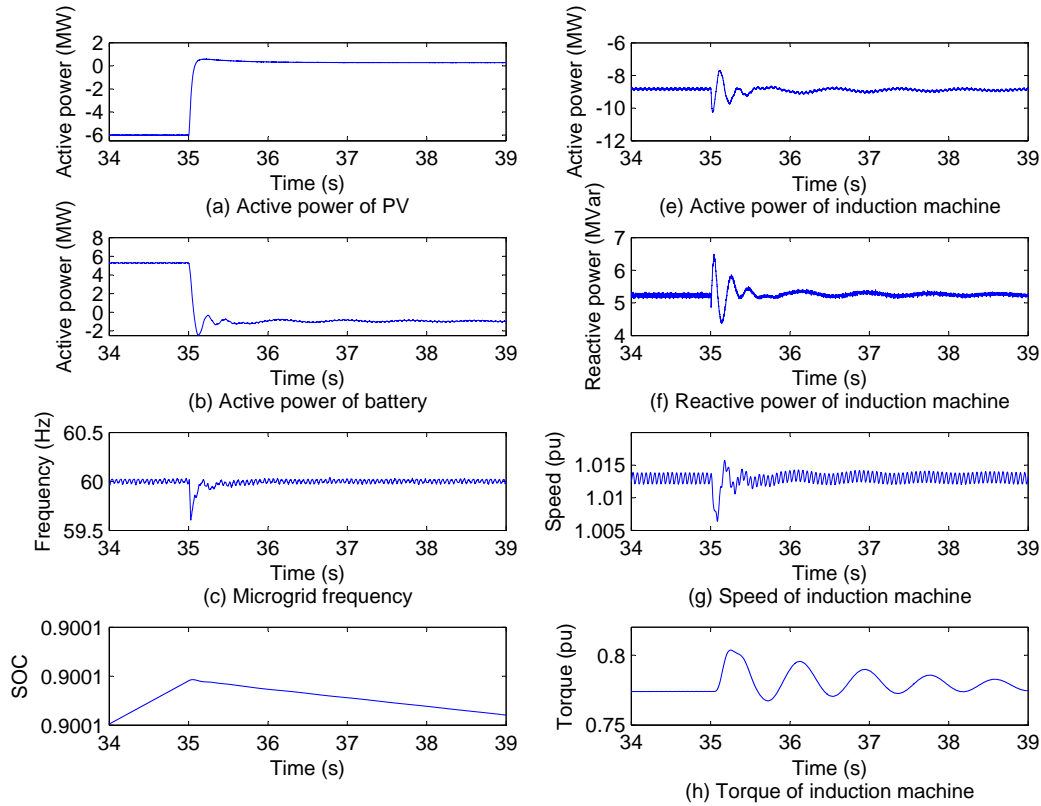
Figure 4.9. System transient during insolation variations.

4.4.2.2 Load Variations

The load within microgrid may change at any time, in order to keep the power balance between load and generation, the controller should be able to handle any load change within its capability. Since the frequency is controlled by the VSCs of battery, it is expected that the battery should take the responsibility to maintain power balance within the microgrid. Fig. 4.10 shows the system behaviors during load variations, in which, one load at 0.5MW and 0.25MVar is added to the

47

microgriid at 50s, and one load at 1.3MW and 0.5MVar is disconnected from the microgrid at 70s. Fig. 4.10 demonstrates that the active and reactive power of battery are regulated to corresponding value and maintain the stability. The active and reactive power of induction machine stay at its reference value, since only the VSCs of battery participates Vf control, and it is desired to not increase the induction machine output, which could save fuel as much as possible. In Fig. 4.10, the microgrid frequency drops 0.1Hz at 50s due to load increase while rises 0.24Hz due to load shedding. The induction machine runs smooth after short time oscillations corresponding load changes.
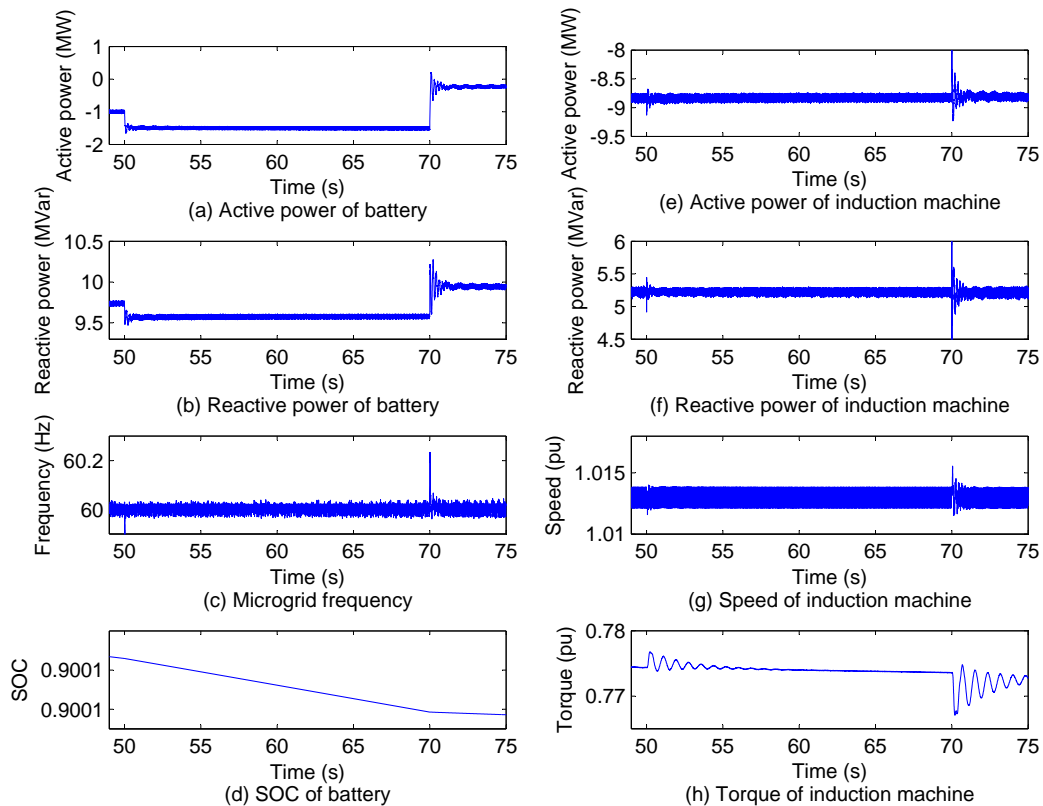
Figure 4.10. System transient during load variations.

CHAPTER 5

VSC BASED HARMONIC AND UNBALANCE MITIGATION FOR A MICROGRID

Inductive load in a microgrid normally occupies a large portion of system capacity, however, unfortunately, it is vulnerable to grid voltage unbalance. [80, 81] demonstrate the positive and negative sequence circuits of induction machine. For high power induction machine, even very low level of grid voltage unbalance may lead to very high percentage of unbalanced currents if the slip is small. In order to prevent unbalanced currents flowing into utility grid, [82, 83, 84] proposed a shunt connected VSC to inject compensation current with controller designed in dq synchronous frame. Other than compensate unbalanced currents, STATCOM and D-STATCOM have been widely used to compensate the unbalanced voltage at the PCC [85, 86, 87, 88, 89, 90].

Harmonic currents due to power electronics switching have been widely investigated in the literature. Active filter is a mature solution to mitigate the harmonic currents [34, 35, 36, 37]. The current control strategies are discussed and compared in [38], which include linear current control, digital deadbeat control and hysteresis control. The linear current control utilizing dq synchronous frame control has been proposed and tested [34, 35, 39, 40]. Another control method developed in [40, 41] is called Proportional-Resonant (PR) controller. With PR control theory, the complexity of harmonic current control system can be effectively reduced for both positive and negative sequences. Uncontrolled power electronics devices with load can produce non-negligible low orders harmonic currents to microgrid. In [42], even small percentage of grid voltage unbalance would lead to additional high 3rd order harmonic currents from rectifiers. In order to eliminate the harmonic currents, a appropriate control strategy has to be developed.

Unbalanced current and harmonic current compensation normally need the installation of VSCs, such as active filters. As discussed above, a microgrid with DERs always equipped with battery with

49

inverters. Without investing in additional VSCs, the inverter of battery can take the responsibility to not only charge/discharge but also compensate unbalanced and harmonic currents.

The objective of this chapter is to develop a control strategy for the inverter of a battery to compensate unbalanced and harmonic currents under various grid voltage conditions.

5.1   System Configuration

The microgrid studied for this chapter consists of a PV station and a battery as the distribution generation and storage devices respectively. An induction machine and a RL load with rectifier are chosen as the customer load. The microgrid is connected with the main grid via a transformer. Fig. 5.1 shows the topology of the studied system, while the parameters are listed in Table 5.1. The battery station consists of two groups connected in series. Each group has an equivalent open circuit dc voltage at 4.1 kV. The maximum active power capability of which is 1MW for each group, and the energy capacity is 1MWh, which means the whole battery station could inject 2MW active power to the microgrid for 1 hour.

The PV array consisted of many small PV panels, which could build up an open circuit dc voltage to 2 kV for the whole array. The short circuit dc current under nominal insolation level is set to 1 kA. The PV array is connected to a dc/dc converter, which is controlled by MPPT algorithm. A dc/ac inverter which utilizes IGBTs connects the dc/dc converter to the microgrid.

The induction machine is used to simulate traditional customer load, which can also inject significant negative sequence currents when it even subjects to a small percentage of unbalanced system voltage. A simple RL load connected with rectifier can simulate the harmonic currents due to uncontrollable power electronics devices.

Fig. 5.2 depicts the positive and negative sequence equivalent circuit of an induction machine. R_s and X_s are stator resistance and reactance respectively, R_r and X_r are rotor resistance and reactance referred to stator side respectively. X_m is the magnetizing reactance. V_p and V_n represent the positive and negative sequences of voltage, while I_{ps}, I_{pr} and I_{ns}, I_{nr} are the corresponding currents. For the sake of simple analysis, the magnetizing reactance X_m is neglected. The positive and negative sequence currents can be written as (5.1) and (5.2). It is clear that even a very low

50
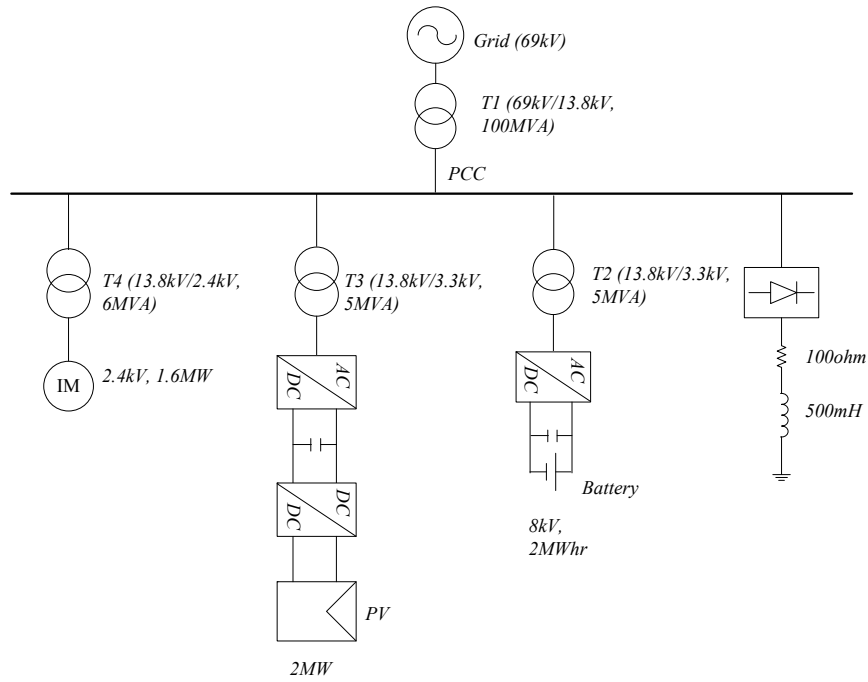
Figure 5.1. System topology of a microgrid.

Table 5.1. Simulation system parameters

Quantity	Value
ac grid voltage	69kV (L-L RMS)
Transformer 1	69kV/13.8kV, 100MVA, leakage 8%pu
Transformer 2	13.8kV/3.3kV, 5MVA, leakage 10%pu
Transformer 3	13.8kV/3.3kV, 5MVA, leakage 10%pu
Transformer 4	13.8kV/2.4kV, 6MVA, leakage 10%pu
Induction machine ratings	2.4kV, 1.6MW
Battery ratings	8.2kV, 2MWhr
PV ratings	2kV, 2MVA
Load ratings	100ohm+500mH
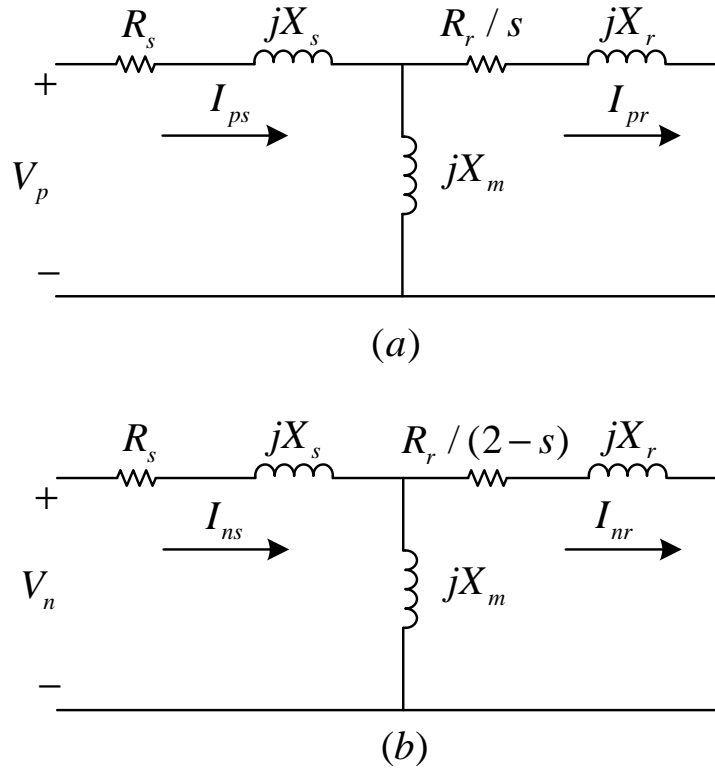
Figure 5.2. Induction machine positive and negative sequence equivalent circuit.

negative sequence voltage would induce a relatively high negative sequence current. For example, if $R_s = 0.3$, $R_r = 0.1$, $X_s = 0.5$, $X_r = 0.2$, $s = 0.01$, $V_p = 1.0$, and V_n is only 2% of V_p, the resulting negative sequence current is $I_{ns} = 0.0256$, whereas, the positive sequence current is $I_{ps} = 0.0969$. The negative sequence current is 26.42% of positive sequence current although the negative sequence voltage is only 2%. Therefore, when there is a small part of negative sequence voltage superposed at PCC, the induction machine will inject significant unbalanced currents to the system.

$$I_{ps} = \frac{V_p}{\sqrt{\left(R_s + \frac{R_r}{s}\right)^2 + (X_s + X_r)^2}} \tag{5.1}$$

$$I_{ns} = \frac{V_n}{\sqrt{\left(R_s + \frac{R_r}{2-s}\right)^2 + (X_s + X_r)^2}} \tag{5.2}$$

52
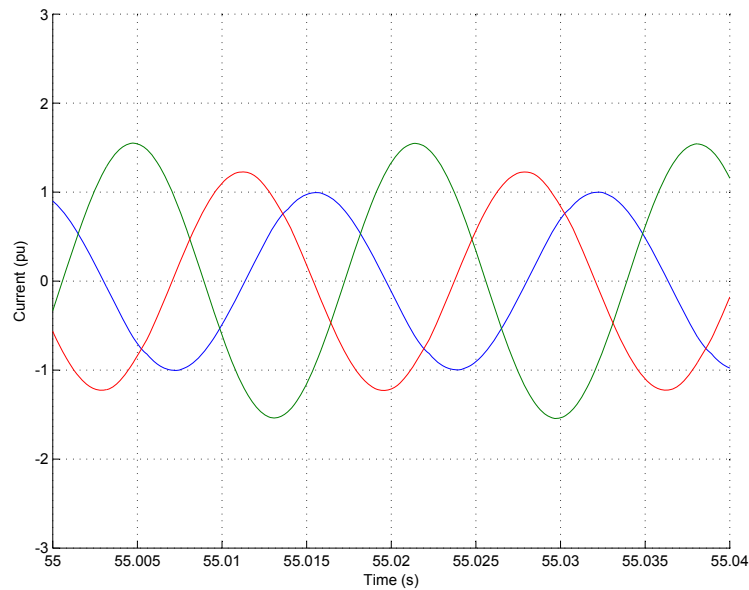
Figure 5.3. Induction machine current under 2% unbalanced grid voltage.

5.1.1 Consequence of Unbalance in Motor Loads

The consequence of unbalanced voltage applied in motor loads is demonstrated in Fig. 5.3, which shows the induction machine currents. The system voltage contains a 2% negative sequence, however, the magnitude of negative sequence is as high as 26% of the positive sequence component. Such high magnitude negative sequence currents may cause severe problems to the end users, since it may cause vibrations on machine, unstable rotating speed and noise. The power factor and efficiency of machine may be worsen as well. The worst case would be shut down of the machine. For sensitive industry customers, such system performance is not acceptable since the financial loss would be very high.

5.1.2 Consequence of Unbalance in Rectifier Loads

The consequence of unbalanced voltage applied in rectifier loads is also presented in Fig. 5.4. The system voltage also has 2% negative sequence. Fig. 5.4 shows the rectifier phase A current, which is quite different than when under balanced grid voltage. When under balanced grid voltage,

53

Figure 5.4. Rectifier current under 2% unbalanced grid voltage.

the main harmonic components are 5th and 7th order, while the largest harmonic shifts to 3rd order in Fig. 5.4. The grid current injected into main grid is critical to power quality, which is shown in Fig. 5.5. The current harmonics limits for a power system can be found in IEEE standard [91], which is 4% for harmonic order of 9 and less, and 2% for harmonic order of 15 and less. Fig. 5.6 depicts the FFT analysis of grid current under 2% unbalanced grid voltage. The red bar is the magnitude percentage corresponding to fundamental current for various odd harmonic orders, while the green bar is the limit specified by the standard for different odd harmonic order currents. Based on the system parameters and short circuit calculation, the THD limit of grid current for the model is 8% [91]. However, the actual THD of the current for this case is 15.86%, which is almost 2 times of the limit.

5.2 Controller Design

Since the battery is connected with the microgrid via VSC, it is possible to design a proper control strategy to have the VSC to compensate both negative sequence and harmonic currents injected into the grid. The reason does not use the PV's VSC to perform the compensation is that

54
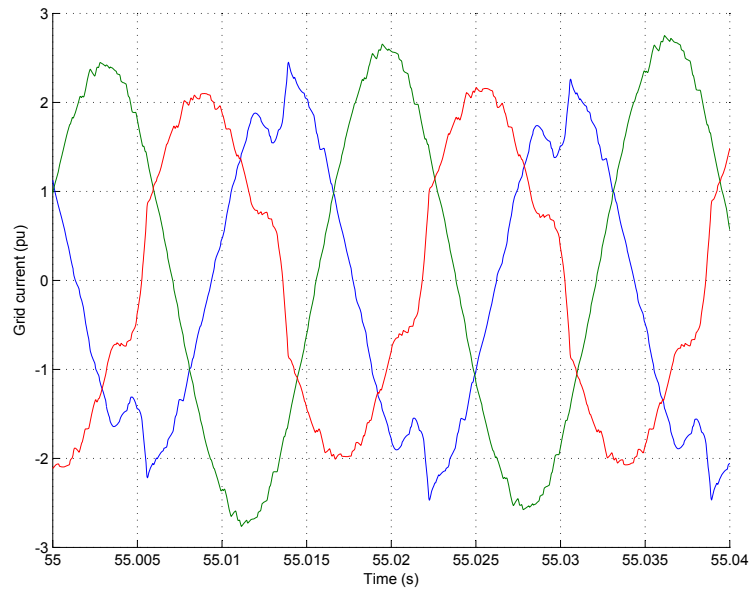
Figure 5.5. Grid current under 2% unbalanced grid voltage.
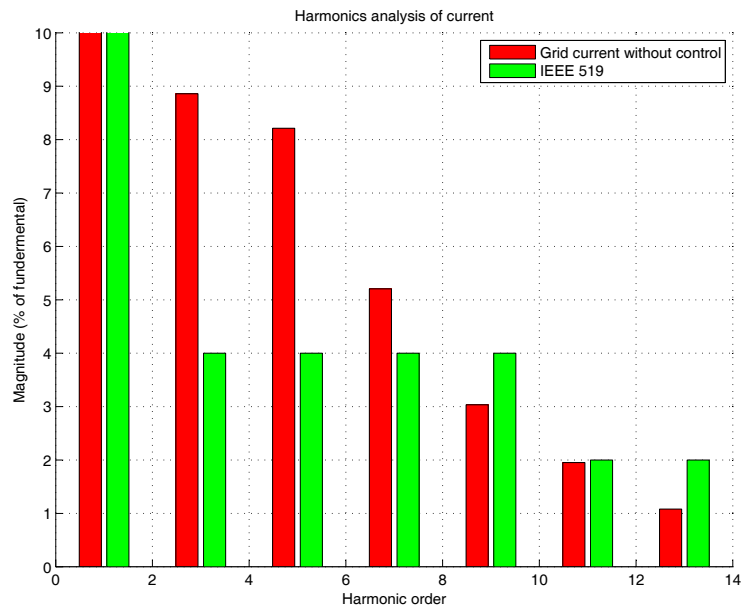
Figure 5.6. FFT analysis of grid current under 2% unbalanced grid voltage.

55
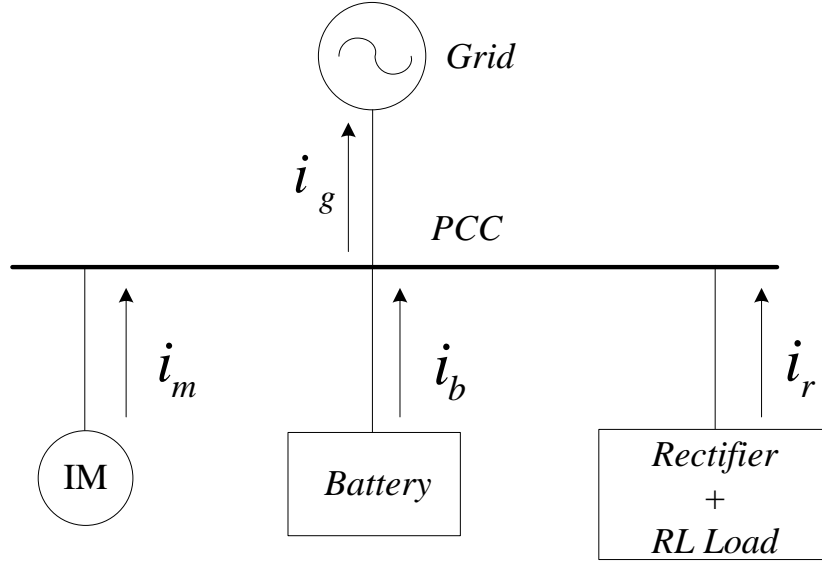
Figure 5.7. Simplified system topology.

the VSC of PV has to control the dc voltage for PV panel's dc/dc converter. However, the battery has a relatively stable dc voltage, so its VSC has more freedom to implement sophisticated control objectives.

In Fig. 5.7, the microgrid is simplified with each component's current labeled. Since the major negative sequence and harmonic currents are contributed by induction machine and rectifier, the PV station is ignored in Fig. 5.7. Assuming the PCC voltage is unbalanced, the induction machine current i_m can be written as $i_m = i_{mp} + i_{mn}$, where i_{mp} and i_{mn} represent the positive and negative sequence current. The rectifier load current i_r also can be written as $i_r = \sum_{k=1} (i_{rp\_k} + i_{rn\_k})$, where $k = 1, 2, 3...$ is the harmonic order and the subscript rp and rn represent positive and negative sequences. Apparently, the current i_g injected into the grid would contain various harmonic currents and negative sequences, which is not acceptable in terms of power quality.

One solution for this problem is to design a proper control strategy for the battery's VSC and make it inject specific currents to the grid for compensation. For instance, let the battery $i_b = i_{b0} - i_{mn} - \sum_{k=2} i_{rp\_k} - \sum_{k=1} i_{rn\_k}$, where i_{b0} is the battery's own current order. So the total grid current i_g will only have positive sequence and the negative sequence and harmonic currents will be canceled out.

56
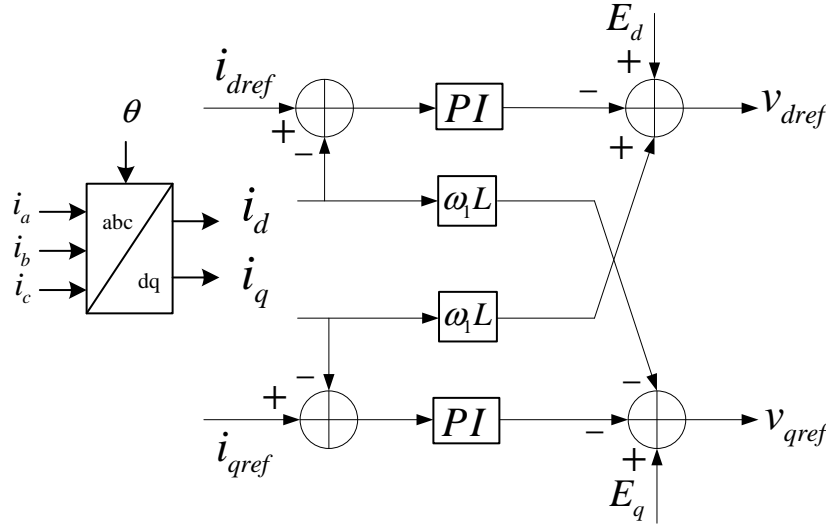
Figure 5.8. Conventional dq control strategy for VSC.

The conventional control scheme for VSC is dq decoupled control algorithm, which is shown in Fig. 5.8. θ is the system voltage angle at nominal frequency of 60Hz. For a balanced system, the currents i_d and i_q are both dc quantities, and the PI controllers are able to regulate them in order to track the respective references. However, under unbalanced case, the dq currents are no longer dc quantities but contain ac time varying currents at frequency of 120Hz. Since PI controllers can not track ac signals, two low pass filters are needed to get rid of the 120Hz components. Similarly, in order to control the negative sequence current, a negative sequence dq transformation is needed and two low pass filters are required to filter out the 120Hz positive sequence part. Moreover, this control structure is specific for nominal frequency, for each harmonic order, a complete set of the controller shown in Fig. 5.8 is needed. The difference is the angle θ will be the corresponding angle at each harmonic order. Obviously, the complexity of the overall controller is very high and the calculation burden will cost much resources for a real controller.

Instead of the conventional dq controller, a PR controller is more suitable for such kind of application. The transfer function of a PR controller is shown in (5.3), where K_p is the proportional gain and K_{ih} is the resonance gain for each harmonic order. The control structure is also shown in Fig. 5.9, where only first order and second order controller are drawn. The current regulated by PR controller has to be ac current as it has very limited response for dc signals. Another

57
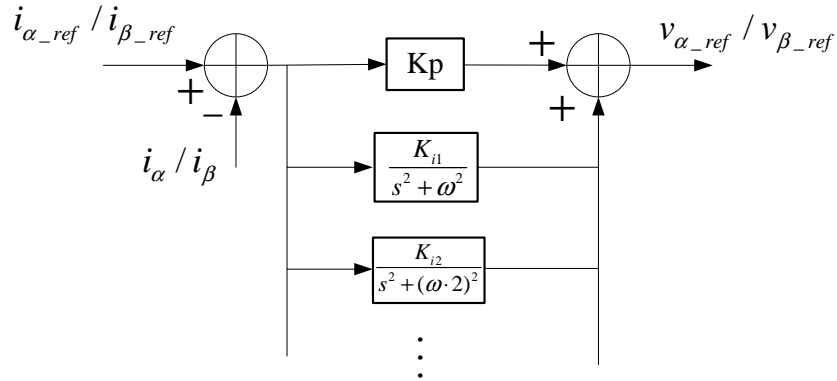
Figure 5.9. A PR controller structure.

advantage of PR controller is for each order of current, the controller can regulate both positive and negative sequence as long as the frequency is the same with the controller's harmonic order [40, 41]. Hence, the overall controller would be much more easier to implement. Since the controller needs ac current signals, instead of dq transformation, the abc currents will be transformed into $\alpha\beta$ frame. The current reference of battery shown above will also be transformed into $\alpha\beta$. Obviously, in order to get a proper current reference for battery, a signal conditioning unit which can correctly extract the negative sequence and harmonic currents of i_m and i_r is needed.

$$G_h(s) = K_p + \sum_{h=2,3,4...} K_{ih}\frac{s}{s^2 + (\omega \cdot h)^2} \tag{5.3}$$

5.3 Validation

A simulation model of microgrid is built in RT-LAB in order to validate the capability of battery inverter for negative sequence and harmonics current compensation. RT-LAB is a Real-Time Digital Simulator manufactured by OPAL-RT which can simulate the power system model with detailed power electronics switches in real-time. Therefore, it can provide precise simulation results and taking the switching details of IGBTs into account. Moreover, the simulation can run in real time and highly improve simulation efficiency. Fig. 5.10 shows the setup of RT-LAB simulator

58
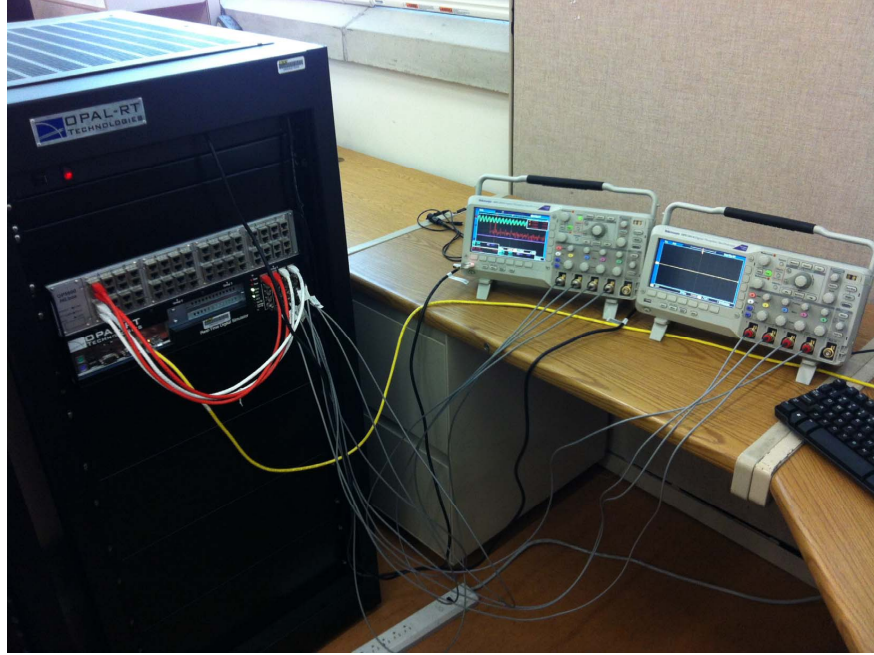
Figure 5.10. Real-time digital simulation setup using RT-LAB.

and its corresponding oscilloscopes which monitor the simulation signals, such as voltage, current and power.

A three-phase programmable voltage source is selected to emulate the grid. Besides the regular positive sequence voltages, the programmable voltage source can also generate negative sequence voltages and superpose them onto the positive sequence. Therefore, that feature can be used to simulate the unbalanced voltage cases. Four cases will be conducted to investigate the current compensation capability of battery inverter with PR controller. The first case would investigate the unbalanced and harmonic currents pollution to the grid under 2% unbalanced voltage without Unbalanced Current (UC) and Harmonic Current (HC) controllers. The other three 3 cases would investigate the system performance under different level of unbalanced grid voltage with the help of UC and HC controllers.
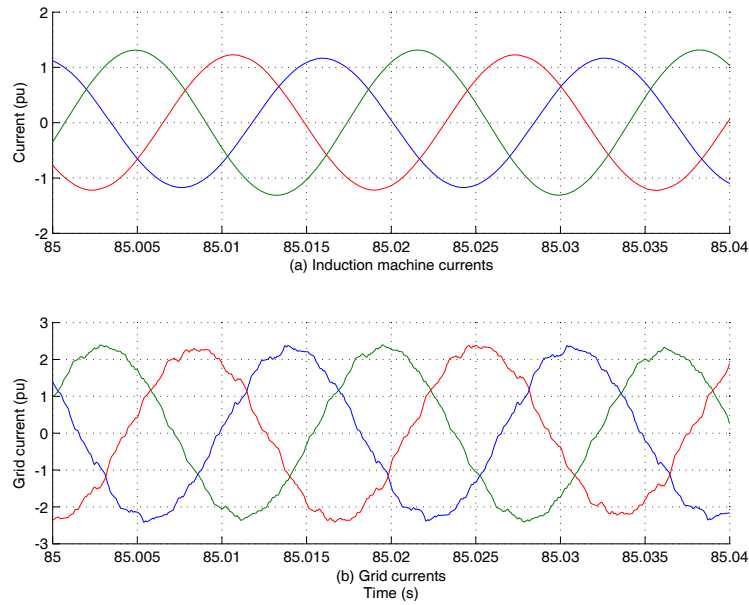
Figure 5.11. Induction machine and grid currents under 0.5% unbalanced grid voltage.

5.3.1   Case I

The microgrid built in RT-LAB consists of five main components, which are main grid, induction machine, rectifier with load, battery and PV station. The electrical parameters are shown in Table 5.1.

The first case investigates the system performance while the UC controller is enabled. The HC controller is firstly disabled and then enabled to validate the harmonic current compensation capability by battery inverter. The negative sequence of grid voltage is set to 0.5%, which indicates a relatively low unbalanced grid voltage case. Fig. 5.11 (a) shows the induction machine currents which contain 7% negative sequence component, and Fig. 5.11 (b) shows the grid currents with both UC and HC controllers enabled. Fig. 5.12 shows the rectifier phase A current, which has various harmonic components. The 3rd harmonic current is smaller comparing with Fig. 5.3. Generally, the 3rd harmonic current increase as the voltage contains more negative sequence.

Fig. 5.13 depicts the battery inverter current in stationary frame. The blue trace is the battery inverter α current reference and the red line is the actual α current. Since the battery has to inject

60
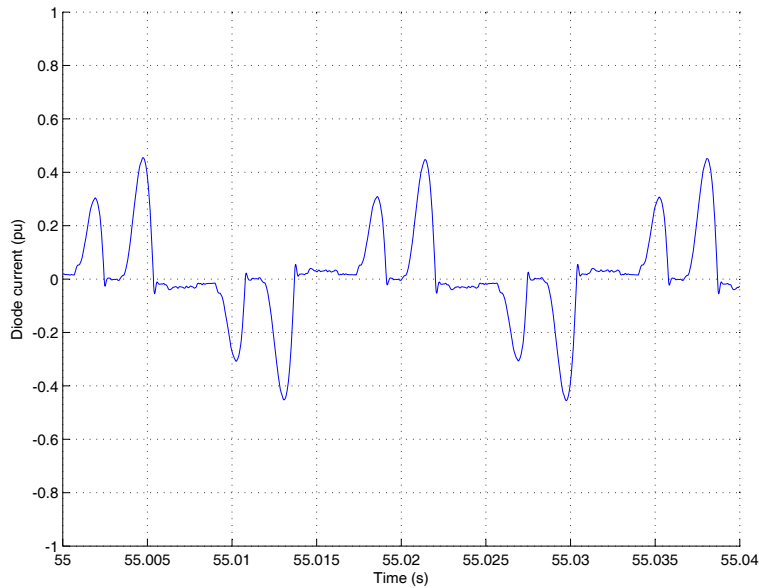
Figure 5.12. Rectifier current under 0.5% unbalanced grid voltage.

harmonic currents to compensate the rectifier current, the reference current is already distorted. Thanks to the UC and HC controllers, the actual current tracks the reference in a precisely manner both on α and β axes. Therefore, the grid phase A current shown in Fig. 5.14 (b) is improved comparing to Fig. 5.14 (a) when the HC controller is disabled. The FFT analysis of case II is included in Fig. 5.15, the 5th and 11th order harmonic current are beyond the limits set by [91] when the HC controller is disabled. With the help of HC controller, all odd order harmonic currents are less than the limits. The THD of grid current without HC controller is 11.3% while the THD of grid current decreases to 5.1% with HC controller enabled.

5.3.2   Case II

In Case, the negative sequence voltage is 2%, however, the HC controller is enabled after 60s. Fig. 5.16 shows the induction machine and grid currents under 2% unbalanced grid voltage. The negative sequence induced by induction machine is the same as 26%, however, the injected grid currents have eliminated most of the negative and harmonic currents by UC and HC controllers. The rectifier current is identical to Fig. 5.4 since the grid condition is the same.

61

Figure 5.13. Battery inverter currents in stationary frame.

Figure 5.14. Grid current under 0.5% unbalanced grid voltage.

62

Figure 5.15. FFT analysis of grid current under 0.5% unbalanced grid voltage.
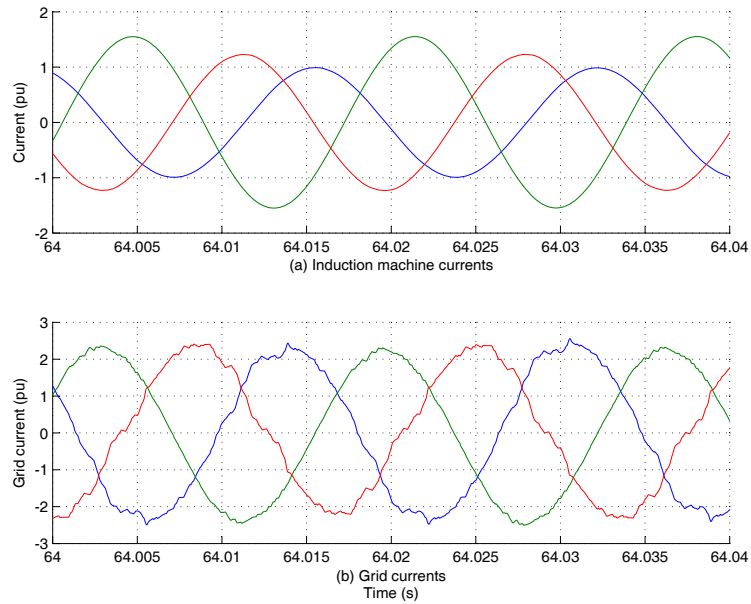
Figure 5.16. Induction machine and grid currents under 2% unbalanced grid voltage.

63
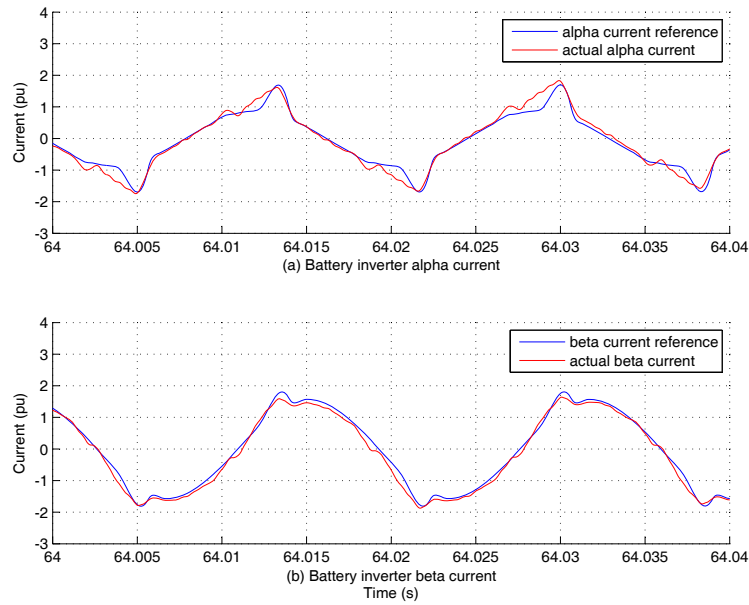
Figure 5.17. Battery inverter currents in stationary frame.

Fig. 5.17 demonstrates the battery inverter current in $\alpha\beta$ frame. The HC controller still works properly since the actual $\alpha\beta$ currents track their corresponding references exactly. Fig. 5.18 shows the details of grid phase A current comparing between HC controller disabled and enabled. The current distortion on highest and lowest peak has been improved considerably. Correspondingly, the THD of grid currents is 6.82% when both UC and HC controllers enabled while the THD is 14.21% when only UC controller is enabled. Fig. 5.19 shows the FFT analysis of grid current, and all of the odd order harmonics are below the limits with the controllers, however, 3rd, 5th and 7th order harmonics are larger than the limits when HC controller is not used.

5.3.3 Case III

The case III introduces a relative high level of unbalanced voltage, which is a 4% negative sequence voltage included. The negative sequence current in induction machine is as high as 48% of total current and implies huge unbalanced current existed, which is shown in Fig. 5.20 (a). However, the total grid current injected to PCC is still balanced and has limited amount of harmonics, which is shown in Fig. 5.20 (b). Due to high level of unbalanced grid voltage, the

64
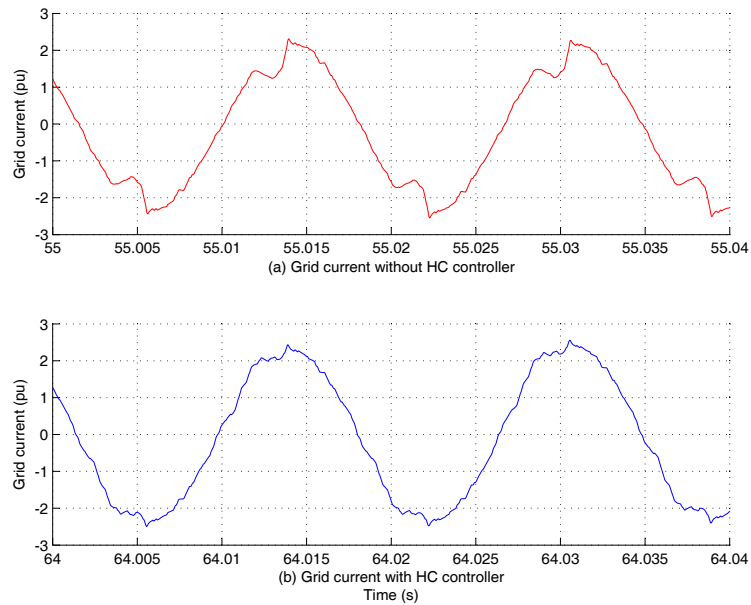
Figure 5.18. Grid current under 2% unbalanced grid voltage.
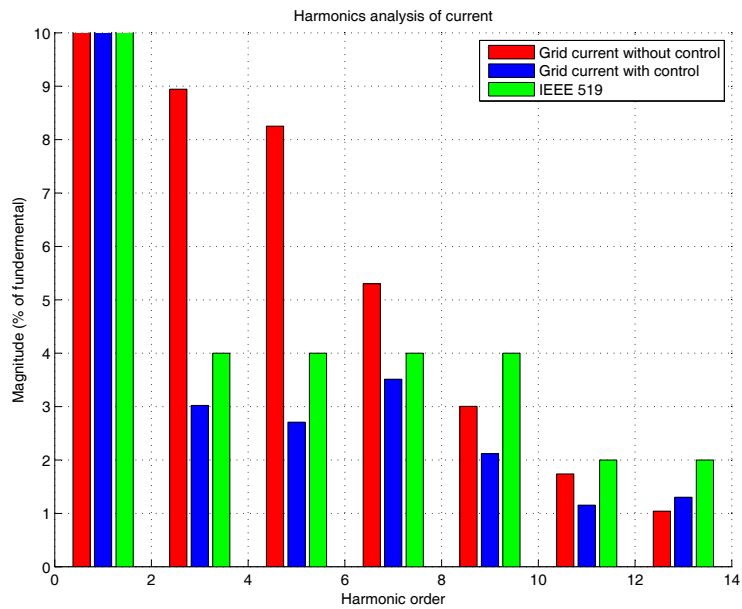
Figure 5.19. FFT analysis of grid current under 2% unbalanced grid voltage.

65
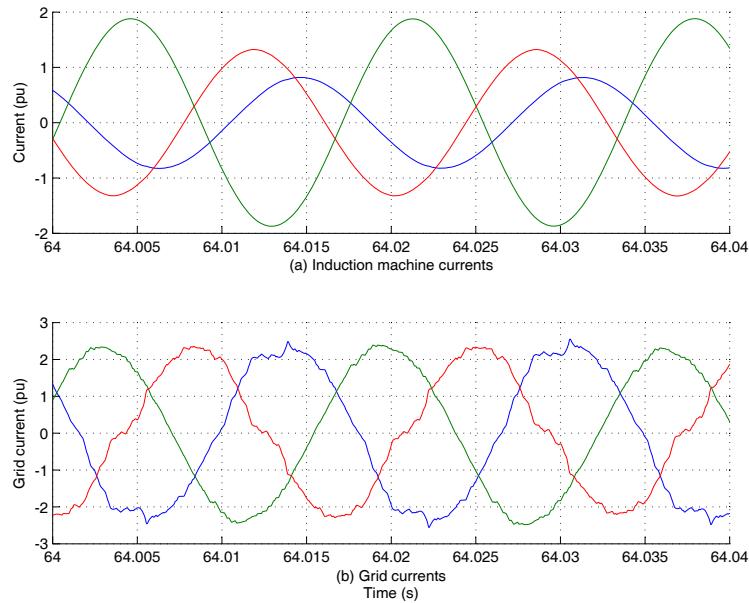
Figure 5.20. Induction machine and grid currents under 4% unbalanced grid voltage.

rectifier current distortion in Fig. 5.21 became worse, which implies the 3rd order harmonic current is larger and became more difficult to be eliminated.

Since the 3rd order harmonic current component became larger, the rectifier current became much more sharper. In order to compensate it, the battery current component at that frequency also needs to become more sharper. This phenomena can been found in Fig. 5.22 (a), the reference of α current has sharp distortion at each highest and lowest peak which is needed to compensate the 3rd order harmonic current component of induction machine. Since the changing rate at peak distortion is very high, the actual current can not track the reference instantaneously. Fig. 5.23 shows the grid phase A current, and small distortion at peak can still be found. The FFT analysis shown in Fig. 5.24 indicates the 3rd order harmonic current is around 5.6% and 5th order harmonic current is slightly higher than 4%, though those harmonic currents have been greatly improved comparing to the case without HC controller. The THD of grid current with controller is 8.89%, which is slightly higher than the 8% limit. The THD of grid current without controller is 15.08%. Therefore, when the grid voltage has higher level of negative sequence component, the

66
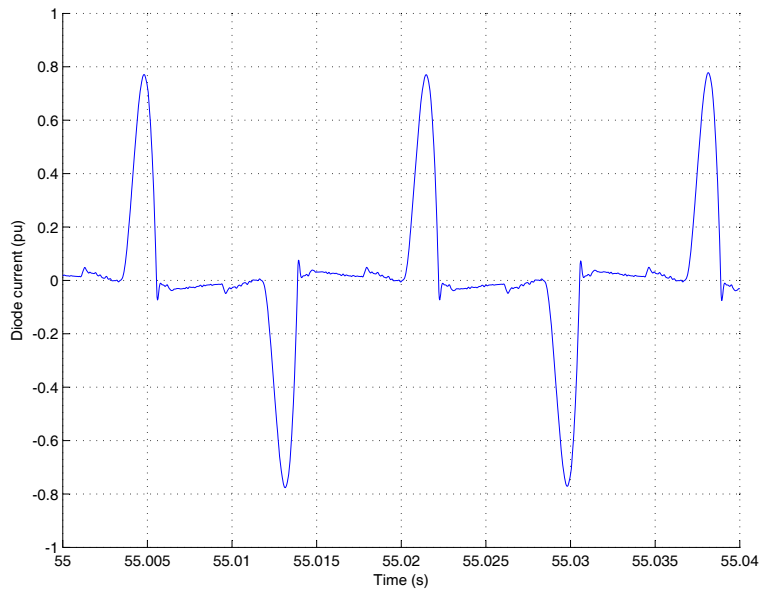
Figure 5.21. Rectifier current under 4% unbalanced grid voltage.
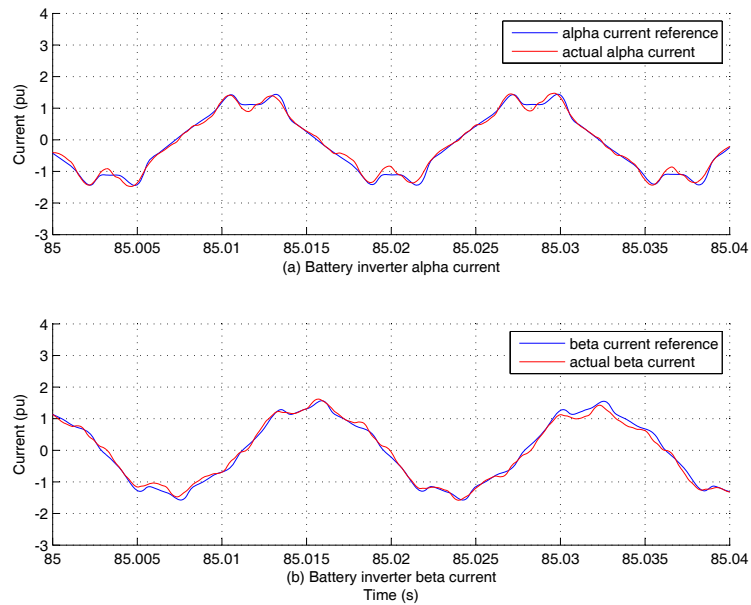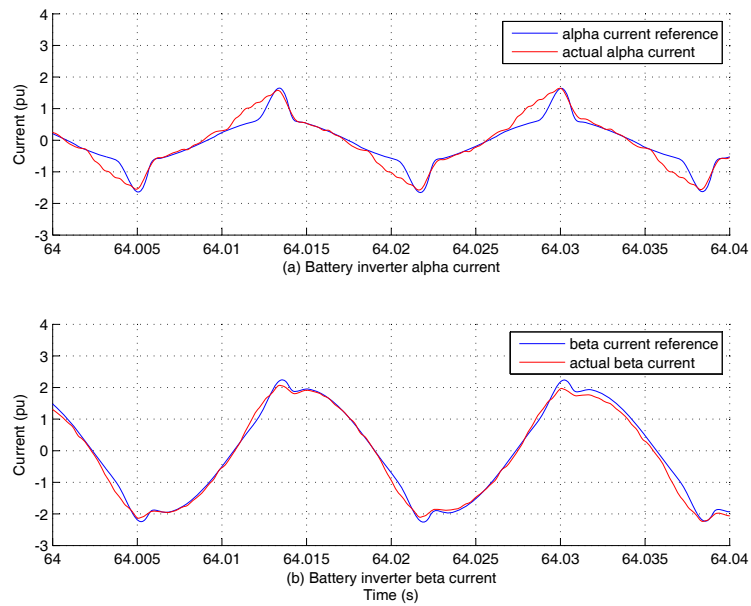

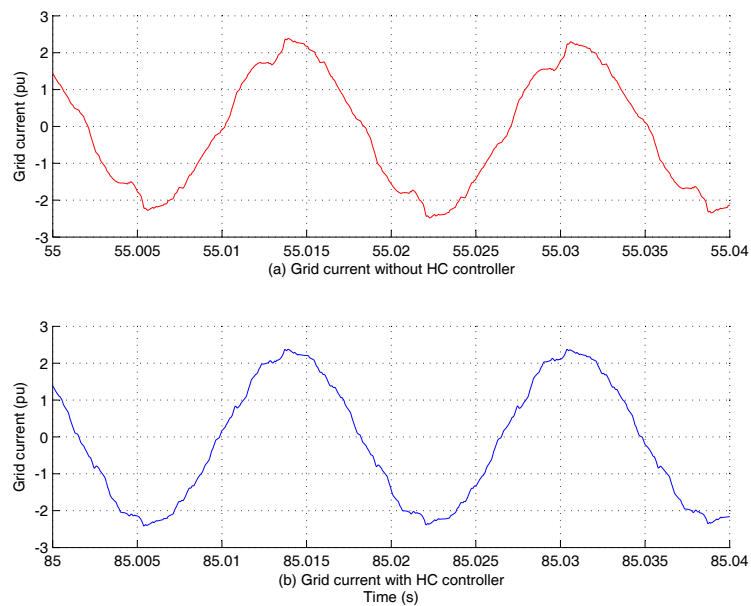Figure 5.22. Battery inverter currents in stationary frame.

67
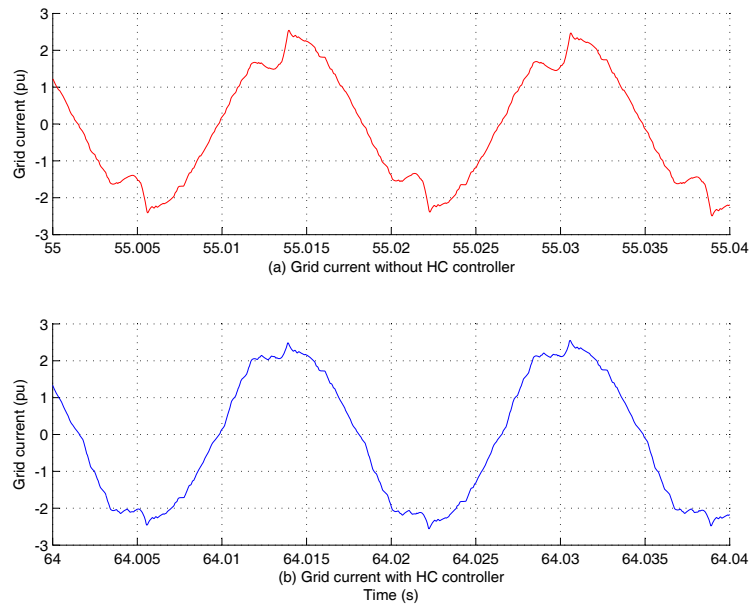
Figure 5.23. Grid current under 4% unbalanced grid voltage.
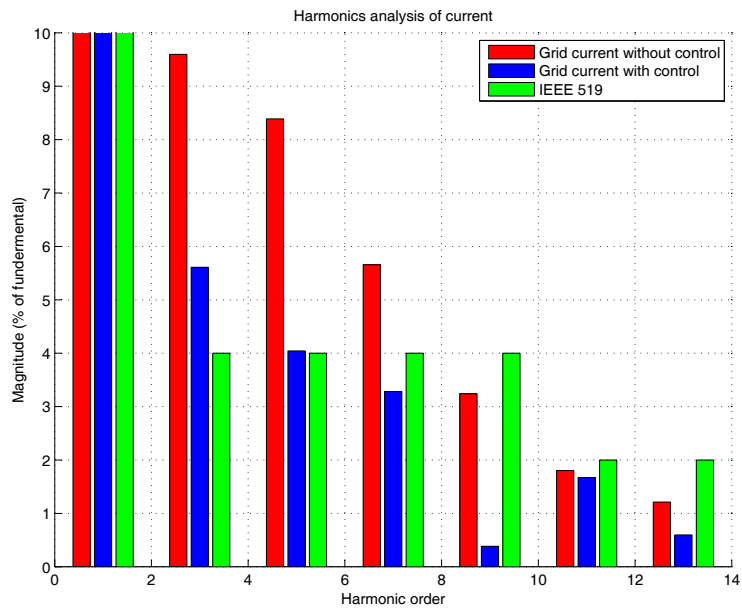
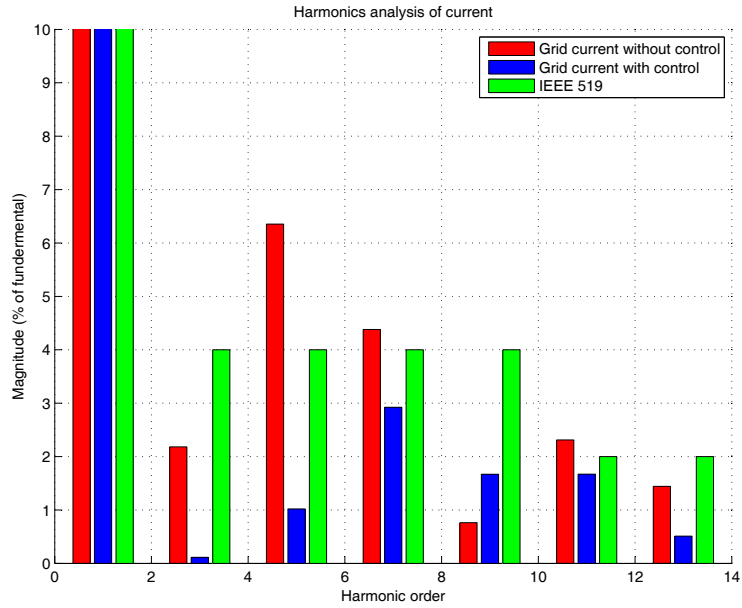Figure 5.24. FFT analysis of grid current under 4% unbalanced grid voltage.

68

rectifier load would generate more 3rd order harmonic current which may exceed the compensation capability of battery inverter. The THD of grid current may violate the limit set by the standard.

CHAPTER 6

SYSTEM IDENTIFICATION BASED VSC-HVDC DC VOLTAGE CONTROLLER DESIGN

VSC-HVDC is becoming a preferred solution to deliver renewable energy to main grids [92, 93, 94]. Proper controls are required for adequate operation of the VSC-HVDC. Depending on the function of each station, the converter station could operate at either power control or dc-link voltage control mode. dc-link control is important for power balance and fault ride through. Hence proper design of the dc-link voltage in a VSC-HVDC system is investigated in this chapter.

Typically, the controllers are PI controllers, are designed based on the transfer function of VSC model. [52, 53, 54, 55] derived the VSC models based on system parameters and basic circuit equations, which means the system variables need to be known in advance. [56] obtained the multi-terminal VSC-HVDC model via small signal analysis. [59] proposed methods to model power converters using reduced-order system.

Without knowing all parameters of the system, dynamic models can be obtained through system identification given input and output dynamic responses. MATLAB System Identification Toolbox is designed for such purpose and has been used in model identification. For instance, [60, 61] have proposed approaches to identify the model representation of dc-dc power converters via MATLAB System Identification Toolbox. [58] used MATLAB System Identification Toolbox to identify a linear model for a fuel cell system.

This chapter[1] proposes to use MATLAB system identification toolbox to identify the open-loop system model for dc-link voltage control design. The d-axis current reference is treated as the input while the dc-link voltage is treated as the output. With the simplified linear model determined from the toolbox, a dc-link voltage controller's parameters can be determined accurately. Simulation

---

[1]This chapter was published in North American Power Symposium (NAPS), 2012, vol., no., pp.1,6, 9-11 Sept. 2012. Permission is included in Appendix B.

results indicate that the identified model is accurate and the controller could meet the performance requirements [95].

6.1 System Model

6.1.1 System Topology

The VSC-HVDC system studied in this chapter is a two terminal system, which connects two ac grids. Fig. 6.1 depicts the structure of the two terminal VSC-HVDC system. One of the two grids is the sending end and the other is a receiving end, both are 230 kV, 60 Hz ac sources, and the capacity is 2000 MVA. The converter stations are modeled by two three-level dc/ac IGBT converters, and the PWM switching frequency is 1620 Hz. The π transmission cable model in SimPowerSystem library is used to represent the dc-link, and the cable length is set to 70 km. Table 6.1 shows the parameters of the above VSC-HVDC system. The two terminal VSC-HVDC system is bulit in SimPowerSystem with detailed power electronics converters.
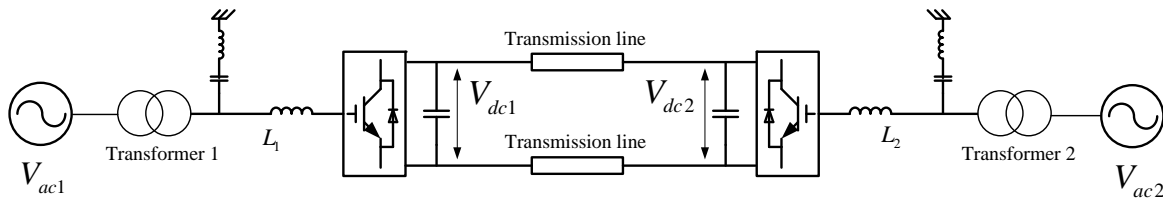
Figure 6.1. Topology of a two terminal VSC-HVDC system.

Table 6.1. Electrical parameters of the VSC-HVDC system

Quantity	Value
ac grid voltage	230kV (L-L RMS)
Coupling inductor	0.03ohm+0.02H
Transformer 1	230kV/100kV, 200MVA, leakage 8%pu
Transformer 2	230kV/100kV, 200MVA, leakage 8%pu
Transmission line	75km, (0.2568ohm+2mH+0.0086uF)/km
dc-link capacitor	700uF
dc-link voltage	250kV

www.manaraa.com

6.1.2 Control Modes

The two terminal VSC-HVDC system consists of one rectifier station and one inverter station respectively. Normally, the rectifier station operates at power control mode. At this mode, the station controls active power drawn from the ac grid, and controls the reactive power compensated to grid or controls the ac grid voltage directly. The inverter station operates at dc-link voltage control mode, which regulates the dc-link voltage at a specific level. Otherwise, the active power flow balance between two stations could not be maintained. As well as the rectifier station, the inverter station could also control the reactive power compensation or ac grid voltage if required.

6.1.2.1 Rectifier Station Control

Fig. 6.2 depicts an equivalent circuit of a VSC connected with a three-phase ac source. (6.1) describes the voltage and current relationship between ac sources and converter. Variables in the abc system in the above circuits can be transformed into a synchronous reference frame. The voltage and current relationship is shown in (6.2) and (6.3), where ω is the angular frequency of ac system, v_d, v_q, v_{d1}, and v_{q1} represent the d and q components of the PCC voltage (v_a, v_b, v_c)and VSC output voltage(v_{a1}, v_{b1}, v_{c1}), respectively, and i_d and i_q represent the d and q components of the current flowing between the ac system and the VSC. The powers could also be calculated in dq frame, which is shown in (6.4). In which, the d axis voltage is aligned with the phase A of the ac source voltages, which results the q axis voltage is equal to zero when no unbalance sequences exists. From (6.4), it is obvious that the active power is controlled by d axis current only, while the reactive power is controlled by q axis current only. The ac source voltages are assumed to be strong enough so that v_d is a constant. Therefore, the controller for rectifier station showed in Fig. 6.3 could be implemented.

$$\begin{cases} v_a = v_{a1} + i_a R + j\omega L \frac{di_a}{dt} \\ v_b = v_{b1} + i_b R + j\omega L \frac{di_b}{dt} \\ v_c = v_{c1} + i_c R + j\omega L \frac{di_c}{dt} \end{cases} \tag{6.1}$$

72
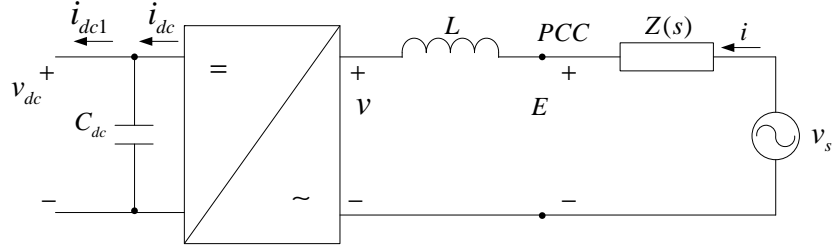
Figure 6.2. Equivalent model of a VSC connected with ac sources.
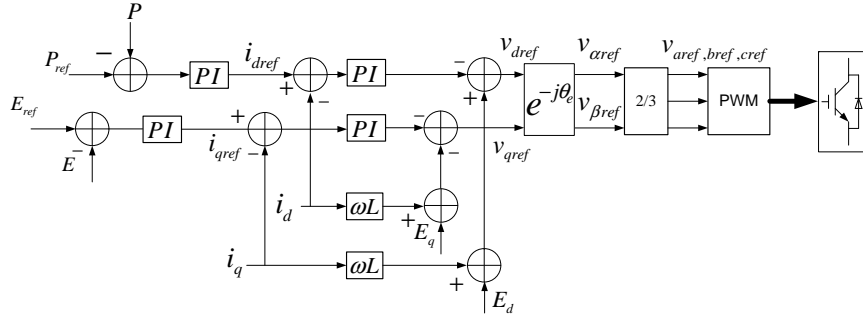
Figure 6.3. Controller of the rectifier station.

$$v_{d1} = -(Ri_d + L\frac{di_d}{dt}) + \omega_s Li_q + v_d \tag{6.2}$$

$$v_{q1} = -(Ri_q + L\frac{di_q}{dt}) - \omega_s Li_d \tag{6.3}$$

$$\begin{cases} p = v_d i_d \\ q = -v_d i_q \end{cases} \tag{6.4}$$

6.1.2.2 Inverter Station Control

The main function of inverter station is to regulate the dc-link voltage. The dynamics on dc capacitor is shown in (6.5), in which the term $v_d i_d$ is the active power transferred from grid, and which is equal to the active power on dc side if the losses on IGBTs are neglected. In fact, the controllers include two control loops, the outer control loop is dc-link voltage control loop. The dc voltage is measured and compared with reference, the resulting error is then sent to a *PI*

73

controller, and the output of which is the reference of d axis current. The inverter station could also compensate reactive power to the grid due to the advantage of IGBTs. In Fig. 6.4 (a), the magnitude of the PCC voltage is measured and compared with the command, the error signal is then the input of a PI controller, the output of which is the reference of q axis current. The inner control loops are the cross decoupled d, q current control loops, which is shown in Fig. 6.4 (a).

$$v_{dc}(C\frac{dv_{dc}}{dt} + i_{dc2}) = v_d i_d \rightarrow \frac{dv_{dc}}{dt} = \frac{v_d i_d}{v_{dc}C} - \frac{i_{dc2}}{C} \tag{6.5}$$

The control mechanisms described above are achieved via the well-known decoupled dq control algorithms [2]. The controllers include two control loops, depending on the stations, the outer control loop could be either a power control loop for rectifier station, or it could be a dc-link voltage control loop for inverter station. The inner control loops are the cross decoupled d, q current control loops.

The controllers essentially used are typical PI controllers in most cases. Therefore, two critical parameters need to be determined carefully, which are the proportional gain K_p and the integral gain K_i. However, due to the complexity of the VSC-HVDC system and the nonlinear effect introduced by power electronics devices, it is hard to directly derive the exact mathematical model of the system for controller design purpose. Many attempts have been done to explore the accurate model representation of the VSC-HVDC system, such as circuit equation derivations and small signal analysis [52, 53, 54, 55, 56].

6.2   System Identification

The major purpose of the chapter is to determine the parameters of dc-link voltage controller, which means the inner control loop has already been tuned in advance. The parameter selection of the current controller is made based on [1]. Fig. 6.4 (a) describes the detailed structure of the dc-link voltage controller, in which, the voltage controller is the object to be determined, and the other blocks could be considered as the plant to be controlled, which includes PLL, current controller, PWM generator, IGBT converters, and dc capacitor. All the blocks other than voltage

www.manaraa.com
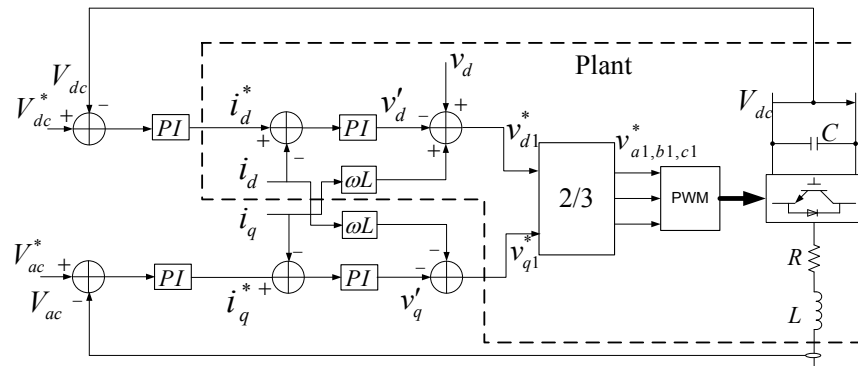
(a)
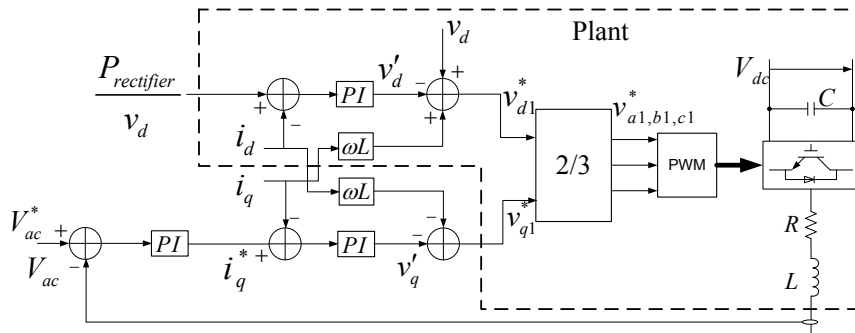
(b)

Figure 6.4. Detailed controller of the inverter station.

75

controller could be treated as one aggregated plant, as shown in Fig. 6.4 (a)'s dotted box, which looks like a black-box.

The input signal of the black-box is the d axis current, which represents the active power delivered from rectifier station, while the output signal of the black-box is simply the dc-link voltage. Since the inverter station is at open-loop control, the actual dc-link voltage is no longer the pre-defined value, it will automatically pump up to a level which could be able to satisfy the requirement of the ac side voltage of the IGBT converters. Fig. 6.4 (b) depicts the open-loop dc-link voltage controller of inverter station. Since the dc-link cable connects two converter stations, the interactions are critical for the system identification procedure. The input signal of the black-box, d axis current, should be calculated depending on the active power sent out from the rectifier station, which ensures the power balance. Otherwise, the system would be unstable, and the system characteristics could not be captured. (6.6) describes the derivation of the input signal i_d, in which, $P_{rectifier}$ is the active power sent from the rectifier station if the power loss on dc cable is neglected, v_{d_inv} is the actual d axis voltage of the ac side at inverter station.

$$i_d = \frac{P_{rectifier}}{v_{d\_inv}} \tag{6.6}$$

An active power step change in rectifier station is applied to test the dynamic response on dc-link voltage. From (6.6), the input signal tracks the active power change in rectifier station, the stability on dc-link voltage could be guaranteed. However, without dc link voltage feedback control, when the active power coming from the rectifier station goes up, the dc-link voltage would rise up and stay at a higher level due to the dynamic response. As a result, the dynamics on output signal corresponding to the input signal could be found.

Fig. 6.5 shows the step change on d axis current and the response on dc-link voltage. At 20 s, the active power changes from 1 pu to 1.5 pu, while it returns to 1 pu at 30 s. The output signal dc-link voltage v_{dc} rises up to 230 kV and decays to around 210 kV after several seconds, and it has an opposite response at 30 s when i_d decreases. With the system identification toolbox, the step up change on input signal and the corresponding output signal response is used to estimate the transfer function representation of the plant (from 19.9 s to 29.9 s). The step down response is
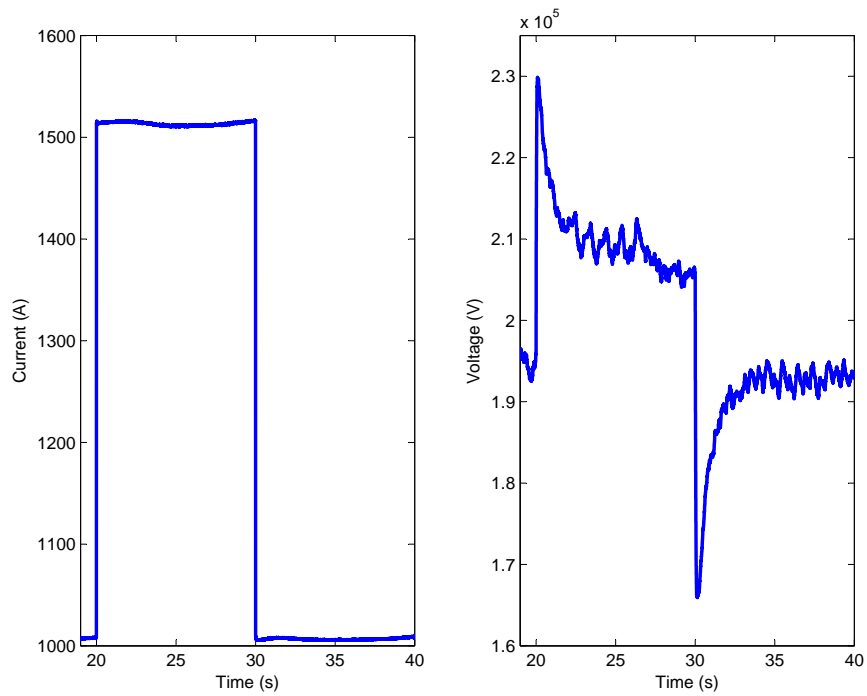
Figure 6.5. Active power step up and down responses.
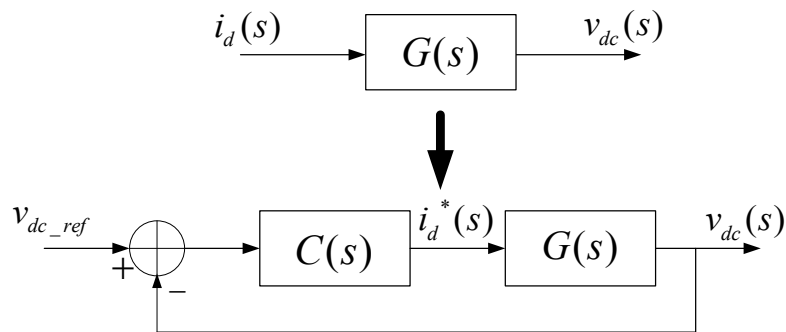
Figure 6.6. Open-loop plant and corresponding feedback controller.

77

used to verify the accuracy of the estimated transfer function (from 29.9 s to 39.9 s). The order of the transfer function is unknown before the estimation done. With System Identification Toolbox SIT, an initial guess of the order needs to be performed, after that, the order could be increased if the best fits is low, which indicates the accuracy of the estimated model. The increase of the order guess could stop if there is no significant improvement on best fits while order increasing. Fig. 6.7 illustrates the step responses of different order models and their best fits, which indicates order 6 is good enough to represent the black-box. Actually, since there is one inductor between converter and grid, one capacitor at dc side, and one smoothing inductor at dc cable, the order of the system should be at least three. And since the best fit of estimated system above order 6 is not improved that much, order 6 system is chosen as the estimated system. The black trace is the actual dc-link voltage due to a active power step down change in the VSC-HVDC model in SimPowerSystem, and the other color traces are the output signal waveforms of identified models. Therefore, the transfer function of dc-link voltage over d axis current could be obtained.
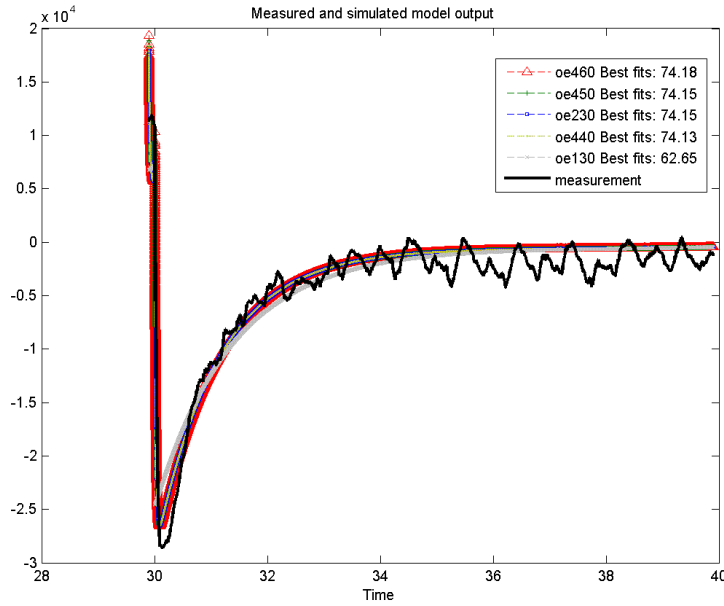
Figure 6.7. Identified dc-link models with various orders.

(6.7) shows the transfer function estimated by SIT, in which, $i_d(s)$ and $v_{dc}(s)$ are input and output signals respectively. The transfer function is the model representation of the black-box

78
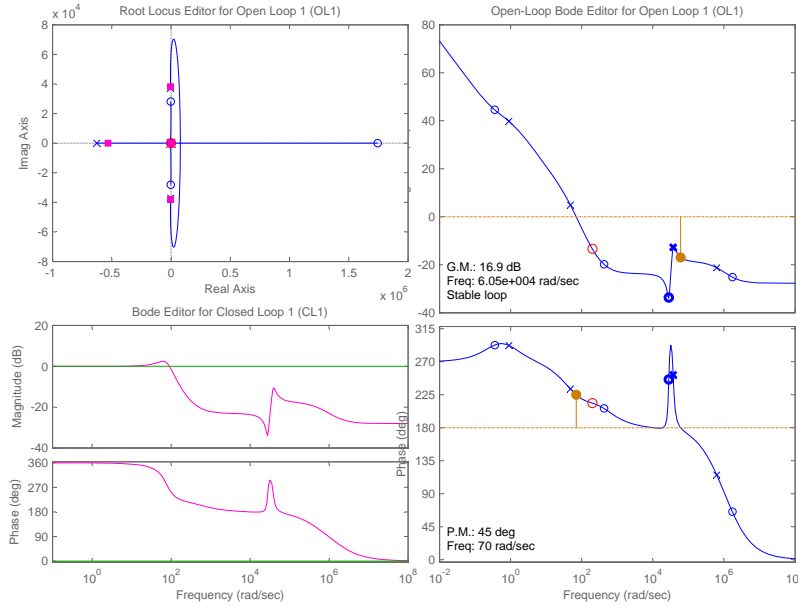
Figure 6.8. Controller characteristics plot of identified model.

shown in Fig. 6.4. The controller parameters design could be implemented via SISO tool in MATLAB, and the limits are able to be obtained thereafter.

$$G(s) = \frac{v_{dc}(s)}{i_d(s)} = \frac{4.848s^5 - 8.438e6s^4 - 2.659e10s^3}{s^5 + 6.342e5s^4 + 6.445e9s^3}$$
$$\frac{-6.69e15s^2 + 2.843e18s + 1.02e18}{+8.727e14s^2 + 4.292e16s + 3.781e16} \tag{6.7}$$

Fig. 6.6 shows the controller and the plant to be controlled, in which $G(s)$ is the estimated model obtained via SIT, and $C(s)$ is the controller to be designed, which is a typical PI controller, and (6.8) is the transfer function of $C(s)$. The open-loop system is the product of $C(s)$ and $G(s)$, hence, the root locus and bode plot could be drawn. As long as the bandwidth of controller and phase margin are selected, the controller parameters could be obtained by adjusting K_p and K_i until the bode plot of the open-loop system meets the requirements. Graphic control design tool could accelerate the procedure, such as the SISO toolbox in MATLAB. Fig. 6.8 plots the root locus of $C(s)G(s)$, and the open-loop and closed-loop bode plots of which are included as well.

79

Since the switching frequency is 1620 Hz, the current controller bandwidth is chosen at 150 Hz, which is around 10 times smaller. Based on the coupling inductor, the current controller parameters are calculated in (6.8), in which τ_i is $\frac{1}{150Hz}$ [1]. Therefore, K_{pc} and K_{ic} are 3 and 4.5 respectively. Since the current controller is at inner loop, the bandwidth should be considerably greater than the dc-link voltage controller. Subsequently, 15 Hz should satisfy those criterions and is chosen as the bandwidth of the dc-link voltage controller. Table 6.2 lists the designed controller parameters corresponding to three different bandwidth and phase margin combinations. A low phase margin which is 5 deg is used to test the low performance controller.

$$C(s) = \frac{K_p s + K_i}{s}, K_{pc} = \frac{L}{\tau_i}, K_{ic} = \frac{R}{\tau_i} \tag{6.8}$$

Table 6.2. dc-Link voltage controller parameters

Bandwidth	Phase margin	Parameters
70 rad/s	45 deg	$K_p = 0.2$, $K_i = 1.7$
90 rad/s	20 deg	$K_p = 0.4$, $K_i = 4.1$
90 rad/s	5 deg	$K_p = 0.4$, $K_i = 6.2$

6.3   Validation

Since the transfer function and the PI controller parameters have been obtained, a simple closed-loop system could be drawn in Simulink, which is shown in Fig. 6.6. The input signal is the dc-link voltage reference and the output signal is the dc-link voltage. A step up change on dc-link voltage reference is applied to observe the response on output signal in Fig. 6.6. The reference change is also applied to the actual VSC-HVDC model in SimPowerSystem, and the dynamic response on dc-link voltage is compared with the estimated system in Simulink. Fig. 6.9 illustrates the dc-link voltage behaviors with three cases comparison corresponding to three different sets of controller parameters. For the case with 45 deg phase margin, the mismatch between measured and estimated voltage is a little bit higher, it may because of the controller is well designed,
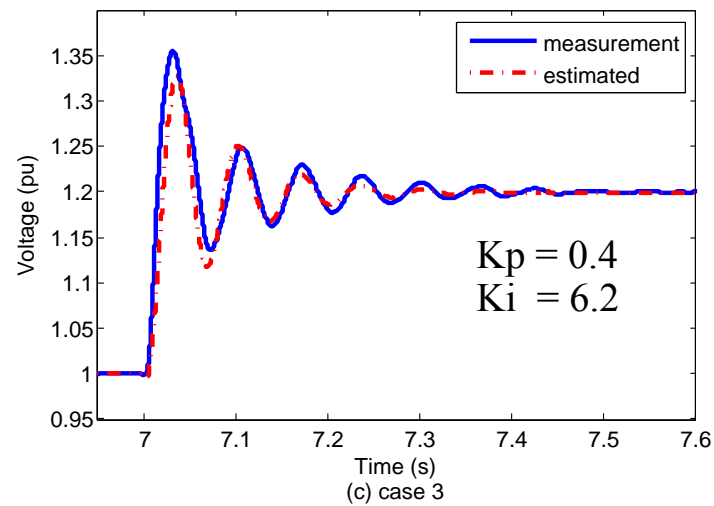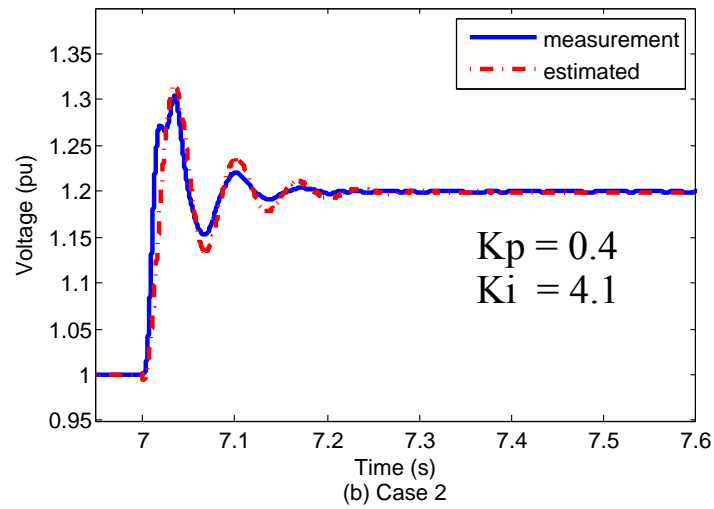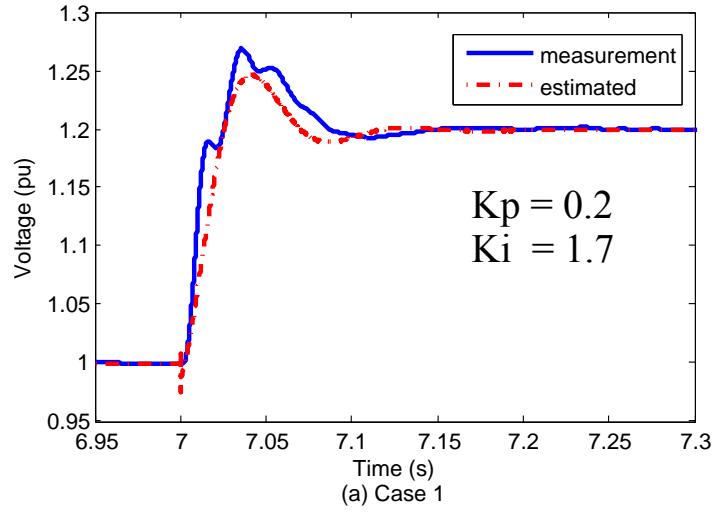
Figure 6.9. Validations of identified model with its controller under different combinations of parameters.

and the voltage is more sensitive to other system factors. The mismatch is becoming smaller for the 5 deg phase margin case, and it may because the controller is not well tuned which makes the voltage is more sensitive to the controller. The 5 deg phase margin significantly make the controller performance worse, which introduces more oscillations before reaching steady state. However, the actual dc-link voltage in VSC-HVDC model and the output signal of estimated model matches each other, though there are some small mismatches on peak values and settle times. The simulations verify the estimated model in (6.7) could accurately represent the actual VSC-HVDC system in Fig. 6.4, and the controller designed based on which could effectively regulate the dc-link voltage. The research could expand to hardware validation, since some details of the physical converter are not included in SimPowerSystem, such as the parasitic inductance and snubber circuit, the estimated system representation could be different.

CHAPTER 7

MODELING AND SIMULATION OF MULTI-TERMINAL HVDC FOR WIND POWER DELIVERY

VSC-HVDC transmission has the advantage to be easily implemented in multi-terminal topologies. The dc link voltage polarity can be kept the same for different power flow directions. This feature could benefit the grid integration of offshore wind farms, since the physical distance of each wind farm could be far and the grid integration station may have only few choices. The multi-terminal VSC-HVDC system could integrate several wind farms to one or multiple grid side converter station, which provides high flexibility for power system planning and construction [46, 47].

This chapter[1] will investigate modeling and simulation of a four terminal VSC-HVDC system under both normal and fault scenarios. The MHVDC system includes two DFIG wind farms. The control strategies of both WFVSC and GSVSC will be described. Simulations of the system are carried out in a Real-Time digital simulator RT-LAB. The system response under grid side ground fault is also studied, and an approach to mitigate the over-voltage during fault is proposed and tested [96].

7.1   System Model

7.1.1   System Topology

The multi-terminal VSC-HVDC system studied in this chapter consists of four terminals. Two terminals are connected to respective DFIG wind farms, and the other two terminals link to the main ac grids. Fig. 7.1 shows the topology of the system, in which, two wind farms are connected

---

[1]This chapter was published in Power Electronics and Machines in Wind Applications (PEMWA), 2012 IEEE, vol., no., pp.1,6, 16-18 July 2012. Permission is included in Appendix B.

83

to respective converter stations. The main grid is represented by a 230kV (L-L rms) voltage source V_{ac1} and V_{ac2}, which connect to the above two wind farms via long distance dc cables. Each segment of the transmission cable is 75km. Wind farm 1 consists of 50 units of DFIG, which has a nominal power rating of 2MW for each unit, while wind farm 2 is built up by 50 units of the same DFIG. Each wind farm can generate 100MW to the grid at nominal operation. Fig. 7.2 shows a DFIG wind turbine model used in this chapter, in which the RSC and GSC are rotor side converter and grid side converter respectively, both are IGBTs converters. The power rating of WFVSC is 100 MVA, and the nominal ac side voltage is 100 kV. The dc cables are 75 km and 50 km long for respective wind farms, and the reference voltage is set at 250 kV. The capacity of GSVSC is 200 MVA, and the grid is modeled as a 2000 MVA, 230 kV voltage source. They are connected through a 230 kV/100 kV transformer.
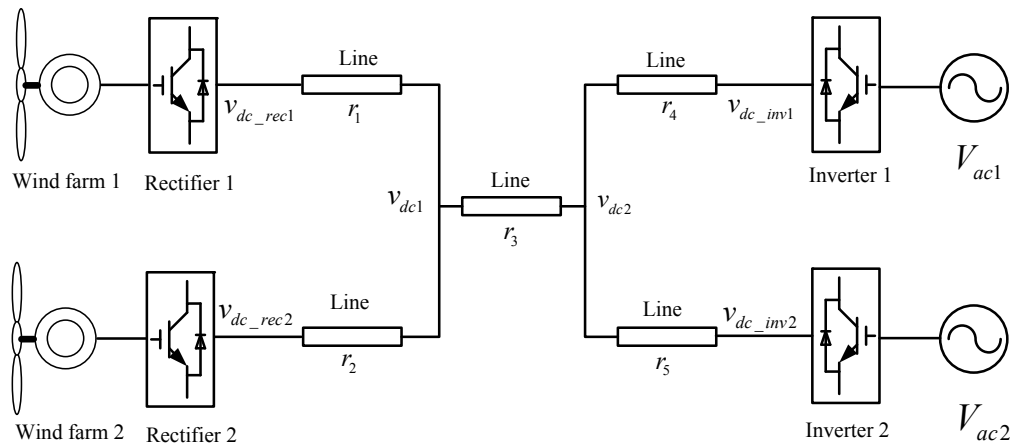
Figure 7.1. Topology of a multi-terminal VSC-HVDC system.

7.1.2 Control Modes

The control modes of the VSCs in Fig. 7.1 depend on the function of the converters. Generally, the converters at wind farm side operates at Vf control mode, which regulates the voltage and frequency of the ac side. Hence, the WFVSC can behave as an infinity bus, which could absorb whatever the active and reactive power generated by DFIGs. The GSVSC normally operates at dc-link voltage control mode, which controls the voltage of the dc cable [51]. As long as the power

84
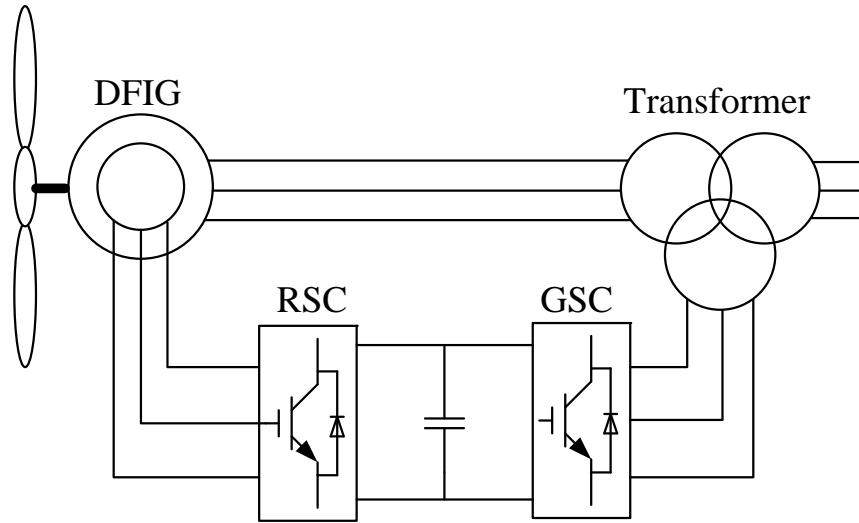
Figure 7.2. A DFIG wind turbine model.

balance is achieved, the dc voltage could be maintained at an appropriate value. The other control freedom could be either reactive power or ac voltage control, which normally compensate reactive power required by the ac grid.

7.1.2.1 GSVSC Control

The control modes of the VSCs in Fig. 7.1 depend on the function of the converters. Generally, the converters at wind farm side operates at vf control mode, which regulates the voltage and frequency of the ac side. Hence, the WFVSC can behave as an infinity bus, which could absorb whatever the active and reactive power generated by DFIGs. The GSVSC normally operates at dc-link voltage control mode, which controls the voltage of the dc cable [51]. As long as the power balance is achieved, the dc voltage could be maintained at an appropriate value. The other control freedom could be either reactive power or ac voltage control, which normally compensate reactive power required by the ac grid. Since there are two GSVSCs, a dc voltage droop control method is used to regulate the respective dc voltages and active powers. (7.1) and (7.2) describe the dc voltage controller with droop control, in which, the coefficients k_1 and k_2 determines the power ratio between inverter stations 1 and 2. Combining (7.1), (7.2), and (7.3) yield the ratio of power

85

which depicted in (7.4) [51, 97]. In this chapter, k_1 and k_2 are set to identical so that the two inverter stations would split the active powers from rectifier stations equally.

$$v_{dc\_inv1} = v_{dc0} + k_1 i_{dc\_inv1} \tag{7.1}$$

$$v_{dc\_inv2} = v_{dc0} + k_2 i_{dc\_inv2} \tag{7.2}$$

$$v_{dc2} = v_{dc\_inv1} + r_4 i_{dc\_inv1} = v_{dc\_inv2} + r_5 i_{dc\_inv2} \tag{7.3}$$

$$\frac{P_{inv1}}{P_{inv2}} = \frac{v_{dc\_inv1} i_{dc\_inv1}}{v_{dc\_inv2} i_{dc\_inv2}} \approx \frac{i_{dc\_inv1}}{i_{dc\_inv2}} = \frac{k_2 + r_5}{k_1 + r_4} \tag{7.4}$$

Once the dc voltage reference for each GSVSC such as v_{dc_inv1} and v_{dc_inv2} are derived, a dc-link voltage controller is required to regulate the dc voltage at each terminal. The control mechanisms described are achieved via the well-known decoupled dq control algorithms [2]. The controller includes two control loops, the outer control loop is dc-link voltage control loop. The dc voltage is measured and compared with reference, the resulting error is then sent to a PI controller, and the output of which is the reference of d axis current. The grid side converter could also compensate reactive power to the grid due to the advantage of IGBTs. In Fig. 7.3, the magnitude of the PCC voltage is measured and compared with the command, the error signal is then the input of a PI controller, the output of which is the reference of q axis current. The inner control loops are the cross decoupled d, q current control loops, which is shown in Fig. 7.3.

7.1.2.2   WFVSC Control

The WFVSC control adpots vf control which regulate the ac voltage and frequency and is introduced in Chapter 3.
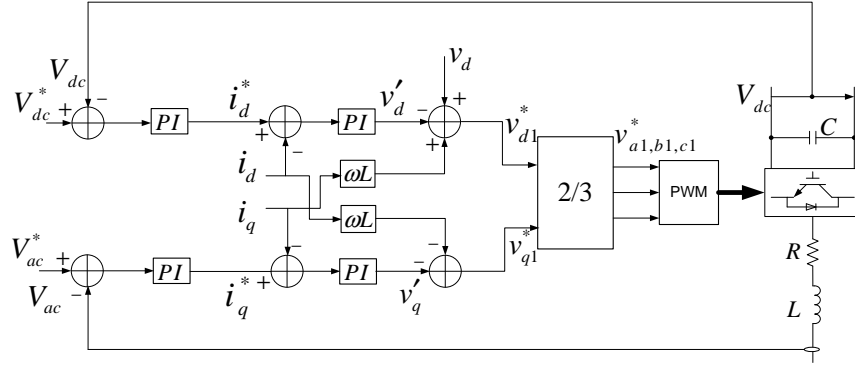
Figure 7.3. dc-link voltage controller.

7.1.3 Grid Fault Operation

In case of any potential fault at grid side, the performance and stability of the VSC-HVDC system could be affected. In this chapter, a three-phase ground fault at grid side is studied. Since the three-phase ground fault at grid side could lead to a huge voltage sag, the power generated by wind farms is difficult to sent to grid continuously. The response at wind turbines is much slower than the electrical fault, which implies the active power generation is still almost the same with the instance before fault, hence decreasing the power generation of wind turbine is not an ideal choice. If there is no proper action taken, the dc-link voltage would rise up since the active power has no where to go. This chapter proposes an approach to prevent the dc-link voltage overshoot, which is shown in Fig. 7.4. At the dc side of the GSVSC, a switch and a dc/dc converter are used to connect a battery and the dc-link. Once the ground fault at grid side is detected, the switch will be closed to let the excessive active power to be stored in the battery through a dc/dc converter. Fig. 7.5 depicts the dc/dc converter topology and control strategy for the battery. In which, the converter is controlled by a PWM regulator, when the up IGBT switch is turned on, the down IGBT switch is turned off, and the modulation index m is chosen at 0.2. The output voltage of the dc/dc converter is expressed in (7.5). The battery model in this case is modeled as a constant voltage source, therefore, the dynamics of SOC is neglected.

$$v_{out} = \frac{1 + m}{2} v_{dc} \tag{7.5}$$

87

www.manaraa.com
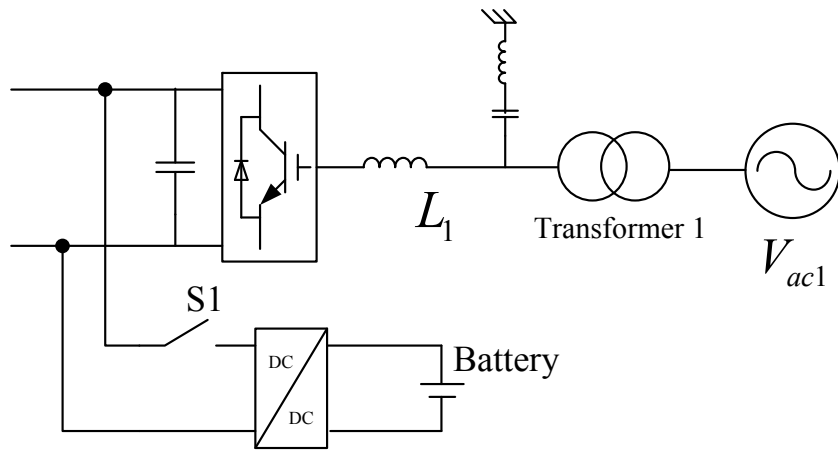
Figure 7.4. An approach to prevent the dc over-voltage after grid fault.
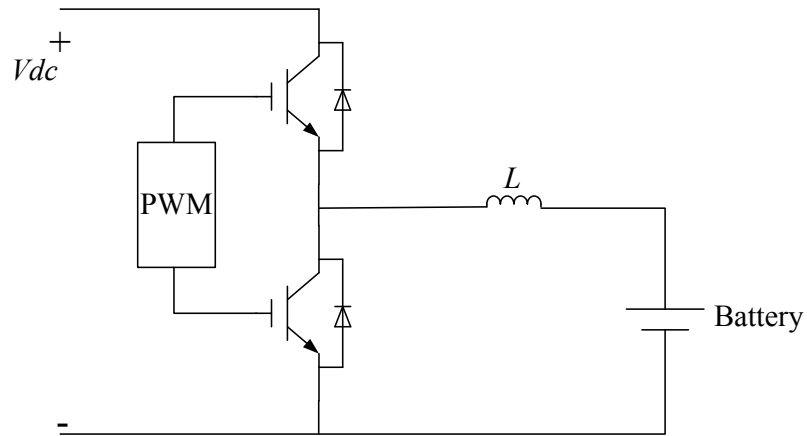
Figure 7.5. dc/dc converter topology and control for the battery.

88
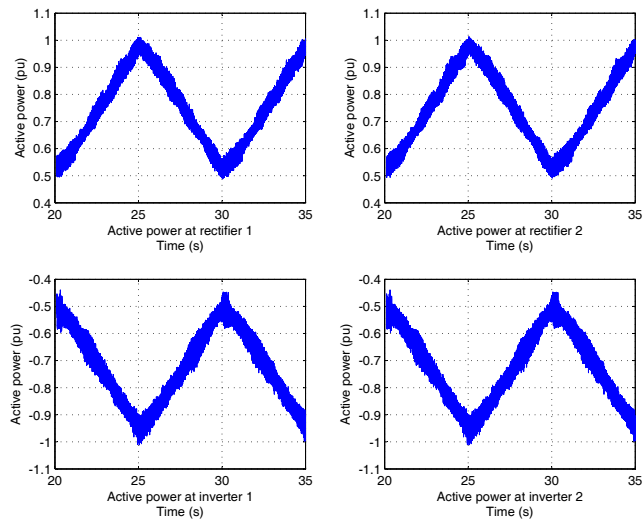
Figure 7.6. Active power of rectifier and inverter stations.
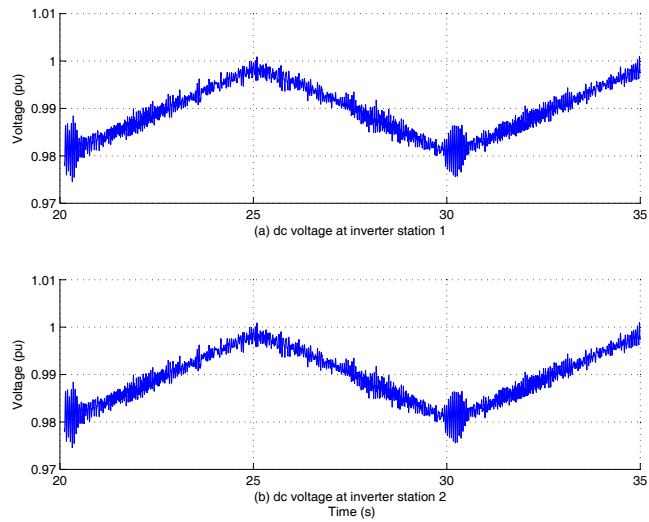
Figure 7.7. dc voltage of inverter stations.

89
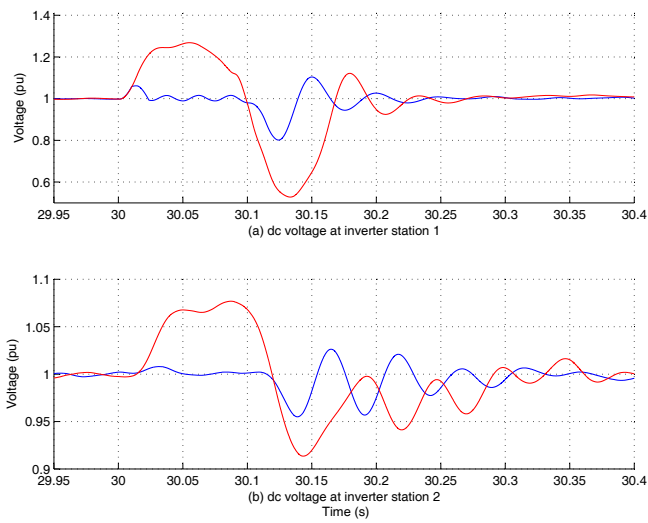
Figure 7.8. dc voltage of inverter stations during ac fault.
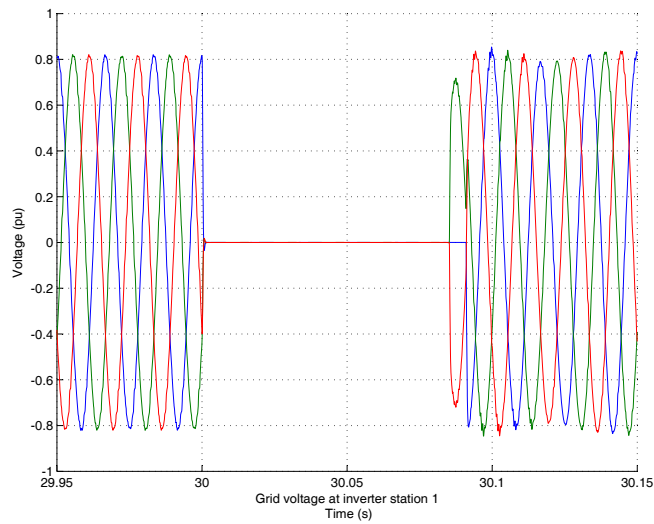
Figure 7.9. Grid voltage of inverter station 1 during ac fault.

90
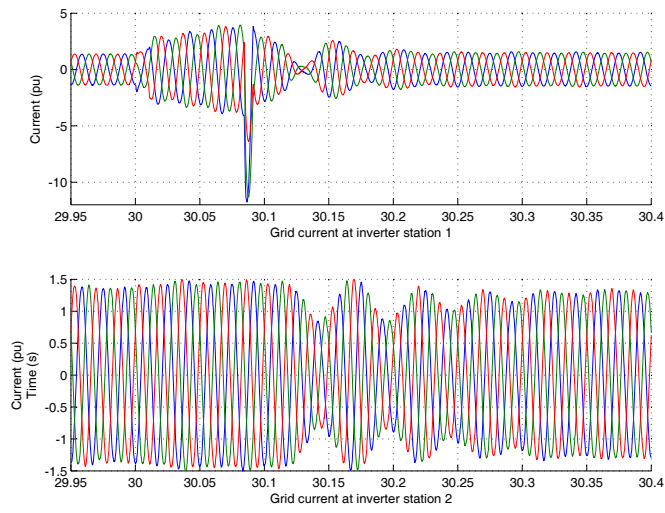
Figure 7.10. Grid current of inverter stations during ac fault.
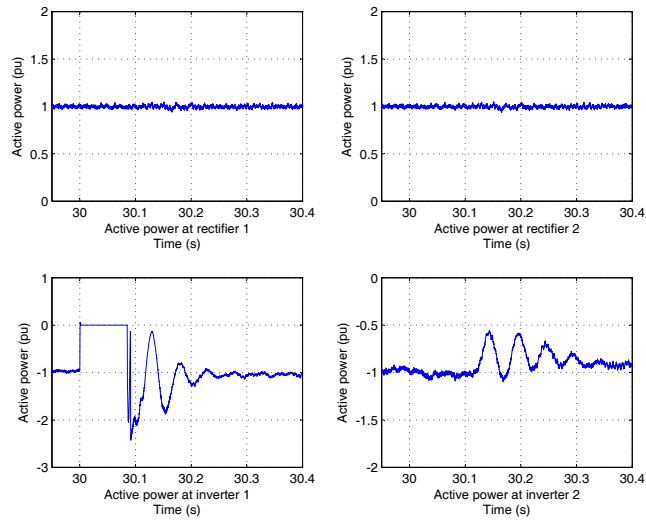
Figure 7.11. Active power of rectifier and inverter stations during ac fault.

91

7.2 Simulation

System evaluations are carried out in RT-LAB, which is shown in Fig. 5.10. The system is tested both on normal operation and fault operation. For normal operation, the wind speed varies with time, and therefore the active power generated by DFIGs varies. The system response are observed, and verified the power balance within VSC-HVDC. For fault operation, a three-phase ground fault was applied at grid side, and lasted 5 cycles. An over-voltage on dc-link was found during fault, which may damage the physical dc capacitor and cables. An approach to limit the overshoot is proposed and tested, which effectively mitigate the over-voltage.

7.2.1 Normal Operation

Ramp changes on wind power are tested for normal operation, and the results are shown in Fig. 7.6 and Fig. 7.7. In ramp up test, from 20s to 25s, the active power of WF1 is increased from 0.5pu to 1pu (1pu=100MW), while the active power of WF2 is increased from 0.5pu to 1pu from 20s to 25s as well. The total power transferred to grid is correspondingly increased. In ramp down test, from 25s to 30s, the active power of WF2 is decreased from 1pu to 0.5pu, while the active power of WF2 is decreased from 1pu to 0.5pu from 25s to 20s as well. Fig. 7.6 shows the power response at rectifier stations and inverter stations. The power sent to grid varies along with the change at rectifier stations.

The dc voltage profile at each inverter station is depicted in Fig. 7.7. Since the droop control method is adopted, the dc voltage is no longer a constant but depends on the active power flow. The dc voltage at each inverter station varies at the same pace because the droop coefficients k_1 and k_2 are set to identical.

7.2.2 Grid Fault Operation

For fault operation, a three-phase ground fault was applied at grid side of inverter station 1, and lasted 5 cycles. An over-voltage on dc-link was found during fault, which may damage the physical dc capacitor and cables. An approach to limit the overshoot is proposed and tested, which effectively mitigate the over-voltage. Fig. 7.8 shows the dc voltage at two inverter stations with

92

and without fault control respectively. Obviously, the dc voltage overshoot at inverter station 1 reaches almost 30% without fault control, and the dc voltage overshoot reaches 7.5% at inverter station 2. Contrarily, the dc voltage overshoot is limited below 10% at inverter station 1 and 3% at inverter station 2 respectively. Normally, the fault could be cleared after several cycles in power system, which is 5 cycles in this case. Therefore, the capacity of the battery does not to be very high. In case the fault is permanent, the battery could also be used to store the power for a short period, and the wind turbines and other components could have enough time to turn off without damages.

CHAPTER 8

AC IMPEDANCE BASED RESONANCE ANALYSIS IN A VSC-HVDC SYSTEM

Harmonic resonances can impact the power quality and the power transfer level of VSC-HVDC system. Normally, harmonics generated by switching sequences could be eliminated by ac filters. However, there are low frequency harmonic resonances due to the interaction of ac grid and VSC controllers. Those resonances are not easy to be filtered out. Though harmonic resonances have been examined in VSC interfaced ac grids in [98, 99, 100, 63], a comprehensive examination of the both ac systems (the rectifier side and the inverter side) has not been seen in the literature. It will be the objective of this chapter[1].

Since harmonic resonances are related to electrical systems mainly, impedance or admittance model based analysis is feasible in understanding the phenomena. In [101, 100, 63], impedance models of grid-connected inverters are developed for resonance analysis. [101, 100] developed impedances models of converters with only the inner current control loops considered. The outer control loops are ignored. Investigation shows that grid inductor, shunt capacitor and PLL have impact on harmonic resonances.

Impedance models of the VSC converter with inner current control and outer dc/ac voltage control loops are developed in [63]. Resonance stability is studied for both power flow direction. The studied ac grid is represented by a series RL circuit. It is stated in [63] that for the interaction of a converter and the grid impedance, with outer loop ignored, instability cannot be detected. With the outer control loop and PLL considered, instability can be detected. Therefore, modeling of the outer control loops is important.

---

[1]This chapter was published in Power Delivery, IEEE Transactions on, vol.28, no.4, pp.2209,2216, Oct. 2013. Permission is included in Appendix B.

In a VSC-HVDC system, there are two converters and each has its own control strategies. The rectifier controls power flow while the inverter controls dc-link voltage [1]. [63] studied only the interactions of the inverter and ac grid. The paper also assumes that the integral coefficients of converter PI controllers are equal to zero. In many literatures, the integral gains are greater than the proportional gains [102, 103].

In this chapter [104], resonance stability will be investigated for the two ac systems (the rectifier side ac grid and the inverter side ac grid). Typical VSC-HVDC controls will be adopted and impedance models of the systems will be developed with the inner and outer converter control loops included. Nyquist stability criterion and impedance frequency responses will then be applied to detect resonances. Impacting factors on stability such as feed-forward filter structure, line length and power transfer levels will be identified.

8.1 System Model

A VSC-HVDC system is presented in Fig. 8.1, where the basic controller for the rectifier and inverter stations are also presented. Normally, power is sent from the rectifier station to the inverter station. Power control is implemented at the rectifier station, while the inverter station controls dc-link voltage to ensure power balance. An advantage of VSC-HVDC over LCC-HVDC is its reactive power compensation capability, which is provided by the reactive power controller or ac voltage controller.

Table 8.1. System parameters of VSC-HVDC model

Quantity	Value
ac system line voltage	100kV
ac system frequency	60Hz
Grid impedance	0.02H/0.012H
Grid filter capacity	18Mvar
Grid filter tuning frequency	1620Hz
dc rated voltage	250kV
dc cable parameters	$0.0139\Omega/km$, $0.159mH/km$, $0.231\mu F/km$
dc cable length	20km
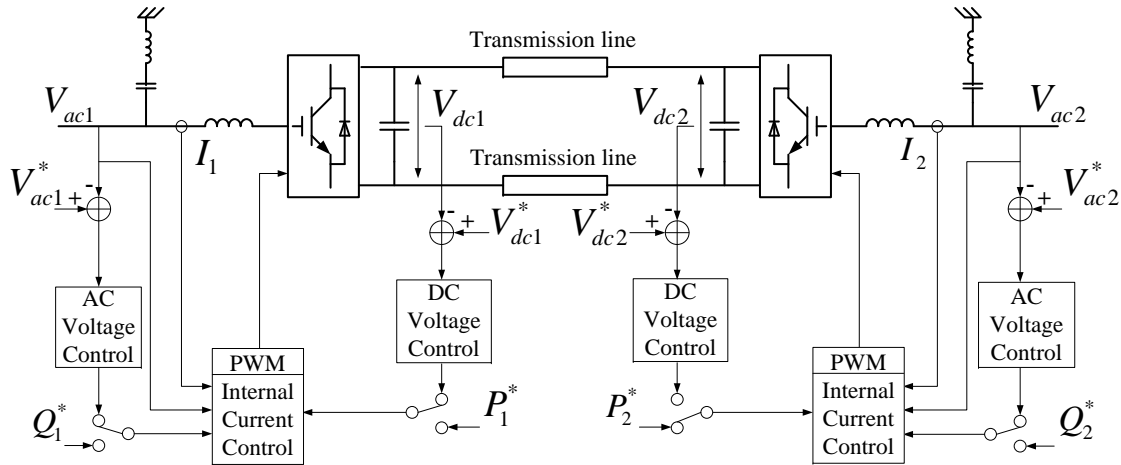
Figure 8.1. A two-terminal VSC-HVDC system.

For a balanced three-phase system, Fig. 8.2 shows the equivalent circuit of a VSC connecting with an ac grid via a coupling inductor L, where the resistor is neglected. The ac grid is modeled as an ac voltage source v_s with an impedance $Z(s)$. (8.1) describes the voltage and current relationship between grid and converter in time domain and represented in the dq frame. The letter with upper-line represents complex space vector, $e.g.$, $\overline{v} = v_d + jv_q$ and $\overline{i} = i_d + ji_q$. The angular speed within grid reference frame is ω_1, which is a constant throughout this chapter.
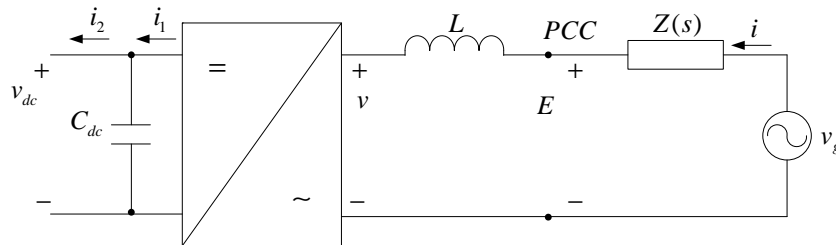
Figure 8.2. Circuit model of a VSC and ac grid.

Table 8.2. Parameters of individual VSC

Quantity	Value
Switching frequency	1620Hz
Grid filter	0.04H
dc capacitor	96μF

96

$$L\frac{d\bar{i}}{dt} + j\omega_1 L\bar{i} = \overline{E} - \overline{v} \tag{8.1}$$

where E and v are the PCC voltage and the converter output voltage.

8.1.1 Impedance Models

8.1.1.1 Rectifier Station

The current control loop will be analyzed in order to derive impedance model. The VSC-HVDC system consists of two terminal stations, one is the rectifier station and the other is the inverter station. Fig. 8.3 presents the controller of the rectifier station, in which active power P_{ref} and reactive power Q_{ref} are to be regulated.
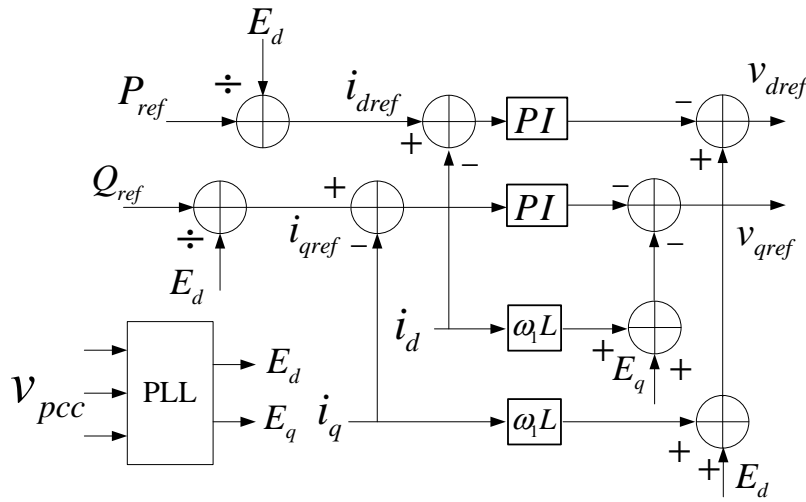
Figure 8.3. Controller of the rectifier station.

Depending on the requirements of application, the reactive power control could be substituted with ac grid voltage control. v_{dref} and v_{qref} are the converter output voltages and could be derived as (8.2), which is essentially the inner current control loop.

$$\begin{aligned}
\overline{v_{ref}} = & -(k_p + \frac{k_i}{s})(\overline{i_{ref}} - \bar{i}) - j\omega_1 L\bar{i} \\
& + \frac{\omega_0^2}{s^2 + 2\xi\omega_0 s + \omega_0^2}\overline{E}
\end{aligned} \tag{8.2}$$

97

The feed-forward items E_d and E_q are the PCC voltage measured in the dq frame and obtained through a filter. A second-order filter is included in (8.2), and the transfer function is shown in (8.3). Another option is first order filter, and the comparison of the two filters on resonance stability is conducted in Section 8.2.

$$F_{2nd}(s) = \frac{\omega_0^2}{s^2 + 2\xi\omega_0 s + \omega_0^2} \tag{8.3}$$

where ω_0 is the cut-off frequency (1000 Hz) and ξ is the damping factor $(\frac{1}{\sqrt{2}})$.

The controller utilizes PI controllers:

$$F_c(s) = k_p + \frac{k_i}{s}. \tag{8.4}$$

Rearranging (8.2) leads to (8.5),

$$\overline{i^c} = g_c(s)\overline{i_{ref}} + y_i(s)\overline{E^c} \tag{8.5}$$

where

$$\begin{cases} g_c(s) = \frac{k_p s + k_i}{Ls^2 + k_p s + k_i} \\ y_i(s) = \frac{s^2(s + 2\xi\omega_0)}{(Ls^2 + k_p s + k_i)(s^2 + 2\xi\omega_0 s + \omega_0^2)} \end{cases} \tag{8.6}$$

(8.5) describes the relationship of the current $\overline{i^c}$ in terms of $\overline{i_{ref}}$ and $\overline{E^c}$. Alternatively, (8.5) could be written in matrix form (8.7).

$$\overline{\mathbf{i}^c} = \begin{bmatrix} g_c(s) & 0 \\ 0 & g_c(s) \end{bmatrix} \overline{\mathbf{i}_{ref}} + \begin{bmatrix} y_i(s) & 0 \\ 0 & y_i(s) \end{bmatrix} \overline{\mathbf{E}^c} \tag{8.7}$$

where $\mathbf{f} = [f_d, f_q]^T$ and f stands for current or voltage symbol.

Power control loop is analyzed as follows. The rectifier station controls the active power transferred from the left-hand side grid to the converter, which is the outer control loop in dual dq control loops. Equation (8.8) computes the d axis current reference that controls the active power flow,

98

$$i_{dref} = \frac{P_{ref}}{E_d} = \frac{P_{ref}}{E_f} \tag{8.8}$$

where E_f is the d-axis PCC voltage after a filter.

$$E_f = F_{2nd}(s)\,|E| \tag{8.9}$$

The small signal representation of d axis current reference is then expressed as follows.

$$\Delta i_{dref} = -\frac{P_{ref}}{E_0^2} F_{2nd}(s) \Delta E_d \tag{8.10}$$

where E_0 is the rectifier PCC steady-state voltage. Since the direct reactive power compensation control is used throughout this chapter, the q axis current reference can be derived similarly as above.

$$\begin{cases} i_{qref} = -\dfrac{Q_{ref}}{E_d} = -\dfrac{Q_{ref}}{E_f} \\[2mm] \Delta i_{qref} = \dfrac{Q_{ref}}{E_0^2} F_{2nd}(s) \Delta E_d \end{cases} \tag{8.11}$$

Combining (8.10) and (8.11) leads to (8.12).

$$\overline{\Delta i_{ref}} = \underbrace{\begin{bmatrix} -\dfrac{P_{ref\_rec}}{E_0^2} F_{2nd}(s) & 0 \\[3mm] \dfrac{Q_{ref}}{E_0^2} F_{2nd}(s) & 0 \end{bmatrix}}_{G_{Ei\_rec}(s)} \overline{\Delta E} \tag{8.12}$$

The input admittance of ΔE and Δi is then expressed as.

$$\begin{aligned} Y_{rec}(s) &= Y_i(s) + G_c(s)G_{Ei}(s) \\[2mm] &= \begin{bmatrix} y_i(s) - \dfrac{P_{ref}}{E_0^2} F_{2nd}(s) g_c(s) & 0 \\[3mm] \dfrac{Q_{ref}}{E_0^2} F_{2nd}(s) g_c(s) & y_i(s) \end{bmatrix} \end{aligned} \tag{8.13}$$

99

8.1.1.2 Inverter Station

The dc voltage control analysis is implemented as follows. The inverter station regulates the dc-link voltage and maintains the active power balance. The controller is depicted in Fig. 8.4, which consists of two control loops. The inner current control loop is identical to the rectifier station shown in Fig. 8.3, whereas the outer loop is replaced by a dc voltage controller. The dc voltage controller $F_{dc}(s)$ is a typical PI controller shown in (8.14).
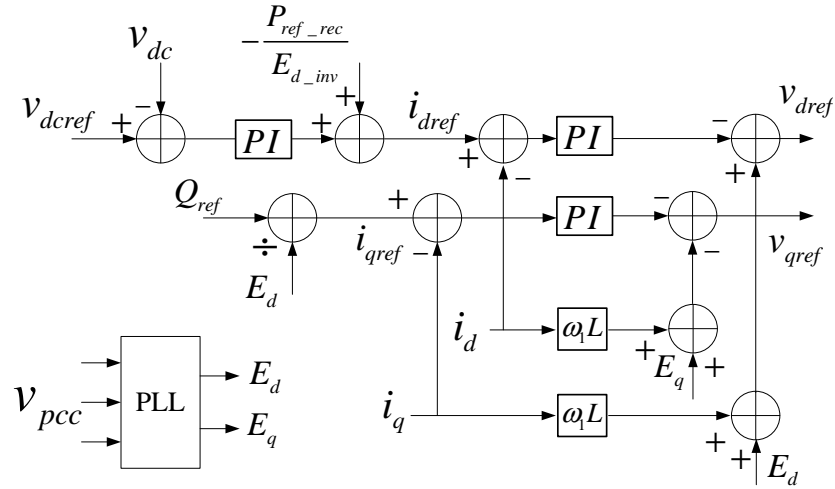
Figure 8.4. Controller of the inverter station.

Table 8.3. Parameters of controllers

Quantity	Value
Current controller	$k_p=50$, $k_i=100$
dc-link voltage controller	$k_p=0.04$, $k_i=0.2$

$$F_{dc}(s) = k_{pdc} + \frac{k_{idc}}{s} \tag{8.14}$$

A feed-forward item $-P_{ref\_rec}/E_{d\_inv}$ is applied to improve the controller dynamic performance. Hence, the d-axis current reference could be established as follows.

$$i_{dref} = (k_{pdc} + \frac{k_{idc}}{s})(v_{dcref} - v_{dc}) - \frac{P_{ref\_rec}}{E_{d\_inv}} \tag{8.15}$$

100

The small signal model of the d-axis current reference is expressed in (8.16),

$$
\begin{aligned}
&i_{dref0} + \Delta i_{dref} \\
&= (k_{pdc} + \frac{k_{idc}}{s})(v_{dcref} - v_{dc0} - \Delta v_{dc}) - \frac{P_{ref\_rec}}{E_{d\_inv}}
\end{aligned}
\tag{8.16}
$$

It can be assumed that $i_{dref0} = -P_{ref\_rec}/E_{d\_inv}$, since the active power delivered by inverter station is the same amount of rectifier station sent if power loss is neglected. The linear model (8.17) is then obtained.

$$
\Delta i_{dref} = - \underbrace{(k_{pdc} + \frac{k_{idc}}{s})}_{F_{dc}(s)} \Delta v_{dc}
\tag{8.17}
$$

In order to derive Δv_{dc}, the complex power S has to be calculated.

$$
\begin{aligned}
S = \left\{ \overline{E}\vec{i}^{*} \right\} &= (E_0 + \Delta E_d + j\Delta E_q)[i_{d0} + \Delta i_d - j(i_{q0} + \Delta i_q)] \\
&\approx E_0 i_{d0} + E_0 \Delta i_d + i_{d0}\Delta E_d + i_{q0}\Delta E_q \\
&\quad + j(-E_0 i_{q0} - E_0 \Delta i_q + i_{d0}\Delta E_q - i_{q0}\Delta E_d)
\end{aligned}
\tag{8.18}
$$

The active power and reactive power will then extracted:.

$$
\begin{cases}
P = E_0 i_{d0} + E_0 \Delta i_d + i_{d0}\Delta E_d + i_{q0}\Delta E_q \\
Q = -E_0 i_{q0} - E_0 \Delta i_q + i_{d0}\Delta E_q - i_{q0}\Delta E_d
\end{cases}
\tag{8.19}
$$

Assuming that $P_0 = E_0 i_{d0}$ and $Q_0 = -E_0 i_{q0}$, the small deviation parts of powers are then expressed in (8.20).

$$
\begin{cases}
\Delta P = E_0 \Delta i_d + i_{d0}\Delta E_d + i_{q0}\Delta E_q \\
\Delta Q = -E_0 \Delta i_q + i_{d0}\Delta E_q - i_{q0}\Delta E_d
\end{cases}
\tag{8.20}
$$

Considering the dynamics on dc capacitor C_{dc}, the energy stored in the capacitor is

101

$$W = \frac{1}{2}C_{dc}v_{dc}^2$$
$$\Rightarrow \frac{1}{2}C_{dc}\frac{dv_{dc}^2}{dt} = P_{dc} = P - P_L \tag{8.21}$$
$$\Rightarrow C_{dc}v_{dc}\frac{dv_{dc}}{dt} = P - P_L$$

where P_L is the active power consumed by load. Applying small perturbation leads to (8.22), the linear relationship between dc voltage and active power is obtained.

$$C_{dc}(v_{dc0} + \Delta v_{dc})\frac{d(v_{dc0} + \Delta v_{dc})}{dt} = P_0 + \Delta P - P_{L0} - \Delta P_L$$
$$\Rightarrow C_{dc}v_{dc0}\frac{d\Delta v_{dc}}{dt} = \Delta P - \Delta P_L \tag{8.22}$$

Since the current control loop of both inverter and rectifier station is identical, substituting (8.17) into (8.5) modifies equation (8.20) as:

$$\Delta P = E_0[-g_c(s)F_{dc}(s)\Delta v_{dc} + y_i(s)\Delta E_d]$$
$$+ i_{d0}\Delta E_d + i_{q0}\Delta E_q \tag{8.23}$$

Using (8.22) and (9.18), and assuming $\Delta P_L = 0$, Δv_{dc} is derived in terms of ΔE_d and ΔE_q.

$$sC_{dc}v_{dc0}\Delta v_{dc} = -E_0g_c(s)F_{dc}(s) + E_0y_i(s)\Delta E_{d\_inv}$$
$$+ \frac{P_0}{E_0}\Delta E_d - \frac{Q_0}{E_0}\Delta E_q \tag{8.24}$$
$$\Rightarrow \Delta v_{dc} = \frac{(E_0^2y_i(s) + P_0)\Delta E_d - Q_0\Delta E_q}{sE_0C_{dc}v_{dc0} + E_0^2g_c(s)F_{dc}(s)}$$

Substituting (8.24) into (8.17), Δi_{dref} could be represented in terms of ΔE_d and ΔE_q.

$$\Delta i_{dref} = \underbrace{\frac{-(E_0^2y_i(s) + P_0)F_{dc}(s)}{sE_0C_{dc}v_{dc0} + E_0^2g_c(s)F_{dc}(s)}}_{G_{dc}^d(s)}\Delta E_d$$
$$+ \underbrace{\frac{Q_0F_{dc}(s)}{sE_0C_{dc}v_{dc0} + E_0^2g_c(s)F_{dc}(s)}}_{G_{dc}^q(s)}\Delta E_q \tag{8.25}$$

102

Besides dc-link voltage control, the inverter station could also compensate reactive power to the right-hand side grid, which utilizes the same control structure as that of the rectifier station. Therefore, the input admittance for the inverter station is shown in equation (8.26),

$$Y_{inv}(s) = Y_i(s) + G_{Ei\_inv}(s)G_c(s)$$

$$= \begin{bmatrix} y_i(s) + G_{dc}^d(s)g_c(s) & G_{dc}^q(s)g_c(s) \\ \frac{Q_{ref}}{E_0^2}F_{2nd}(s)g_c(s) & y_i(s) \end{bmatrix} \tag{8.26}$$

where

$$G_{Ei\_inv}(s) = \begin{bmatrix} G_{dc}^d(s) & G_{dc}^q(s) \\ \frac{Q_{ref\_inv}}{E_{0\_inv}^2}F_{2nd}(s) & 0 \end{bmatrix}. \tag{8.27}$$

8.1.2 Stability Analysis
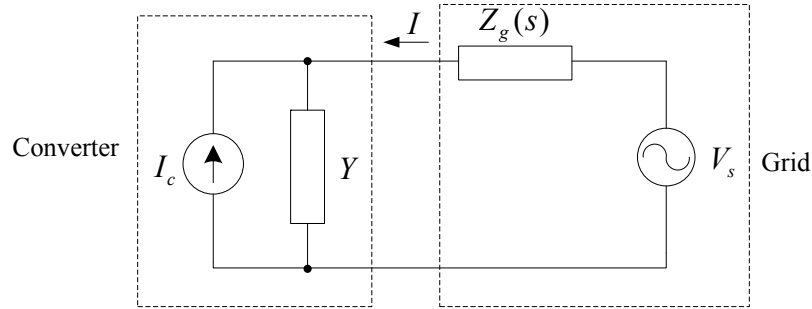
Figure 8.5. Small-signal representation of a converter-grid system.

The grid is modeled as a combination of an ideal ac voltage source v_s and an impedance , which consists of a resistor R_g and an inductor L_g. Under dq frame, the impedance is expressed as $Z_g(s)$ in (8.28).

$$Z_g = \begin{bmatrix} R_g + sL_g & -\omega L_g \\ \omega L_g & R_g + sL_g \end{bmatrix} \tag{8.28}$$

Based on Fig. 8.5, the current I flowing from the grid to the converter is

$$I(s) = \frac{V_g(s) - Y^{-1}(s)I_c(s)}{Z_g(s) + Y^{-1}(s)} \qquad (8.29)$$

which can be rearranged to

$$I(s) = [Y(s)V_g(s) - I_c(s)]\frac{1}{1 + Y(s)Z_g(s)} \qquad (8.30)$$

Therefore, the stability analysis of the system relies on $Y(s)Z_g(s)$ in (8.30). Consequently, the grid-connected converter will operate stably if $Y(s)Z_g(s)$ satisfies Nyquist stability criterion. Since the VSC-HVDC system consists of a rectifier station and an inverter station, and the input admittance of each station depends on not only component parameters but also different control loops, it is obvious that many factors may affect the resonance stability.

8.2   Impacting Factors of Resonance Stability

In this section, we carry out frequency domain analysis based on impedance models and validate the analysis via MATLAB/SimPowerSystems simulation. SimPowerSystems is a toolbox of MATLAB/Simulink developed by Hydro-Québec of Montreal [105]. Models built in SimPowerSystems include switching details and are considered high-fidelity models. [106] compared the simulation results between SimPowerSystems toolbox and PSPICE, and demonstrated that SimPowerSystems is well suitable for the electrical circuits simulation containing switching devices because it can detect precise discontinuities.

In the literature, SimPowerSystems simulation results substituting experimental results are used for validation for VSC-HVDC systems. For example, [107] compared the simulations of CIGRÉ HVDC Benchmark System between SimPowerSystems and PSCAD/EMTDC, which demonstrated that both simulation tools are accurate and consistent during steady-state and transients situations. [108, 109, 110] investigated the various issues of VSC-HVDC using SimPowerSystems toolbox, including subsynchronous resonance, robust sliding-mode Controller, and Small-signal stability analysis.

Therefore, MATLAB/SimPowerSystems simulation is also used as a tool to validate the impedance model based analysis.

8.2.1 Feed-forward Filter

The feed forward filter in the current control loop as shown in (8.3) has impact on the input admittance of rectifier $Y_{rec}(s)$ and hence can influence resonance stability. E_d and E_q are the feed forward PCC voltages in dq frame after the filter. In this subsection, the impact on stability of a second-order filter is compared with a first order filter. The transfer function of a first order low pass filter is as follows:

$$F_{1st}(s) = \frac{1}{s\tau + 1}. \tag{8.31}$$

where τ is the time constant (0.001 s). Two scenarios with same power transfer level (100 MW) and same inverter control structures are examined:

- The feed-forward filter at the rectifier is a 1st order filter

- The feed-forward filter at the rectifier is a 2nd order filter

The line inductance L_g is chosen to be 0.05 H.

Figs. 8.6 and 8.7 present the real part of the total impedances for the rectifier side ac system and the inverter side ac system. Analysis of complex torque coefficients method in [111] indicated that the resonance frequencies are related to the roots of the real part of a transfer function. A brief explanation is offered as follows.

Assuming there are only oscillatory modes in the system, then $Z_g(s) + Z_{conv}(s)$ $(Z_{conv} = Y^{-1})$ should only have roots appearing as complex conjugate pairs $(-\sigma_l \pm \omega_l)$. $Z_g(s)$ and $Z_{conv}(s)$ are rational functions. Therefore

$$Z_g(s) + Z_{conv}(s) = \frac{P(s)}{Q(s)} \tag{8.32}$$

105

where $P(s)$ and $Q(s)$ are polynomials of s

$$P(j\omega) = \gamma \prod_{l}^{n} (j\omega + \sigma_l + j\omega_l)(j\omega + \sigma_l - j\omega_l)$$
$$= \gamma \prod_{l}^{n} (\sigma_l^2 + \omega_l^2 - \omega^2 + 2j\sigma_l\omega) \tag{8.33}$$

where γ is a constant.

Assuming negligible damping terms, then $P(j\omega)$ is a real function and denoted as $P_R(\omega)$. Hence

$$Re(Z_g(j\omega) + Z_{conv}(j\omega)) = \alpha(\omega)P_R(\omega) \tag{8.34}$$

where $\alpha(\omega)$ is also a real function.

When $s = j\omega_l$, $P_R(\omega_l) \approx 0$, and hence $Re(Z_g(s) + Z_{conv}(s)) \approx 0$. From the roots of the real part of the total impedances, resonance frequencies can be identified. For example, from Fig. 8.6, the resonance frequencies are 70 Hz and 190 Hz when 1st order filter or 2nd order filter is employed.
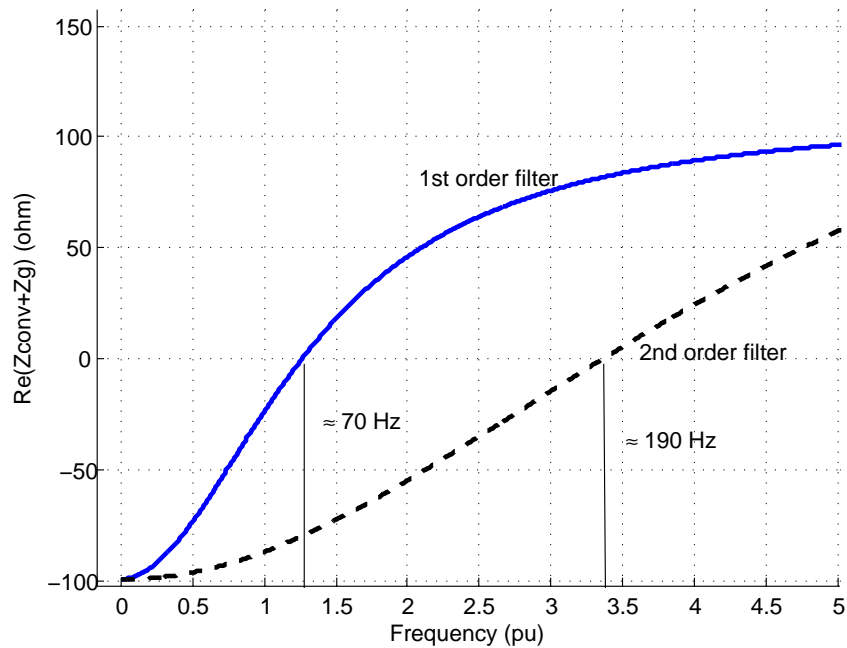

Figure 8.6. Real part of the total impedance (left-hand side grid impedance plus converter impedance) at rectifier side.

106
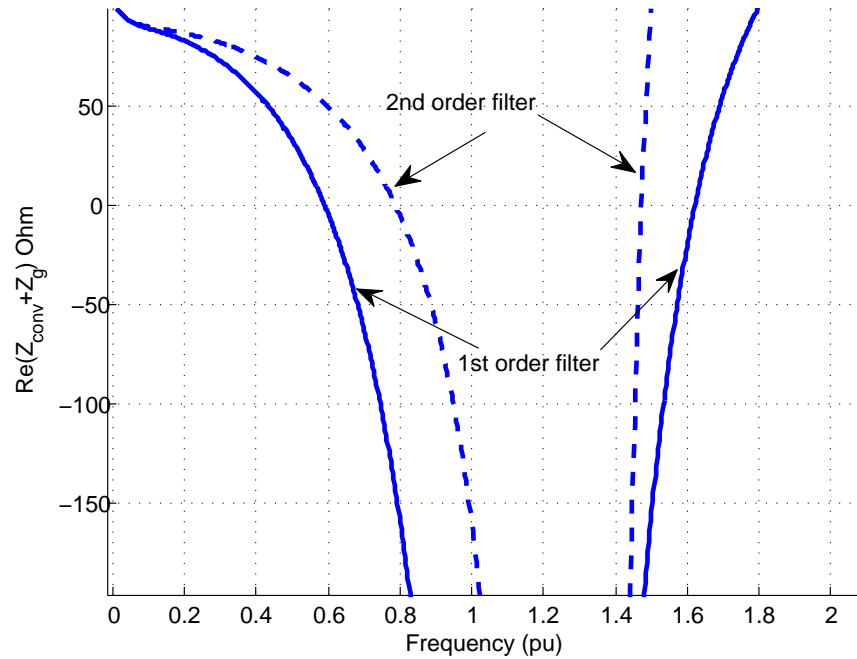
Figure 8.7. Real part of the total impedance (right-hand side grid impedance plus converter impedance) at inverter side.

A detailed VSC-HVDC model is built in MATLAB SimPowerSystems to verify the analysis. The parameters of the system are listed in Table 8.3. The HVDC system is operated at 100 MW power transfer level. Fig. 8.8 shows the rectifier side d-axis current with two types of filters, where the oscillation frequency in the case of first-order filter is much lower than that when the 2nd -order filter case. Fig. 8.10 shows the active power at the rectifier side with two types of filter. Figs. 8.11 and 8.13 present the d-axis current and active power at the inverter side. Fig. 8.9 and Fig. 8.12 shows the d axis PCC voltage at rectifier and inverter stations with different filters. The d-axis PCC voltage with first order filter is lower than the d-axis PCC voltage with second order filter. Since the rectifier station operates on power control mode, which causes the d-axis current with first order filter case higher than the current with second order filter. The inverter station delivers active power transferred from rectifier station to right-hand side grid, therefore, the d-axis current with first order filter case is also higher than the second order filter case.

107

Figure 8.8. Rectifier side d-axis current with different filters.
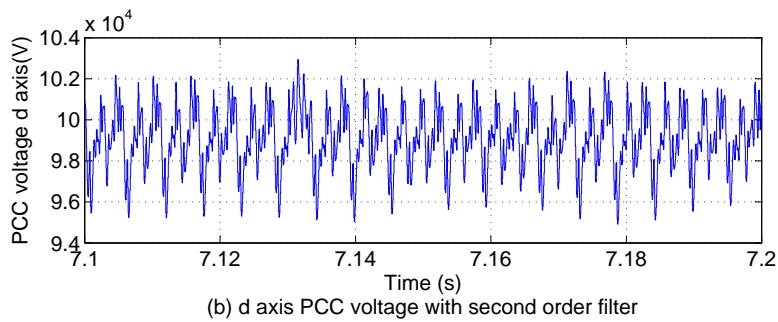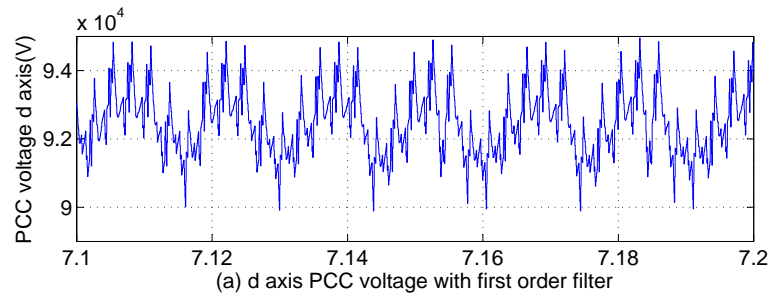
Figure 8.9. Rectifier side d-axis PCC voltage with different filters.

108
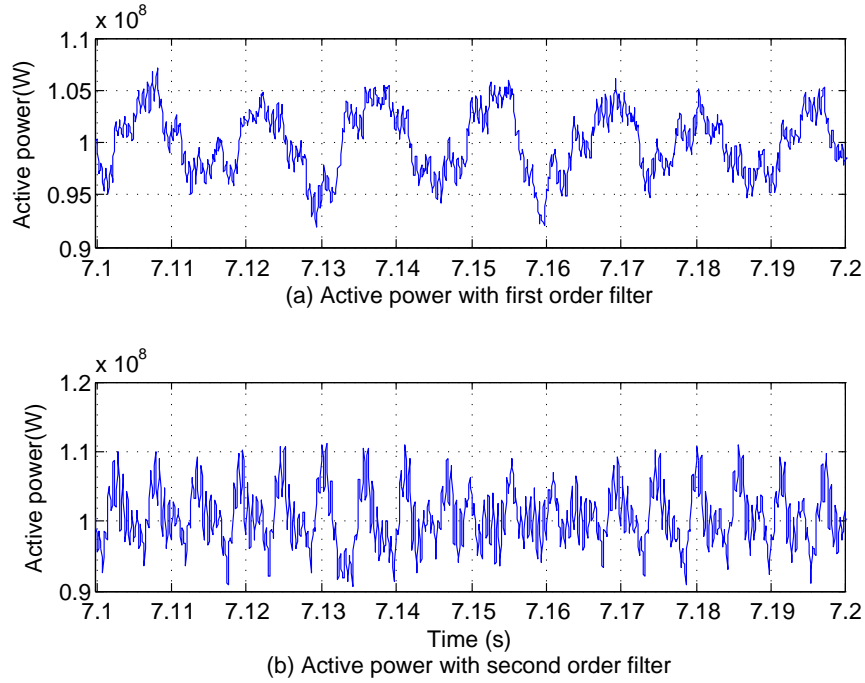
Figure 8.10. Rectifier side active power with different filters.

Figs. 8.8 and 8.10 show that the rectifier side ac system possesses a resonance around 70 Hz with 1st order filter and 190 Hz with 2nd order filter. This observation corroborates with the analysis in total impedance frequency responses in Fig. 8.6.

The inverter side ac system possesses at least two resonance frequencies as shown in Fig. 8.7 where two roots are identified. Simulation results also demonstrate more complicated waveforms in d-axis current and active power. The rectifier side ac line inductance is 0.02H while the inverter side line inductance is 0.012H. The resonances cause around 5% ripples in waveforms and do not pose stability issues.

8.2.2   ac Line Length

The impact of the line length of the rectifier ac side on resonance is studied in this subsection. The inductance of the rectifier ac system is varied to reflect the change of length. First-order feed forward filter is adopted in the current controller of the VSC. The power transfer level is set to 100 MW. The Nyquist curves for the eigenvalues of YZ_g are presented in Fig. 8.14.
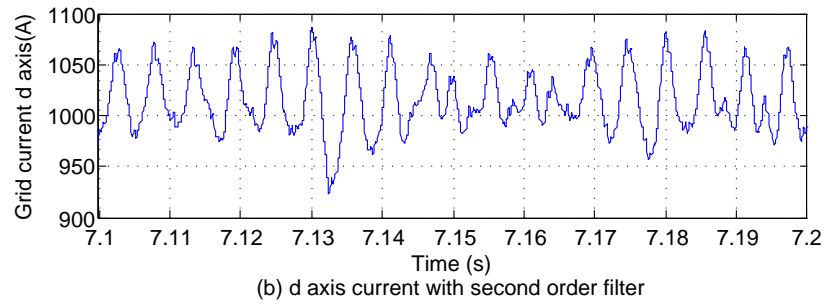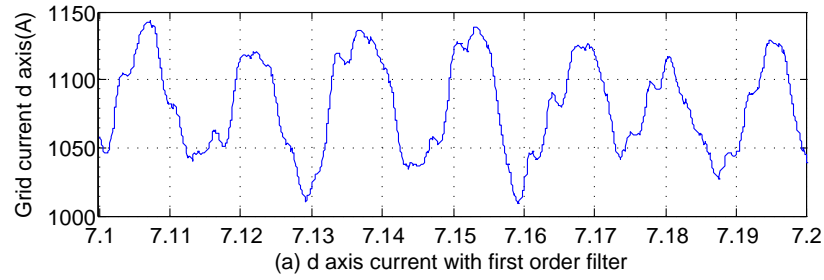
109
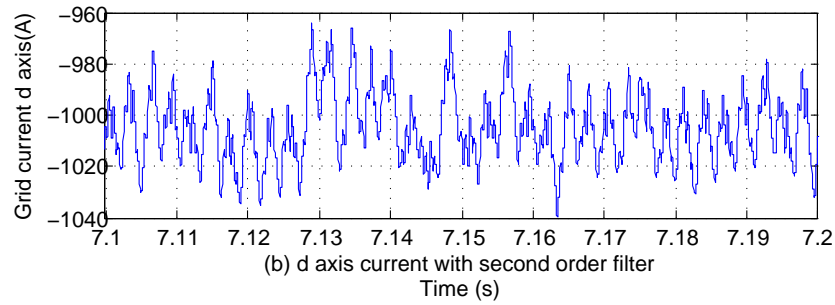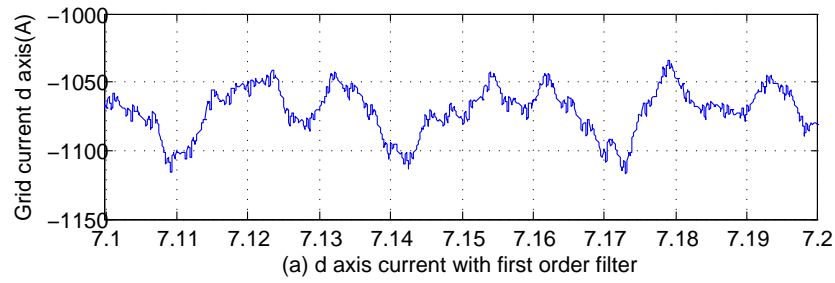
Figure 8.11. Inverter side d-axis current with different filters.
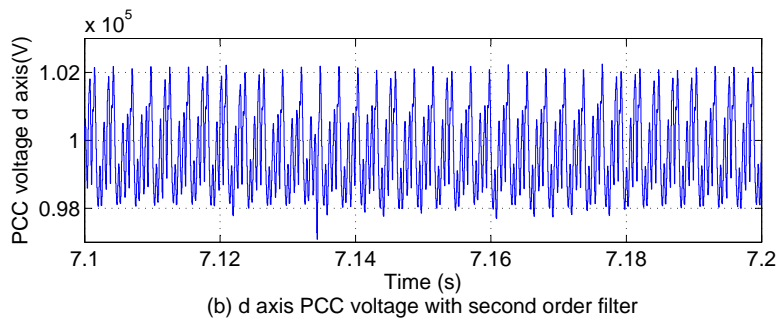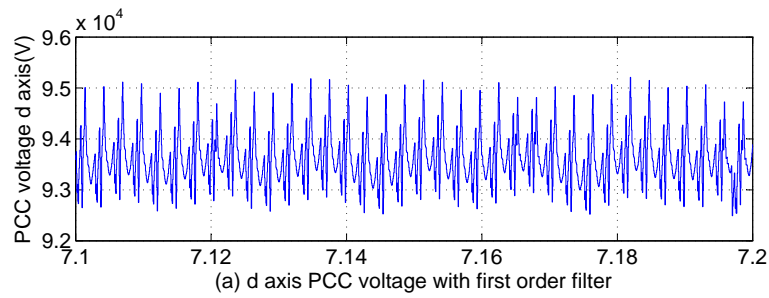
Figure 8.12. Inverter side d-axis PCC voltage with different filters.

110
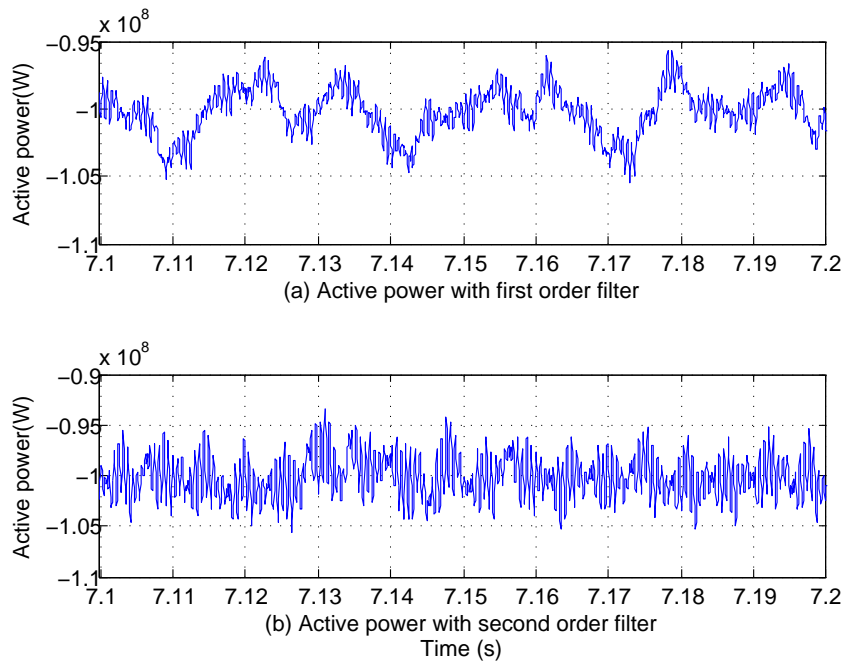
Figure 8.13. Inverter side power with different filters.
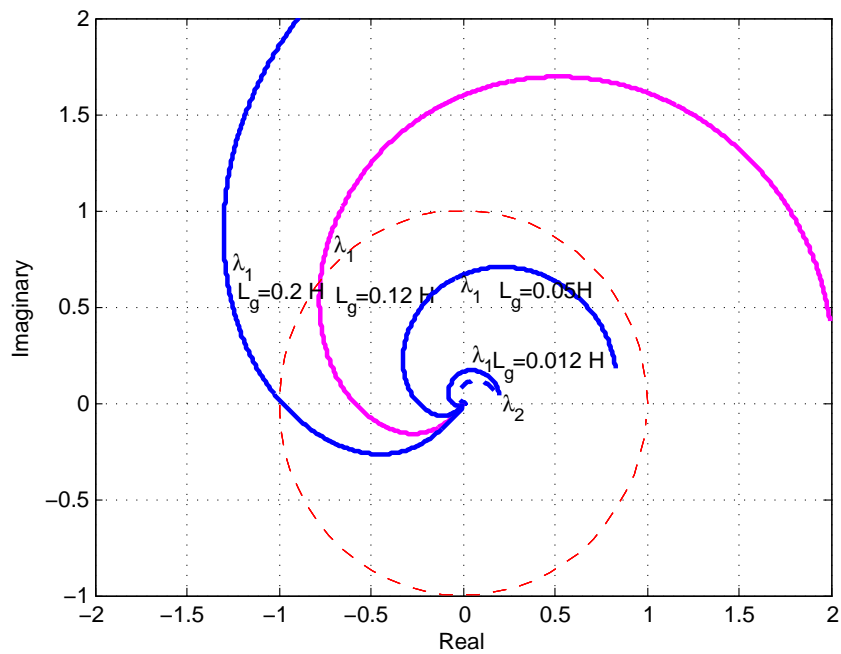
Figure 8.14. Nyquist curves for the eigenvalues of YZ_g (rectifier ac system) for various line inductance.

111
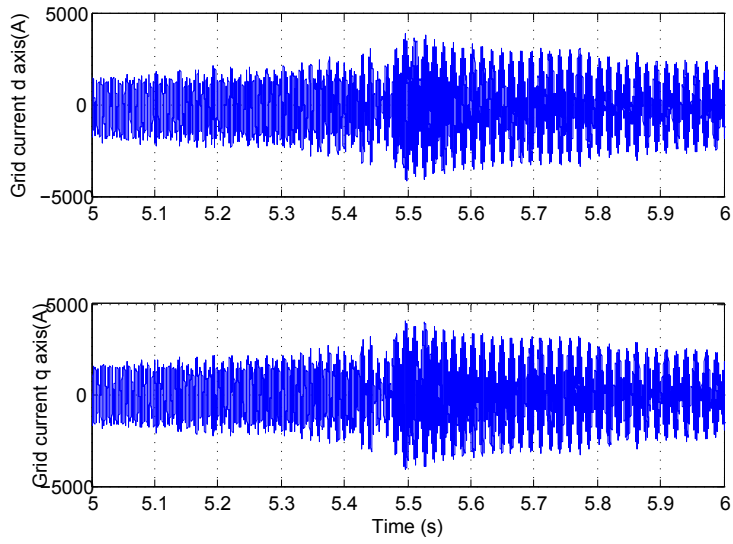
Figure 8.15. Simulation results of i_d and i_q. $L_g = 0.05H$.
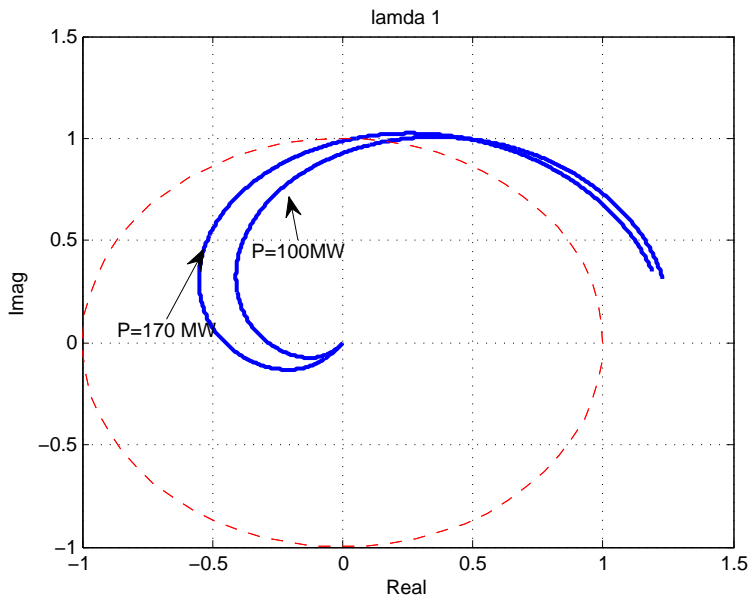
Figure 8.16. Nyquist curves for the eigenvalues of YZ_g (rectifier ac system) for two power levels.

112
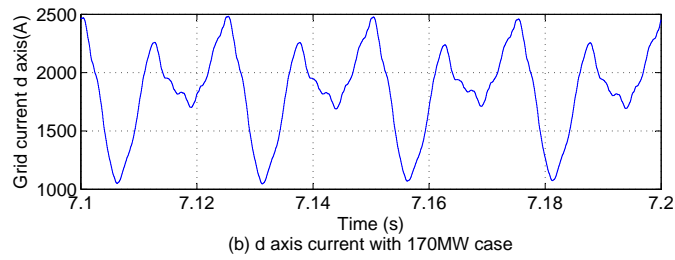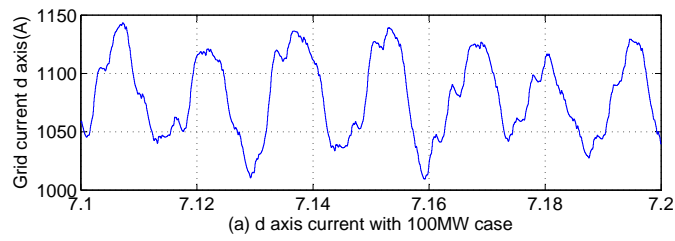
Figure 8.17. *d*-axis current with different power level.
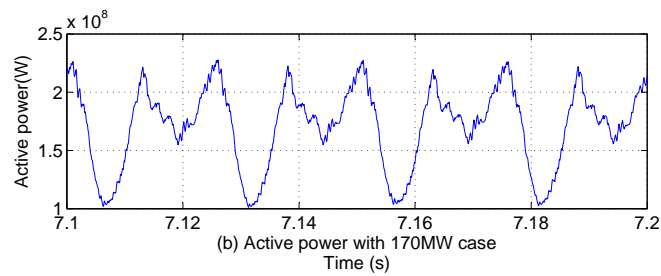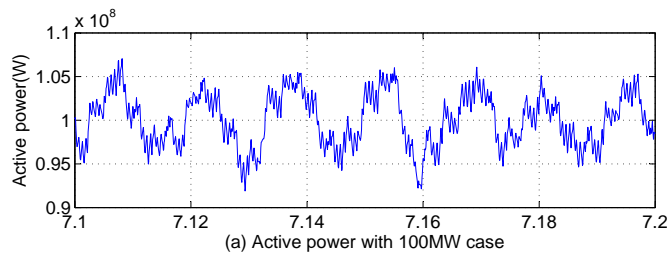
Figure 8.18. Active power with different power level.

113

The Nyquist curves shows that with the increase of line length, the more the system is prone to instability. Take the example of $L_g = 0.12H$, the time domain simulation results of the rectifier ac grid currents in dq-axis are shown in Fig. 8.15. It is clearly that the system has lost stability.

8.2.3 Power Level

Power transfer level is indicated in [63] to impact the converter impedance. Hence in this subsection, the impact of power level is investigated. Fig. 8.16 gives the Nyquist curves for one of the eigenvalues of YZ_g (rectifier ac system) for two power levels (100 MW and 170 MW). The line inductance is chosen to be 0.05 H. It is found from Nyquist curves that the higher the power transfer level, the more the system is prone to resonance.

The d-axis currents at the two power levels are shown in Fig. 8.17 and the active powers in the rectifier ac system at the two power levels are shown in Fig. 8.18. It can be observed that at 100 MW level, the ripple magnitude in i_d is about 5% of the mean magnitude, while it is more than 30% at 170 MW level.

CHAPTER 9

DC IMPEDANCE-MODEL-BASED RESONANCE ANALYSIS OF A VSC-HVDC SYSTEM

The harmonic resonances in VSC interfaced ac grids have been examined in [98, 99, 101, 100, 63]. In addition, subsynchronous resonances due to the interaction of a VSC and a series compensated ac network are examined in [112, 113]. A comprehensive examination of both the ac systems (the rectifier side and the inverter side) of a VSC-HVDC system has been described in Chapter 8. Impedance models for the two ac systems were derived and used for resonance analysis. However, a comprehensive dc impedance based analysis on the dc system while taking both rectifier and inverter station into account has not been seen in the literature. This chapter will address this topic. The VSC-HVDC system has various different converter topology choices to be implemented. Among those topologies, two-level converter, three-level converter and Modular Multilevel converter (MMC) are three topologies with most of interest. Regarding the current harmonics spectrums on ac side within those topologies, the most significant harmonic would be around the switching frequency which is normally around 1.6kHz for two-level converters, and the frequency will be increased to doubled switching frequency for three-level converters. The current waveforms have significant improvements for MMC topology, and the most significant harmonic is always higher than two-level and three-level converters, and would depend on the number of converter modules in each leg. However, the resonance frequencies discovered by [104] are at low range, such as below 200Hz, which is far away from the switching frequencies and imply that the topology has limited impacts on ac side resonance. The dc impedance modeling depends on the topology of dc side much, which makes non-negligible differences among those topologies. For a three-level converter topology, the dc side is similar with two-level converters. However, the neutral point voltage clamp structure brings additional unique inherent voltage variations comparing to two-level converters.

The neutral point voltage varies at three times of the fundamental frequency [114], which imposes additional harmonics on dc side. Instead of a single or two capacitors, the MMC topology consists of a large number of submodules, and each module has a capacitor, which makes the equivalent dc capacitor is a series connection of various capacitors [115]. Furthermore, the series number is not a constant and depends on the switching state of each submodule. That characteristic would impose high frequency voltage oscillations on dc side and requires additional investigation to be implemented. This chapter will then focus on the two-level converter topology which has a single capacitor on dc side.

Most of the dc side impedance modeling for converters are focused on single converter and machine drive applications [116, 117, 118]. In addition, few papers have presented dc impedance models with the effect of converter controls included. For example, Sudhoff *et al* in [116] discussed dc impedance model for a dc/ac converter. The converter is assumed to be a constant power load and the incremental impedance is a negative resistance. In a most recent paper [118], a dc input admittance model is developed for a dc/ac converter interfaced permanent-magnet synchronous motor (PMSM). PMSM dynamics are included in the model. However, the converter controller dynamics are neglected.

For a VSC-HVDC system, at least two converter stations exist and the control mechanism for each station is different, which implies the dc impedance modeling may have different characteristics for each station. Therefore, a comprehensive analysis of dc impedance modeling of a VSC-HVDC system is required to better understand the dc resonance issues. In this chapter, dc resonance issues will be investigated for a two-terminal VSC-HVDC system. Typical VSC-HVDC controls and a practical dc transmission line will be adopted. Frequency domain analysis will be applied to examine the characteristics of the derived dc impedance models. The models will be verified by comparing with the frequency responses obtained from a detailed VSC-HVDC system simulated in a real-time digital simulator. Real-time digital simulations will also be used to validate the dc resonance analysis on the impact of dc capacitor and power transfer levels.

116

9.1 Analysis

9.1.1 System Model

A two-terminal VSC-HVDC transmission system is shown in Fig. 8.1. The basic controllers for both rectifier and inverter stations are depicted in Fig. 8.1. Since the structure of both stations are identical, each station could operate on either rectifier or inverter mode depending on the requirement of system operator. Normally, the rectifier station controls the amount of active power transfer, and the inverter station controls dc-link voltage in order to keep power transfer balance. Both stations are able to compensate reactive power to ac grid by directly injecting reactive power or control the ac grid voltage.

Table 9.1. System parameters of VSC-HVDC model

Quantity	Value
ac system line voltage	100kV
ac system frequency	60Hz
Grid impedance	0.01Ω/1.88mH
Grid filter capacity	18Mvar
Grid filter tuning frequency	1620Hz
dc rated voltage	250kV
dc cable parameters	0.0139Ω/km, 0.159mH/km, 0.231μF/km
dc cable length	50km

An equivalent model of a VSC connecting with an ac voltage source via an inductor is shown in Fig. 9.1. The ac voltage source is represented by an ideal voltage source v_s in series with an impedance $Z(s)$. The PCC voltage is then represented by E. After the coupling inductor L, the equivalent output voltage of the VSC is called v. At the dc side of VSC, the dc-link voltage and current are represented by v_{dc} and i_{dc}. The capacitor C_{dc} is used to stabilize the dc voltage, while i_{dc1} is the net current flowing to the other station. (9.1) describes the voltage and current relationship between grid and converter in dq frame. The letter with upper-line represents complex space vector, such as $\bar{v} = v_d + jv_q$ and $\bar{i} = i_d + ji_q$. The angular speed within grid reference frame is ω, which is a constant throughout this chapter.

117
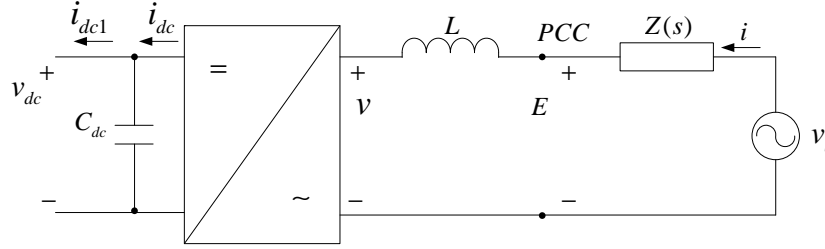
Figure 9.1. A model of VSC and grid.

Table 9.2. Parameters of individual VSC

Quantity	Value
Switching frequency	1620Hz
Grid filter	$0.01\Omega/0.02$H
Grid impedance	$0.01\Omega/1.88$mH
dc capacitor	900μF

$$L\frac{d\bar{i}}{dt} + j\omega L\bar{i} = \overline{E} - \overline{v} \tag{9.1}$$

9.1.2 Impedance Model

9.1.2.1 Rectifier Station

This chapter investigates the dc impedance model of a VSC-HVDC system, which focuses on the dc side analysis. In order to derive the dc impedance model, the ratio of small variation of dc voltage and dc current has to be implemented.

The dc power analysis will be performed in order to derive impedance model. The objective of dc impedance derivation is to find out the expression of $\frac{\Delta v_{dc}}{\Delta i_{dc}}$. In order to relate v_{dc} and i_{dc} to ac quantities, one solution is the power relationship. Since the controller of VSC-HVDC utilizes dq decoupling control algorithm, the abc three-phase voltage and current quantities v_{abc} and i_{abc} are then converted into dq frame as v_{dq} and i_{dq} by Park transformation. The three-phase instantaneous power can then be expressed by dq quantities as $v_a i_a + v_b i_b + v_c i_c = v_d i_d + v_q i_q$. When neglecting the power loss on IGBTs switches, the power on ac side is equal to the power on dc side $v_{dc} i_{dc}$, which yields equation (9.2). Taking the small signal analysis on (9.2) and rearranging the equation

118

can lead to the relation between Δv_{dc} and Δi_{dc}, which is shown in (9.3). In (9.3), the variables v_{dq} and i_{dq} are ac side quantities, which implies the derivation should involve both dc and ac side. Hence, in order to get an expression of the dc impedance ($\frac{\Delta v_{dc}}{\Delta i_{dc}}$), the ac side variables (Δv_{dq} and Δi_{dq}) have to be expressed in terms of Δv_{dc} and Δi_{dc}.

$$v_{dc}i_{dc} = v_d i_d + v_q i_q \tag{9.2}$$

$$\Delta v_{dc}i_{dc0} = -v_{dc0}\Delta i_{dc} + \begin{bmatrix} i_{d0} & i_{q0} \end{bmatrix} \begin{bmatrix} \Delta v_d \\ \Delta v_q \end{bmatrix}$$
$$+ \begin{bmatrix} v_{d0} & v_{q0} \end{bmatrix} \begin{bmatrix} \Delta i_d \\ \Delta i_q \end{bmatrix} \tag{9.3}$$

The controller consists of current control and power control. The current control analysis will be implemented as follows. The rectifier station controls the amount of active power transferred to inverter station, and can also compensate reactive power to grid to support the ac voltage. The control system of rectifier stations is shown in Fig. 9.2, where P is the measured active power sent to inverter station. There are two control loops in Fig. 9.2, the outer loop is power control loop which controls the active power transfer and grid ac voltage. The outer control loop generates the reference of dq currents. The inner control loop regulates the dq axis currents and tries to track the respective reference value which is obtained from outer control loop. The analysis of current control is identical to the ac impedance modeling which in shown in [104] and the details will be skipped. The current i can be expressed as (9.4),
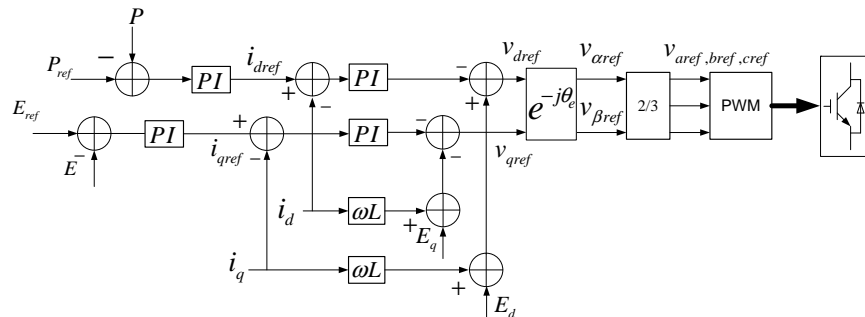
Figure 9.2. Controller of the rectifier station.

119

$$i = \underbrace{\begin{bmatrix} g_c(s) & 0 \\ 0 & g_c(s) \end{bmatrix}}_{G_c(s)} i_{ref} + \underbrace{\begin{bmatrix} y_i(s) & 0 \\ 0 & y_i(s) \end{bmatrix}}_{Y_i(s)} E \tag{9.4}$$

where i, i_{ref} and E are vectors of d-axis and q-axis variables.

$$\begin{cases} g_c(s) = \frac{k_p s + k_i}{L s^2 + k_p s + k_i} \\ y_i(s) = \frac{s^2(s + 2\xi\omega_0)}{(L s^2 + k_p s + k_i)(s^2 + 2\xi\omega_0 s + \omega_0^2)} \end{cases} \tag{9.5}$$

The parameters in (9.5) can be found in the current PI controller $F_c(s) = k_p + \frac{k_i}{s}$ and the second-order filter $F_{2nd}(s) = \frac{\omega_0^2}{s^2 + 2\xi\omega_0 s + \omega_0^2}$, which is used to feed forward the measured PCC voltage E_d and E_q. The cut-off frequency ω_0 is chosen at 1000 Hz and damping factor ξ is $\frac{1}{\sqrt{2}}$.

From Fig. 9.1, v_s is the grid voltage, which is always treated as a constant. However, the PCC voltage E can be affected by the source impedance Z and current i. Therefore, the impact of source impedance Z has to be taken into account. The source voltage can be expressed as (9.6), which can be linearized as (9.7).

$$v_s = E + Zi \tag{9.6}$$

$$\Delta v_s = \Delta E + Z\Delta i \tag{9.7}$$

Combining (9.6) and (9.4) yields (9.8), which can also be linearized as (9.9).

$$i = \frac{1}{1 + Y_i(s)Z(s)}[G_c(s)i_{ref} + Y_i(s)v_s] \tag{9.8}$$

$$\Delta i = [I + Y_i(s)Z(s)]^{-1}[G_c(s)\Delta i_{ref} + Y_i(s)\Delta v_s] \tag{9.9}$$

(9.9) gives the expression of ac current in terms of source voltage and current reference.

The power control analysis is performed as follows. The power conversion efficiency of IGBTs within a two-level VSC-HVDC system is around 98%, and the efficiency increases to 99.5% for

120

a MMC topology [119]. Hence, the active power loss on the IGBTs within rectifier station can be neglected, and the measured active power can also be expressed as $P = v_{dc}i_{dc}$. However, the damping in the system would be lower than the real system during analysis because of the neglecting of power loss. From Fig. 9.2, the reference of d axis current can be expressed as (9.10), where $F_p(s) = k_{p\_p} + \frac{k_{i\_p}}{s}$ is a PI controller.

$$i_{d\_ref} = (P_{ref} - v_{dc}i_{dc})F_p(s) \qquad (9.10)$$

Linearizing (9.10) yields (9.11).

$$\Delta i_{d\_ref} = \begin{bmatrix} -i_{dc0}F_p(s) & -v_{dc0}F_p(s) \end{bmatrix} \begin{bmatrix} \Delta v_{dc} \\ \Delta i_{dc} \end{bmatrix} \qquad (9.11)$$

The reference of q axis current can be expressed as (9.12), where $F_{ac}(s) = k_{p\_ac} + \frac{k_{i\_ac}}{s}$ is the ac voltage PI controller.

$$i_{q\_ref} = (E_{d\_ref} - E_d)F_{ac}(s) \qquad (9.12)$$

Linearizing (9.12) yields (9.13).

$$\begin{aligned} \Delta i_{q\_ref} &= -\Delta E_d F_{ac}(s) \\ &= \begin{bmatrix} -2sLF_{ac}(s) + \frac{E_{d0}F_{ac}(s)}{i_{d0}} \\ -2sL\frac{i_{q0}F_{ac}(s)}{i_{d0}} \end{bmatrix}^T \begin{bmatrix} \Delta i_d \\ \Delta i_q \end{bmatrix} \\ &+ \begin{bmatrix} -\frac{i_{dc0}F_{ac}(s)}{i_{d0}} \\ -\frac{v_{dc0}F_{ac}(s)}{i_{d0}} \end{bmatrix}^T \begin{bmatrix} \Delta v_{dc} \\ \Delta i_{dc} \end{bmatrix} \end{aligned} \qquad (9.13)$$

Combining (9.11) and (9.13) yields the expression of Δi_{d_ref} and Δi_{q_ref}, which is (9.14).

$$\begin{bmatrix} \Delta i_{d\_ref} \\ \Delta i_{q\_ref} \end{bmatrix} = G_{p1} \begin{bmatrix} \Delta i_d \\ \Delta i_q \end{bmatrix} + G_{p2} \begin{bmatrix} \Delta v_{dc} \\ \Delta i_{dc} \end{bmatrix} \qquad (9.14)$$

121

$$G_{p1} = \begin{bmatrix} 0 & 0 \\ -2sLF_{ac}(s) + \frac{E_{d0}F_{ac}(s)}{i_{d0}} & -2sL\frac{i_{q0}F_{ac}(s)}{i_{d0}} \end{bmatrix} \tag{9.15}$$

$$G_{p2} = \begin{bmatrix} -i_{dc0}F_p(s) & -v_{dc0}F_p(s) \\ -\frac{i_{dc0}F_{ac}(s)}{i_{d0}} & -\frac{v_{dc0}F_{ac}(s)}{i_{d0}} \end{bmatrix} \tag{9.16}$$

At steady state, the PCC voltage in dq frame is $E_{dq} = v_{dq} + Z_L(s)i_{dq}$, in which $Z_L(s)$ is the coupling inductor represented in dq frame. Hence, rewriting (9.2) can obtain the relation between dc quantities and PCC voltage and dq currents, which is shown in (9.17). The small signal representation of which is then expressed as (9.18). The Phase Locked Loop (PLL) in the controller tracks the phase of phase A voltage at PCC. The phase information is then applied for $abc - dq$ transformation. Hence, the output of PLL would be stable without disturbance if the PCC voltages are three-phase balanced sinusoidal voltages and the response speed of PLL is tuned fast. Throughout this chapter, the PCC voltages are always balanced and therefore the impacts of PLL can be neglected. Hence, we can assume the q axis component of PCC voltage is always 0, which implies $\Delta E_q = 0$. Therefore, (9.18) can be rearranged, and we can get ΔE_d in terms of i_{dq}, v_{dc} and i_{dc}, which is shown in (9.19).

$$\begin{aligned} v_{dc}i_{dc} &= \begin{bmatrix} v_d & v_q \end{bmatrix} \begin{bmatrix} i_d \\ i_q \end{bmatrix} = \begin{bmatrix} v_d \\ v_q \end{bmatrix}^T \begin{bmatrix} i_d \\ i_q \end{bmatrix} \\ &= (\begin{bmatrix} E_d \\ E_q \end{bmatrix} - Z_L(s)\begin{bmatrix} i_d \\ i_q \end{bmatrix})^T \begin{bmatrix} i_d \\ i_q \end{bmatrix} \\ &= (\begin{bmatrix} E_d \\ E_q \end{bmatrix} - \begin{bmatrix} sL & -\omega L \\ \omega L & sL \end{bmatrix}\begin{bmatrix} i_d \\ i_q \end{bmatrix})^T \begin{bmatrix} i_d \\ i_q \end{bmatrix} \\ &= \begin{bmatrix} E_d - sLi_d + \omega Li_q \\ E_q - sLi_q - \omega Li_d \end{bmatrix}^T \begin{bmatrix} i_d \\ i_q \end{bmatrix} \\ &= E_di_d + E_qi_q - sLi_d^2 - sLi_q^2 \end{aligned} \tag{9.17}$$

122

$$\Delta v_{dc} i_{dc0} + v_{dc0} \Delta i_{dc} = \Delta E_d i_{d0} + E_{d0} \Delta i_d + \Delta E_q i_{q0}$$
$$+ E_{q0} \Delta i_q - 2sL i_{d0} \Delta i_d - 2sL i_{q0} \Delta i_q \tag{9.18}$$

$$\Delta E_d = \begin{bmatrix} 2sL - \frac{E_{d0}}{i_{d0}} \\ 2sL\frac{i_{q0}}{i_{d0}} - \frac{E_{q0}}{i_{d0}} \end{bmatrix}^T \begin{bmatrix} \Delta i_d \\ \Delta i_q \end{bmatrix} + \begin{bmatrix} \frac{i_{dc0}}{i_{d0}} \\ \frac{v_{dc0}}{i_{d0}} \end{bmatrix}^T \begin{bmatrix} \Delta v_{dc} \\ \Delta i_{dc} \end{bmatrix} \tag{9.19}$$

Rewriting (9.7) into dq reference frame and combining with (9.19) yields (9.20), in which r_g and L_g are the source resistance and inductance respectively.

$$\begin{bmatrix} \Delta v_{sd} \\ \Delta v_{sq} \end{bmatrix} = \begin{bmatrix} \Delta E_d \\ \Delta E_q \end{bmatrix} + \begin{bmatrix} r_g + sL_g & -\omega L_g \\ \omega L_g & r_g + sL_g \end{bmatrix} \begin{bmatrix} \Delta i_d \\ \Delta i_q \end{bmatrix}$$
$$= \underbrace{\begin{bmatrix} 2sL - \frac{E_{d0}}{i_{d0}} + r_g + sL_g & 2sL\frac{i_{q0}}{i_{d0}} - \omega L_g \\ \omega L_g & r_g + sL_g \end{bmatrix}}_{G_{v1}} \begin{bmatrix} \Delta i_d \\ \Delta i_q \end{bmatrix}$$
$$+ \underbrace{\begin{bmatrix} \frac{i_{dc0}}{i_{d0}} & \frac{v_{dc0}}{i_{d0}} \\ 0 & 0 \end{bmatrix}}_{G_{v2}} \begin{bmatrix} \Delta v_{dc} \\ \Delta i_{dc} \end{bmatrix} \tag{9.20}$$

Now, Δi_{ref} and Δv_s are both expressed in terms of Δi_{dq}, Δv_{dc} and Δi_{dc}. Therefore, combining (9.9), (9.14) and (9.20) yields (9.21),

$$\begin{bmatrix} \Delta i_d \\ \Delta i_q \end{bmatrix} = M_{i\_dc} \begin{bmatrix} \Delta v_{dc} \\ \Delta i_{dc} \end{bmatrix} \tag{9.21}$$

where

$$M_{i\_dc} = \left\{ I - [I + Y_i(s)Z(s)]^{-1}(G_c(s)G_{p1} + Y_i(s)G_{v1}) \right\}^{-1}$$
$$[I + Y_i(s)Z(s)]^{-1}(G_c(s)G_{p2} + Y_i(s)G_{v2}) \tag{9.22}$$

The equivalent output voltage of rectifier v_{dq} in dq reference frame is depicted in (9.23).

$$\begin{bmatrix} v_d \\ v_q \end{bmatrix} = \begin{bmatrix} E_d - sLi_d + \omega Li_q \\ E_q - sLi_q - \omega Li_d \end{bmatrix} \tag{9.23}$$

Taking linearization leads to (9.24).

$$\begin{aligned} \begin{bmatrix} \Delta v_d \\ \Delta v_q \end{bmatrix} &= \begin{bmatrix} \Delta E_d - sL\Delta i_d + \omega L\Delta i_q \\ \Delta E_q - sL\Delta i_q - \omega L\Delta i_d \end{bmatrix} \\ &= \begin{bmatrix} \Delta E_d \\ \Delta E_q \end{bmatrix} + \begin{bmatrix} -sL & \omega L \\ -\omega L & -sL \end{bmatrix} \begin{bmatrix} \Delta i_d \\ \Delta i_q \end{bmatrix} \\ &= M_{v\_dc} \begin{bmatrix} \Delta v_{dc} \\ \Delta i_{dc} \end{bmatrix} \end{aligned} \tag{9.24}$$

where

$$M_{v\_dc} = \begin{bmatrix} sL - \frac{E_{d0}}{i_{d0}} & 2sL\frac{i_{q0}}{i_{d0}} + \omega L \\ -\omega L & -sL \end{bmatrix} M_{i\_dc} \\ + \begin{bmatrix} \frac{i_{dc0}}{i_{d0}} & \frac{v_{dc0}}{i_{d0}} \\ 0 & 0 \end{bmatrix} \tag{9.25}$$

Taking (9.21) and (9.24) back into (9.3), the following (9.26) can be obtained.

$$\begin{aligned} \Delta v_{dc} i_{dc0} &= -v_{dc0}\Delta i_{dc} + \begin{bmatrix} i_{d0} & i_{q0} \end{bmatrix} M_{v\_dc} \begin{bmatrix} \Delta v_{dc} \\ \Delta i_{dc} \end{bmatrix} \\ &+ \begin{bmatrix} v_{d0} & v_{q0} \end{bmatrix} M_{i\_dc} \begin{bmatrix} \Delta v_{dc} \\ \Delta i_{dc} \end{bmatrix} \end{aligned} \tag{9.26}$$

Rewriting (9.26) yields the expression of i_{dc0},

124

$$i_{dc0} = -v_{dc0}\frac{\Delta i_{dc}}{\Delta v_{dc}}$$

$$+ \underbrace{\left(\begin{bmatrix} i_{d0} & i_{q0} \end{bmatrix} M_{v\_dc} + \begin{bmatrix} v_{d0} & v_{q0} \end{bmatrix} M_{i\_dc}\right)}_{M} \begin{bmatrix} 1 \\ \frac{\Delta i_{dc}}{\Delta v_{dc}} \end{bmatrix} \tag{9.27}$$

The dc impedance model of rectifier station is then expressed as (9.28)

$$Z_{dc} = \frac{\Delta v_{dc}}{\Delta i_{dc}} = \frac{M(1,2) - v_{dc0}}{i_{dc0} - M(1,1)} \tag{9.28}$$

It can be remarked that although the expression of dc impedance model (9.28) involves grid impedance parameters, the impact of which can be neglected even varying its values. Fig. 9.3 shows the bode plots of dc impedance model of rectifier station with two different grid impedances. The blue trace is the bode plot with grid impedance of 18.8mH, and the green trace is the bode plot with grid impedance of 1.88mH. Other system parameters can be found in Tables 9.1, 9.2, and 9.2. The detailed bode plot in Fig. 9.4 demonstrates the impacts of grid impedances on dc impedance model is very limited. It implies that the ac side parameters have little impact on dc side and the converters isolate ac/dc systems.

9.1.2.2   Inverter Station

The inverter station controls dc-link voltage and ensures power transfer balance. Fig. 9.5 shows the controller of inverter station, in which a dual loop control strategy is also adopted as rectifier station. The only difference between rectifier station is the generation of d axis current reference. The dc-link voltage is measured and feed back to the controller, and the error between its corresponding reference is sent to a PI controller to generate the d axis current reference.

Table 9.3. Parameters of controllers

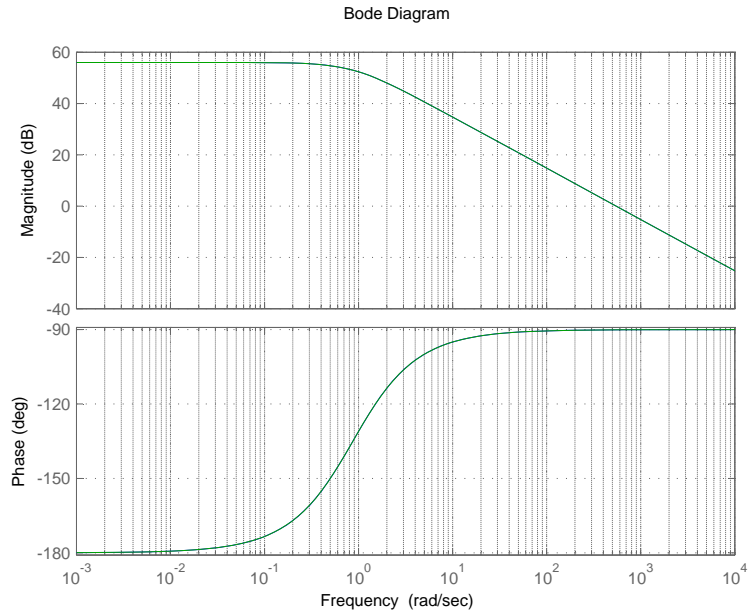| Quantity	Value
Current controller	k_p=50, k_i=100
dc-link voltage controller	k_p=0.04, k_i=0.2
ac voltage controller	k_p=0.01, k_i=100

125

Figure 9.3. Bode plots of dc impedance model of rectifier station with different $Z(s)$.
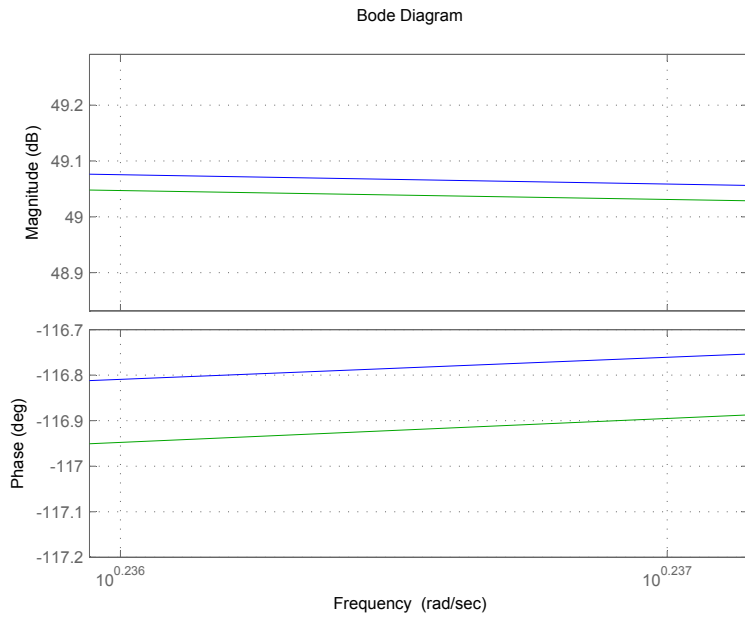

Figure 9.4. Detailed bode plots of dc impedance model of rectifier station.
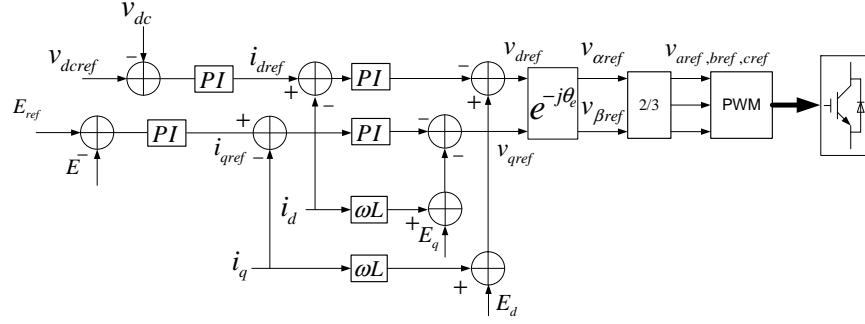
126

Figure 9.5. Controller of the inverter station.

Therefore, the d axis current reference can be expressed as (9.29).

$$i_{d\_ref} = (V_{dc\_ref} - v_{dc})F_{dc}(s) \tag{9.29}$$

Linearizing it yields the expression of Δi_{d_ref}.

$$\Delta i_{d\_ref} = \left[\begin{array}{cc} 0 & 0 \end{array}\right] \left[\begin{array}{c} \Delta i_d \\ \Delta i_q \end{array}\right] + \left[\begin{array}{cc} -F_{dc}(s) & 0 \end{array}\right] \left[\begin{array}{c} \Delta v_{dc} \\ \Delta i_{dc} \end{array}\right] \tag{9.30}$$

Since the inverter station controller also controls ac grid voltage, (9.12) can be used to describe q axis current reference for inverter station. Combining (9.30) and (9.13) yields (9.14), where G_{p1} is the same with (9.15) and the new G_{p2} is shown in (9.31).

$$G_{p2} = \left[\begin{array}{cc} -F_{dc}(s) & 0 \\ -\frac{i_{dc0}F_{ac}(s)}{i_{d0}} & -\frac{v_{dc0}F_{ac}(s)}{i_{d0}} \end{array}\right] \tag{9.31}$$

The inner current controller is identical with rectifier station, hence, the derivation of impedance model for inverter station can be implemented as the approach shown for rectifier station. Therefore, (9.28) can be used to calculate the dc impedance for inverter station as well.

127

9.2 Resonance Analysis

9.2.1 Verification

A two terminal VSC-HVDC system is built in MATLAB/Simulink via SimPowerSystems tool-box. The system parameters and controller settings are shown in Table 9.1, 9.2, and 9.2. In order to verify the derivation of dc impedance models in 9.1, the system was first divided into two isolated parts, which are rectifier station and inverter station. Fig. 9.6 shows the setup of rectifier station verification, where the 250kV dc voltage source is simulating an ideal inverter station, and a constant magnitude variable frequency sinusoidal ac voltage is added to the dc source. The magnitude is set at 5kV which is 2% of the dc source, and the frequency f_{sm} varied from 1Hz to 1000Hz. The dc voltage v_{dc} and current i_{dc} are measured and feed into two discrete Fourier transformation blocks. The dc impedance of rectifier station at certain frequency then can be expressed as $Z_{rec}(f_{sm}) = \frac{V_{dc}(f_{sm})}{I_{dc}(f_{sm})}$. The verification setup in Fig. 9.6 contains a dc capacitor C_{dc}, however, the derivation in 9.1 does not take the capacitor into account. Therefore, the complete dc impedance can be found in (9.32).
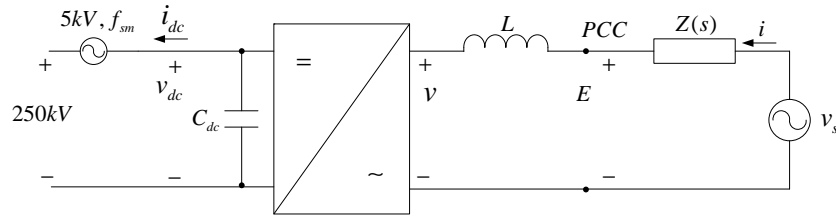
Figure 9.6. Rectifier station verification setup.

$$Z_{rec} = \frac{Z_{dc}}{1 + sC_{dc}Z_{dc}} \tag{9.32}$$

The inverter station verification setup is depicted in Fig. 9.7, where a dc cable is included. Instead of a 250kV dc voltage source, a constant dc current source with 251kV is used to simulate an ideal rectifier station. Based on the dc cable parameters, as long as the inverter station can regulate the dc voltage at 250kV, the active power sent to inverter station is fixed at 100MW. A 5kV variable frequency sinusoidal ac voltage source is added and is used to calculate the dc impedance

128

of inverter station. Since the dc cable is taken into account, the complete dc impedance of inverter station is (9.33).
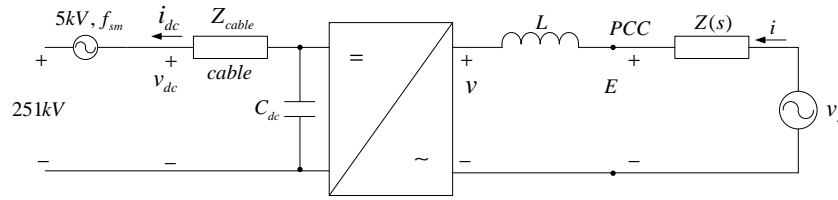

Figure 9.7. Inverter station verification setup.

$$Z_{inv} = \frac{Z_{dc}}{1 + sC_{dc}Z_{dc}} + Z_{cable} \qquad (9.33)$$

Fig. 9.8 shows the verification results of dc impedance for rectifier station. The rectifier station is set to send 100 MW constant active power to the dc voltage source. In Fig. 9.8, the solid trace is the Bode plot of dc impedance of rectifier station computed via (9.32), while the discrete squares are the measured dc impedance of rectifier station shown in Fig. 9.6. For example, we intentionally impose a 5kV sinusoidal voltage source with a frequency of 100Hz on the 250kV dc voltage source. The ripple parts of dc voltage v_{dc} and dc current i_{dc} are measured for analysis. The "Discrete Fourier" block in SimPowerSystems toolbox can be used to extract the magnitude and phase of v_{dc} and i_{dc} at fundamental frequency, which is 100Hz for this example case. Hence, the dc impedance magnitude is then the magnitude ratio of v_{dc} and i_{dc}, and the dc impedance phase is the phase difference between v_{dc} and i_{dc}. For the rectifier station verification simulation in Fig. 9.6, the magnitude ratio of v_{dc} and i_{dc} is -1.2dB, and the phase difference between v_{dc} and i_{dc} is $-91°$. Respectively, for the inverter station verification simulation in Fig. 9.7, the magnitude ratio of v_{dc} and i_{dc} is 29.3dB, and the phase difference between v_{dc} and i_{dc} is $84.3°$ at 100Hz. Other frequencies from 1Hz to 1000Hz are used to verify the dc impedance model in a broad range. The results verify a close match obtained and therefore validate the derivation of dc impedance in Section 9.1. The dc impedance below 1Hz is not measured since lower frequency discrete Fourier transformations become less accurate. The reason is that a large constant dc voltage source is used to simulate the
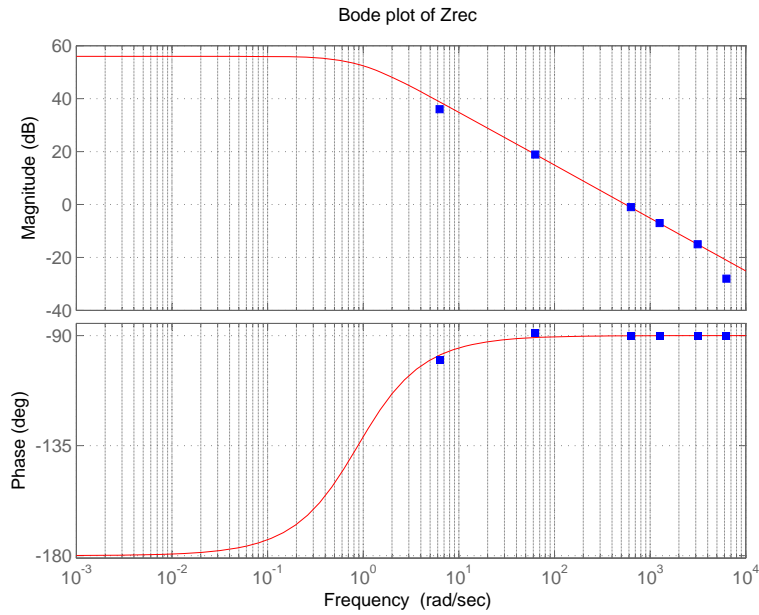
129

Figure 9.8. Bode plot of dc impedance of rectifier station.

inverter station, however, small signals with lower frequencies are not easy to be extracted from the large 250 kV dc voltage.

Fig. 9.9 demonstrates the comparison between computed and measured dc impedances for inverter station. Same with the case for rectifier station, the dc impedances with frequency lower than 1Hz are not measured. However, a reasonable agreement can be found for frequencies from 1Hz to 1000 Hz which validates the inverter dc impedance derivation in Section 9.1 as well.

9.2.2   dc Current Resonance Analysis

9.2.2.1   Impact of dc Capacitor

Once the dc impedances of rectifier and inverter stations are obtained via (9.32) and (9.33), the dc current can be computed as (9.34)

$$i_{dc} = (v_{dc\_rec} - v_{dc\_inv})\frac{Y_{rec}}{1 + Y_{rec}Z_{inv}} \tag{9.34}$$
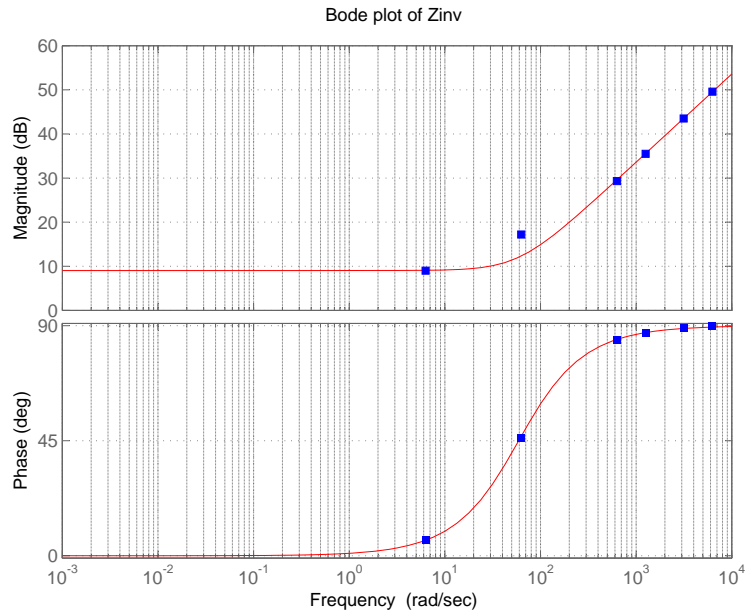
130

Figure 9.9. Bode plot of dc impedance of inverter station.

where v_{dc_rec} and v_{dc_inv} are dc terminal voltages of rectifier and inverter stations respectively. Therefore, investigating the dc impedance item $Y_{rec}Z_{inv}$ can predict dc current characteristics [101, 100, 120].

Fig. 9.10 demonstrates the Nyquist plots of $Y_{rec}Z_{inv}$ with different dc capacitor selections, which indicates the impact of the capacitor size on dc current resonance frequencies. Examining the points where the Nyquist traces crossing the unit circle can indicate the resonance frequencies. For instance, the resonance frequency is 27.7Hz for 900uF capacitor, while the resonance frequencies are 18.8Hz and 12.0Hz for 1800 μF and 3600 μF respectively. Hence, the resonance frequency decreases while the capacitance increases. The phase margin also increases and improve the stability while the capacitance increases. Table 9.4 shows the resonance frequencies and phase margins for different capacitor cases.

A two-terminal VSC-HVDC model is built in RT-LAB real time digital simulator environment. The RT-LAB real-time digital simulator is a high performance computing platform developed by OPAL-RT Technologies, which can simulate power system and power electronics detailed models in real time. Therefore, it can provide precise simulation results and taking the switching details of

131
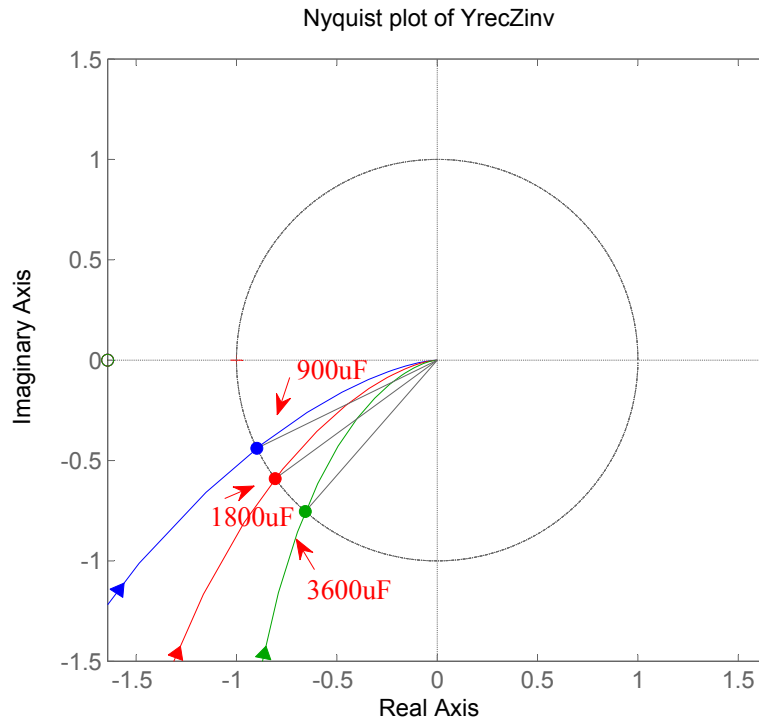
Figure 9.10. Nyquist plots of $Y_{rec}Z_{inv}$.

Table 9.4. Comparison between different capacitor sizes

Capacitance	Resonance frequency (Analysis/Simulation)	Phase margin
900 μF	27.7Hz/28.5Hz	26°
1800 μF	18.8Hz/19.5Hz	36.2°
3600 μF	12.0Hz/14.25Hz	48.9°
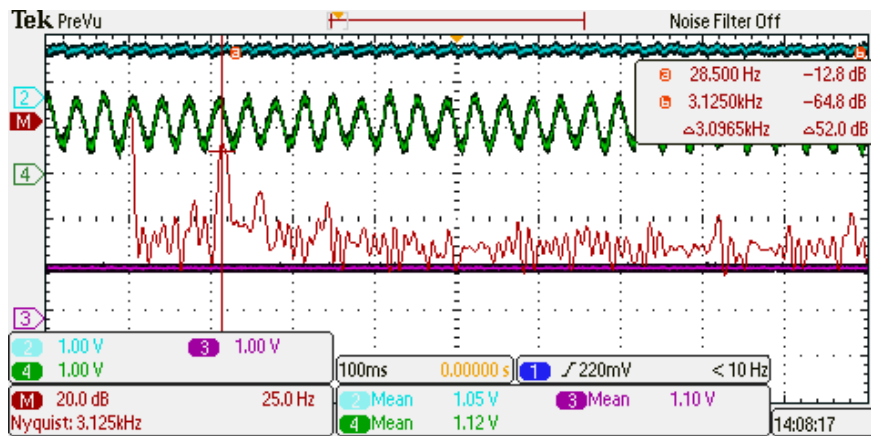
Figure 9.11. Simulation results of $900\mu F$ capacitor.

132
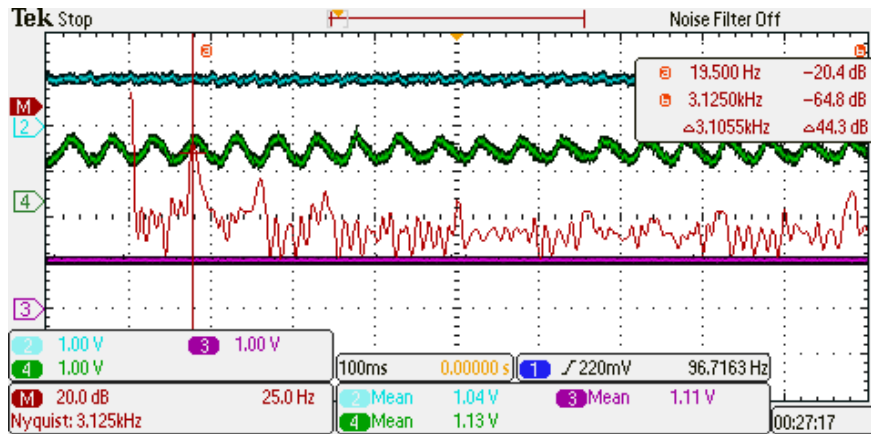
Figure 9.12. Simulation results of $1800\mu F$ capacitor.
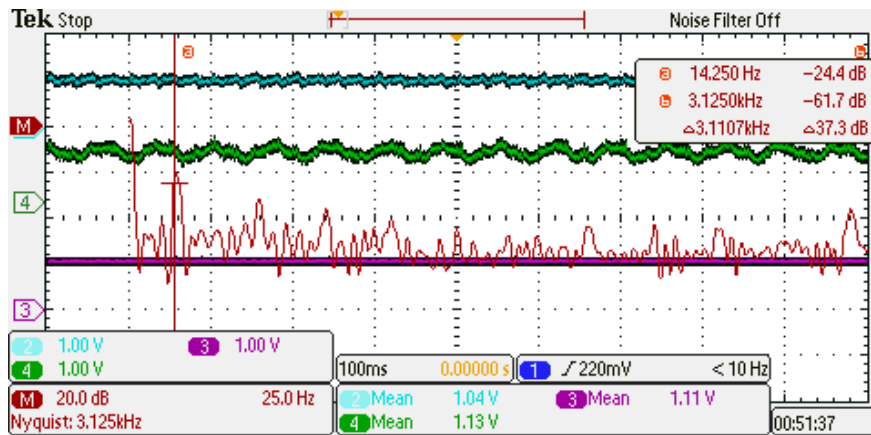
Figure 9.13. Simulation results of $3600\mu F$ capacitor.

Table 9.5. Comparison between different power levels

Power level	Resonance frequency (Analysis/Simulation)	Phase margin
100 MW	18.8 Hz/19.5 Hz	$35.8°$
200 MW	18.8 Hz/20 Hz	$36.2°$
-100 MW	18.8 Hz/19.5 Hz	$37°$

133

Figure 9.14. Nyquist plots of dc current characteristics at different power levels.

Figure 9.15. Simulation results of $1800\mu F$ capacitor at 200 MW.

134
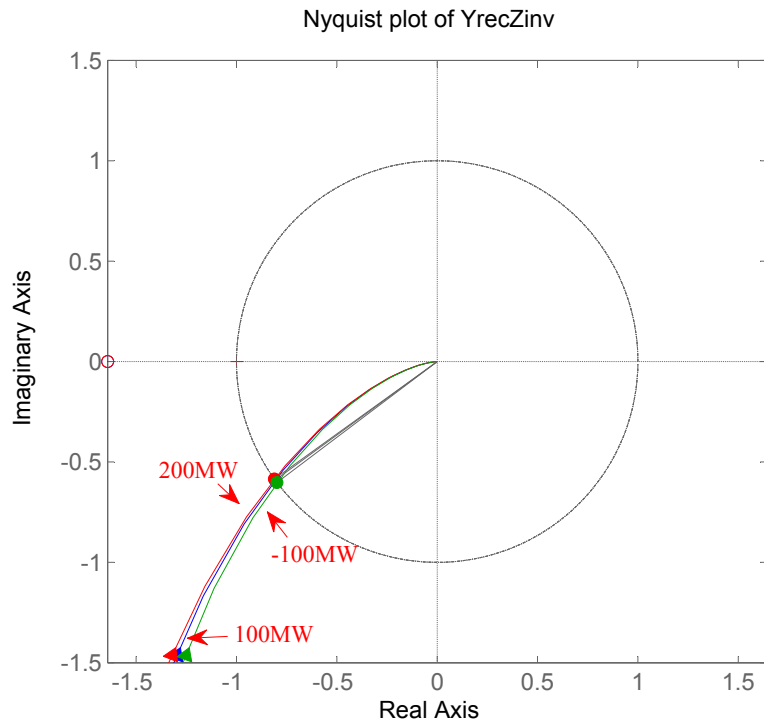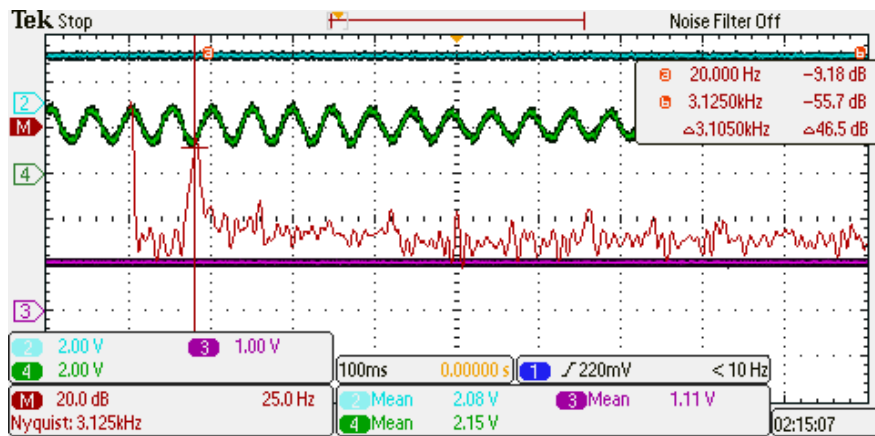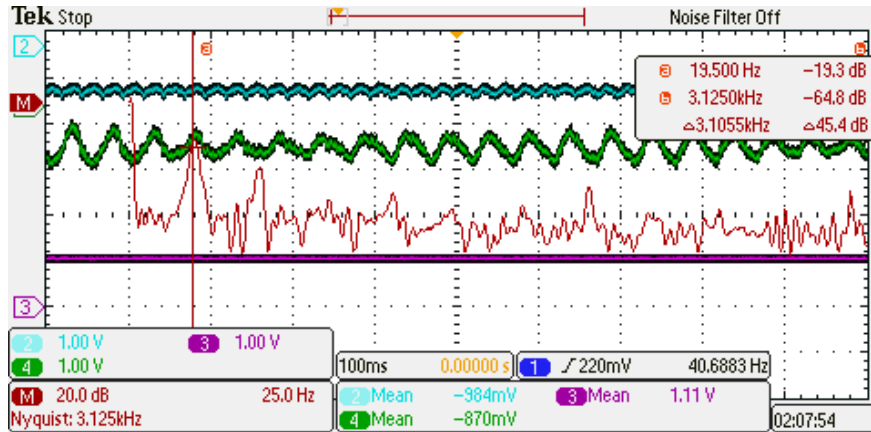
Figure 9.16. Simulation results of $1800\mu F$ capacitor at -100 MW.

IGBTs into account. Moreover, the simulation can run in real time and highly improve simulation efficiency. Fig. 5.10 shows the setup of RT-LAB simulator and its corresponding oscilloscopes which monitor the simulation signals, such as voltage, current and power.

In the simulation model, the rectifier station is set to send 100MW active power to inverter station, and the dc-link voltage is set to 250kV. The dc capacitor varies to examine the dc current resonance and comparing with the analysis results in Fig. 9.10. Fig. 9.11 shows the simulation results for $900\mu F$ capacitor. The cyan trace is the active power sending to inverter station, the mean value of which is 0.672 V. For the measurement system in this simulation, power, voltage and current are measured in per unit system, and are displayed on oscilloscope in Volts. For this case, 1V (1pu) represents 100 MW for power, and it also represents 400 A for current and 250 kV for voltage. Therefore, the cyan trace indicates 1.05 pu active power is sending to inverter station. The purple trace shows the dc-link mean voltage is 1.10 pu and dc mean current is 1.12 pu. The red trace is the FFT analysis of dc current, which shows the highest harmonic is at 28.5 Hz and is very close to 27.7 Hz in Fig. 9.10.

Figs. 9.12 and 9.13 are the simulation results of $1800\mu F$ and $3600\mu F$ cases. The highest harmonics are at 19.5 Hz and 14.25 Hz respectively, and comparing with the analysis in Fig. 9.10, a reasonable agreement can be found. According to Table 9.4, phase margin decreases as capacitor sizes becoming smaller. This phenomenon is demonstrated in current ripple magnitudes. With

135

the size increasing, the current ripple magnitudes found in Figs. 9.11, 9.12, 9.13 decrease. The time-domain simulation results verify the analysis.

9.2.2.2   Impact of Power Level

Fig. 9.14 shows the Nyquist plot of $Y_{rec}Z_{inv}$ at different power levels. The dc capacitor is chosen at $1800\mu F$. Active power transferred to inverter station is tested at 100 MW, 200 MW and -100 MW which means reverse power transfer for this case. The resonance frequency for each power level is almost the same on the Nyquist plot. Table 9.5 shows the resonance frequencies and phase margins for different power levels. Although higher power transfer level makes the phase margin decrease small amount, the impact on dc stability can be neglected.

Fig. 9.15 and 9.16 show the real-time simulation results for 200 MW and -100 MW cases. The FFT analysis of dc current indicates resonance frequencies are 20 Hz and 19.5 Hz, which are very close to the 100 MW case shown in Fig. 9.12.

CHAPTER 10

CONCLUSIONS AND FUTURE WORK

10.1 Conclusions

This dissertation can be concluded in five parts as follows.

First, modeling and control of battery and PV station of a microgrid are presented in Chapters 3 and 4. A battery to improve the microgrid operation such as power flow and autonomous mode is discussed in Chapter 4. A coordinated control strategy between battery and PV station within a microgrid is introduced in Chapter 4.

Second, unbalance and harmonic currents mitigation by the VSC of a battery for microgrid is designed and verified with RT-LAB in chapter 5. The power quality issues have been carefully addressed, and the PR controller has been verified can efficiently remove the negative sequence and harmonic currents.

A novel dc voltage controller design approach is proposed in Chapter 6 and the controller parameters are proved can be precisely obtained based on the performance requirement of the system operator.

The fourth part investigates the Multi-terminal VSC-HVDC operation which includes a four terminal stations. A power droop control scheme is designed to split the active power to two inverter stations based on the droop coefficients. A novel fault control method to limit the dc voltage overshoot is designed and verified in simulation tool.

The fifth part analyzes the VSC-HVDC system based on impedance modeling at both ac and dc side in Chapter 9 and 10. The system structure and controller details are both taken into account when developing the models. The feed-forward filter, ac line length and power level are found to

137

have significant affect on ac side resonance, while the dc side capacitor affects the dc side resonance most.

10.2   Future Work

The future work of this dissertation can contain the following parts.

First, a comprehensive microgrid with different renewable energy resources can be built in RT-LAB for real-time simulation. The PV irradiation profile and wind speed profile can be included into the system for studies on hourly scale. Optimized system power flow and economic operation can be investigated.

Second, the PLL dynamics and system short circuit level can be included in the dc impedance modeling of the VSC-HVDC in Chapter 9. Under weak system scenario, the dc impedance model may have different characteristics so the resonance on dc side may have different properties.

Last, a hybrid VSC-HVDC and LCC-HVDC system can be investigated in RT-LAB environment. Since LCC-HVDC has been deployed into the system several decades ago, the interaction between LCC-HVDC and newly constructed VSC-HVDC will be an interesting research topic.

REFERENCES

[1] A. Yazdani and R. Iravani, *Voltage-sourced converters in power systems : modeling, control, and applications.* Hoboken, N.J. : IEEE Press/John Wiley, 2010.

[2] C. Schauder and H. Mehta, "Vector analysis and control of advanced static var compensators," *Generation, Transmission and Distribution, IEE Proceedings C*, vol. 140, no. 4, pp. 299 –306, jul 1993.

[3] T. Noguchi, H. Tomiki, S. Kondo, and I. Takahashi, "Direct power control of pwm converter without power-source voltage sensors," *Industry Applications, IEEE Transactions on*, vol. 34, no. 3, pp. 473 –479, may/jun 1998.

[4] V. Utkin, "Sliding mode control design principles and applications to electric drives," *Industrial Electronics, IEEE Transactions on*, vol. 40, no. 1, pp. 23 –36, feb 1993.

[5] M. Malinowski, M. Kazmierkowski, S. Hansen, F. Blaabjerg, and G. Marques, "Virtual-flux-based direct power control of three-phase pwm rectifiers," *Industry Applications, IEEE Transactions on*, vol. 37, no. 4, pp. 1019 –1027, jul/aug 2001.

[6] M. Malinowski, M. Jasinski, and M. Kazmierkowski, "Simple direct power control of three-phase pwm rectifier using space-vector modulation (dpc-svm)," *Industrial Electronics, IEEE Transactions on*, vol. 51, no. 2, pp. 447 – 454, april 2004.

[7] R. Datta and V. Ranganathan, "Direct power control of grid-connected wound rotor induction machine without rotor position sensors," *Power Electronics, IEEE Transactions on*, vol. 16, no. 3, pp. 390 –399, may 2001.

[8] D. Zhi and L. Xu, "Direct power control of dfig with constant switching frequency and improved transient performance," *Energy Conversion, IEEE Transactions on*, vol. 22, no. 1, pp. 110 –118, march 2007.

[9] R. Caceres and I. Barbi, "A boost dc-ac converter: analysis, design, and experimentation," *Power Electronics, IEEE Transactions on*, vol. 14, no. 1, pp. 134 –141, jan 1999.

[10] P. Mattavelli, L. Rossetto, G. Spiazzi, and P. Tenti, "General-purpose sliding-mode controller for dc/dc converter applications," in *Power Electronics Specialists Conference, 1993. PESC '93 Record., 24th Annual IEEE*, jun 1993, pp. 609 –615.

[11] K. Jezernik and D. Zadravec, "Sliding mode controller for a single phase inverter," in *Applied Power Electronics Conference and Exposition, 1990. APEC '90, Conference Proceedings 1990., Fifth Annual*, march 1990, pp. 185 –190.

[12] F. Peng, Y. W. Li, and L. Tolbert, "Control and protection of power electronics interfaced distributed generation systems in a customer-driven microgrid," in *Power Energy Society General Meeting, 2009. PES '09. IEEE*, july 2009, pp. 1 –8.

[13] S. Teleke, M. Baran, A. Huang, S. Bhattacharya, and L. Anderson, "Control strategies for battery energy storage for wind farm dispatching," *Energy Conversion, IEEE Transactions on*, vol. 24, no. 3, pp. 725 –732, sept. 2009.

[14] J.-Y. Kim, J.-H. Jeon, S.-K. Kim, C. Cho, J. H. Park, H.-M. Kim, and K.-Y. Nam, "Cooperative control strategy of energy storage system and microsources for stabilizing the microgrid during islanded operation," *Power Electronics, IEEE Transactions on*, vol. 25, no. 12, pp. 3037 –3048, dec. 2010.

[15] N. Hatziargyriou, H. Asano, R. Iravani, and C. Marnay, "Microgrids," *Power and Energy Magazine, IEEE*, vol. 5, no. 4, pp. 78 –94, july-aug. 2007.

[16] N. Hatziargyriou, "microgrids [guest editorial]," *Power and Energy Magazine, IEEE*, vol. 6, no. 3, pp. 26 –29, may-june 2008.

[17] C. Smallwood, "Distributed generation in autonomous and nonautonomous micro grids," in *Rural Electric Power Conference, 2002. 2002 IEEE*, 2002, pp. *D*1 –*D*1_6.

[18] F. Katiraei, M. Iravani, and P. Lehn, "Micro-grid autonomous operation during and subsequent to islanding process," *Power Delivery, IEEE Transactions on*, vol. 20, no. 1, pp. 248 – 257, jan. 2005.

[19] H. Karimi, H. Nikkhajoei, and R. Iravani, "Control of an electronically-coupled distributed resource unit subsequent to an islanding event," *Power Delivery, IEEE Transactions on*, vol. 23, no. 1, pp. 493 –501, jan. 2008.

[20] G. Li, M. Yin, M. Zhou, and C. Zhao, "Modeling of vsc-hvdc and control strategies for supplying both active and passive systems," in *Power Engineering Society General Meeting, 2006. IEEE*, 0-0 2006, p. 6 pp.

[21] H. Chen, "Research on the control strategy of vsc based hvdc system supplying passive network," in *Power Energy Society General Meeting, 2009. PES '09. IEEE*, july 2009, pp. 1 –4.

[22] G. L. Soloveichik, "Battery technologies for large-scale stationary energy storage," *Annual Review of Chemical and Biomolecular Engineering*, vol. 2, no. 1, pp. 503–527, 2011.

[23] M. Bragard, N. Soltau, S. Thomas, and R. De Doncker, "The balance of renewable sources and user demands in grids: Power electronics for modular battery energy storage systems," *Power Electronics, IEEE Transactions on*, vol. 25, no. 12, pp. 3049 –3056, dec. 2010.

[24] S. Vazquez, S. Lukic, E. Galvan, L. Franquelo, and J. Carrasco, "Energy storage systems for transport and grid applications," *Industrial Electronics, IEEE Transactions on*, vol. 57, no. 12, pp. 3881 –3895, dec. 2010.

[25] M. Ceraolo, "New dynamical models of lead-acid batteries," *Power Systems, IEEE Transactions on*, vol. 15, no. 4, pp. 1184 –1190, nov 2000.

[26] M. Chen and G. Rincon-Mora, "Accurate electrical battery model capable of predicting runtime and i-v performance," *Energy Conversion, IEEE Transactions on*, vol. 21, no. 2, pp. 504 – 511, june 2006.

[27] J. Dogger, B. Roossien, and F. Nieuwenhout, "Characterization of li-ion batteries for intelligent management of distributed grid-connected storage," *Energy Conversion, IEEE Transactions on*, vol. 26, no. 1, pp. 256 –263, march 2011.

[28] Y. Riffonneau, S. Bacha, F. Barruel, and S. Ploix, "Optimal power flow management for grid connected pv systems with batteries," *Sustainable Energy, IEEE Transactions on*, vol. 2, no. 3, pp. 309 –320, july 2011.

[29] W. Omran, M. Kazerani, and M. Salama, "Investigation of methods for reduction of power fluctuations generated from large grid-connected photovoltaic systems," *Energy Conversion, IEEE Transactions on*, vol. 26, no. 1, pp. 318 –327, march 2011.

[30] M. Marwali, M. Haili, S. Shahidehpour, and K. Abdul-Rahman, "Short term generation scheduling in photovoltaic-utility grid with battery storage," *Power Systems, IEEE Transactions on*, vol. 13, no. 3, pp. 1057 –1062, aug 1998.

[31] M. Rahman and S. Yamashiro, "Novel distributed power generating system of pv-ecass using solar energy estimation," *Energy Conversion, IEEE Transactions on*, vol. 22, no. 2, pp. 358 –367, june 2007.

[32] N. Kakimoto, H. Satoh, S. Takayama, and K. Nakamura, "Ramp-rate control of photovoltaic generator with electric double-layer capacitor," *Energy Conversion, IEEE Transactions on*, vol. 24, no. 2, pp. 465 –473, june 2009.

[33] N. Kakimoto, S. Takayama, H. Satoh, and K. Nakamura, "Power modulation of photovoltaic generator for frequency control of power system," *Energy Conversion, IEEE Transactions on*, vol. 24, no. 4, pp. 943 –949, dec. 2009.

[34] H. Fujita, T. Yamasaki, and H. Akagi, "A hybrid active filter for damping of harmonic resonance in industrial power systems," *Power Electronics, IEEE Transactions on*, vol. 15, no. 2, pp. 215–222, 2000.

[35] S. Bhattacharya, T. M. Frank, D. Divan, and B. Banerjee, "Active filter system implementation," *Industry Applications Magazine, IEEE*, vol. 4, no. 5, pp. 47–63, 1998.

[36] F. Z. Peng, "Application issues of active power filters," *Industry Applications Magazine, IEEE*, vol. 4, no. 5, pp. 21–30, 1998.

[37] H. Akagi, "New trends in active filters for power conditioning," *Industry Applications, IEEE Transactions on*, vol. 32, no. 6, pp. 1312–1322, 1996.

[38] S. Buso, L. Malesani, and P. Mattavelli, "Comparison of current control techniques for active filter applications," *Industrial Electronics, IEEE Transactions on*, vol. 45, no. 5, pp. 722–729, 1998.

[39] H. Fujita and H. Akagi, "The unified power quality conditioner: the integration of series and shunt-active filters," *Power Electronics, IEEE Transactions on*, vol. 13, no. 2, pp. 315–322, 1998.

[40] F. Blaabjerg, R. Teodorescu, M. Liserre, and A. Timbus, "Overview of control and grid synchronization for distributed power generation systems," *Industrial Electronics, IEEE Transactions on*, vol. 53, no. 5, pp. 1398–1409, 2006.

[41] R. Teodorescu, F. Blaabjerg, U. Borup, and M. Liserre, "A new control structure for grid-connected lcl pv inverters with zero steady-state error and selective harmonic compensation," in *Applied Power Electronics Conference and Exposition, 2004. APEC '04. Nineteenth Annual IEEE*, vol. 1, 2004, pp. 580–586 Vol.1.

[42] A. von Jouanne and B. Banerjee, "Assessment of voltage unbalance," *Power Delivery, IEEE Transactions on*, vol. 16, no. 4, pp. 782–790, 2001.

[43] N. Hingorani, "High-voltage dc transmission: a power electronics workhorse," *Spectrum, IEEE*, vol. 33, no. 4, pp. 63 –72, apr 1996.

[44] ABB, "Xiangjiaba - shanghai ±800 kv uhvdc transmission project," http://www.abb.com/industries/ap/db0003db004333/148bff3c00705c5ac125774900517d9d.aspx.

[45] ——, "Dolwin1," http://www.abb.com/industries/ap/db0003db004333/8b74a5fe4cc03e44c125777c003f3203.aspx.

[46] W. Lu and B.-T. Ooi, "Premium quality power park based on multi-terminal hvdc," *Power Delivery, IEEE Transactions on*, vol. 20, no. 2, pp. 978 – 983, april 2005.

[47] L. Xu, B. Williams, and L. Yao, "Multi-terminal dc transmission systems for connecting large offshore wind farms," in *Power and Energy Society General Meeting - Conversion and Delivery of Electrical Energy in the 21st Century, 2008 IEEE*, july 2008, pp. 1 –7.

[48] D. Jovcic, "Interconnecting offshore wind farms using multiterminal VSC-based HVDC," in *IEEE Power Engineering Society General Meeting*, 2006.

[49] O. Gomis-Bellmunt, A. Egea-Alvarez, A. Junyent-Ferre, J. Liang, J. Ekanayake, and N. Jenkins, "Multiterminal hvdc-vsc for offshore wind power integration," in *Power and Energy Society General Meeting, 2011 IEEE*, july 2011, pp. 1 –6.

[50] W. Lu and B.-T. Ooi, "Dc overvoltage control during loss of converter in multiterminal voltage-source converter-based hvdc (m-vsc-hvdc)," *Power Delivery, IEEE Transactions on*, vol. 18, no. 3, pp. 915 – 920, july 2003.

[51] J. Liang, T. Jing, O. Gomis-Bellmunt, J. Ekanayake, and N. Jenkins, "Operation and control of multiterminal hvdc transmission for offshore wind farms," *IEEE Trans. Power Del.*, vol. 26, no. 4, pp. 2596 –2604, oct. 2011.

[52] V. Blasko and V. Kaura, "A new mathematical model and control of a three-phase ac-dc voltage source converter," *Power Electronics, IEEE Transactions on*, vol. 12, no. 1, pp. 116 –123, jan 1997.

[53] J. Thomas, S. Poullain, and A. Benchaib, "Analysis of a robust dc-bus voltage control system for a vsc transmission scheme," in *AC-DC Power Transmission, 2001. Seventh International Conference on (Conf. Publ. No. 485)*, nov. 2001, pp. 119 – 124.

[54] M. Durrant, H. Werner, and K. Abbott, "Model of a vsc hvdc terminal attached to a weak ac system," in *Control Applications, 2003. CCA 2003. Proceedings of 2003 IEEE Conference on*, vol. 1, june 2003, pp. 178 – 182 vol.1.

[55] Y. Ming, L. Gengyin, L. Guangkai, L. Haifeng, and Z. Ming, "Modeling of vsc-hvdc and its active power control scheme," in *Power System Technology, 2004. PowerCon 2004. 2004 International Conference on*, vol. 2, nov. 2004, pp. 1351 – 1355 Vol.2.

[56] A. Alsseid, D. Jovcic, and A. Starkey, "Small signal modelling and stability analysis of multiterminal vsc-hvdc," in *Power Electronics and Applications (EPE 2011), Proceedings of the 2011-14th European Conference on*, 30 2011-sept. 1 2011, pp. 1 –10.

[57] D. Jovcic, N. Pahalawaththa, and M. Zavahir, "Analytical modelling of hvdc-hvac systems," *Power Delivery, IEEE Transactions on*, vol. 14, no. 2, pp. 506 –511, apr 1999.

[58] C. Ferna andndez, P. Zumel, V. Valdivia, A. Ferna07 andndez Herrero, M. Sanz, A. La07 andzaro, and A. Barrado, "Simple model and experimental identification of a fuel-cell-based power supply oriented to system-level analysis," *Power Electronics, IEEE Transactions on*, vol. 26, no. 7, pp. 1868 –1878, july 2011.

[59] V. Valdivia, A. Barrado, A. Laazaro, P. Zumel, C. Raga, and C. Fernandez, "Simple modeling and identification procedures for 'black-box' behavioral modeling of power converters based on transient response analysis," *Power Electronics, IEEE Transactions on*, vol. 24, no. 12, pp. 2776 –2790, dec. 2009.

[60] V. Valdivia, A. Barrado, A. Lazaro, C. Fernandez, and P. Zumel, "Black-box modeling of dc-dc converters based on transient response analysis and parametric identification methods," in *Applied Power Electronics Conference and Exposition (APEC), 2010 Twenty-Fifth Annual IEEE*, feb. 2010, pp. 1131 –1138.

[61] L. Amedo, R. Burgos, F. Wang, and D. Boroyevich, "Black-box terminal characterization modeling of dc-to-dc converters," in *Applied Power Electronics Conference, APEC 2007 - Twenty Second Annual IEEE*, 25 2007-march 1 2007, pp. 457 –463.

[62] M. Cespedes and J. Sun, "Modeling and mitigation of harmonic resonance between wind turbines and the grid," in *Energy Conversion Congress and Exposition (ECCE), 2011 IEEE*, sept. 2011, pp. 2109 –2116.

[63] L. Harnefors, M. Bongiorno, and S. Lundberg, "Input-admittance calculation and shaping for controlled voltage-source converters," *IEEE Trans. Ind. Electron.*, vol. 54, no. 6, pp. 3323 –3334, Dec. 2007.

[64] L. Zhang, L. Harnefors, and H.-P. Nee, "Power-synchronization control of grid-connected voltage-source converters," *Power Systems, IEEE Transactions on*, vol. 25, no. 2, pp. 809 –820, may 2010.

143

[65] ——, "Interconnection of two very weak ac systems by vsc-hvdc links using power-synchronization control," *Power Systems, IEEE Transactions on*, vol. 26, no. 1, pp. 344 –355, feb. 2011.

[66] L. Xu, Z. Miao, and L. Fan, "Control of a battery system to improve operation of a microgrid," in *Power and Energy Society General Meeting, 2012 IEEE*, July 2012.

[67] "Ieee recommended practice for industrial and commercial power systems analysis," *IEEE Std 399-1997*, p. I, 1998.

[68] R. Pena, J. Clare, and G. Asher, "Doubly fed induction generator using back-to-back pwm converters and its application to variable-speed wind-energy generation," *Electric Power Applications, IEE Proceedings -*, vol. 143, no. 3, pp. 231 –241, may 1996.

[69] P. Piagi and R. Lasseter, "Autonomous control of microgrids," in *Power Engineering Society General Meeting, 2006. IEEE*, 0-0 2006, p. 8 pp.

[70] N. Mohan, T. M. Undeland, and W. P. Robbins, *Power Electronics: Converters, Applications, and Design, 3rd Ed.*   Wiley, 2002.

[71] G. Hernandez-Gonzalez and R. Iravani, "Current injection for active islanding detection of electronically-interfaced distributed resources," *Power Delivery, IEEE Transactions on*, vol. 21, no. 3, pp. 1698 –1705, july 2006.

[72] S.-H. Lee and J.-W. Park, "New islanding detection method for inverter-based distributed generation considering its switching frequency," in *Industry Applications Society Annual Meeting, 2009. IAS 2009. IEEE*, oct. 2009, pp. 1 –8.

[73] L. Xu, Z. Miao, and L. Fan, "Coordinated control of a solar and battery system in a microgrid," in *Transmission and Distribution Conference and Exposition, 2012. T&D. IEEE/PES*, May 2012.

[74] C. Hua, J. Lin, and C. Shen, "Implementation of a dsp-controlled photovoltaic system with peak power tracking," *Industrial Electronics, IEEE Transactions on*, vol. 45, no. 1, pp. 99 –107, feb 1998.

[75] C.-H. Chang, J.-J. Zhu, and H.-L. Tsai, "Model-based performance diagnosis for pv systems," in *SICE Annual Conference 2010, Proceedings of*, aug. 2010, pp. 2139 –2145.

[76] R. Gupta, G. Gupta, D. Kastwar, A. Hussain, and H. Ranjan, "Modeling and design of mppt controller for a pv module using pscad/emtdc," in *Innovative Smart Grid Technologies Conference Europe (ISGT Europe), 2010 IEEE PES*, oct. 2010, pp. 1 –6.

[77] E. Koutroulis, K. Kalaitzakis, and N. Voulgaris, "Development of a microcontroller-based, photovoltaic maximum power point tracking control system," *Power Electronics, IEEE Transactions on*, vol. 16, no. 1, pp. 46 –54, jan 2001.

[78] N. Femia, G. Petrone, G. Spagnuolo, and M. Vitelli, "Optimization of perturb and observe maximum power point tracking method," *Power Electronics, IEEE Transactions on*, vol. 20, no. 4, pp. 963 – 973, july 2005.

[79] T. Esram and P. Chapman, "Comparison of photovoltaic array maximum power point tracking techniques," *Energy Conversion, IEEE Transactions on*, vol. 22, no. 2, pp. 439 –449, june 2007.

[80] Y.-J. Wang, "Analysis of effects of three-phase voltage unbalance on induction motors with emphasis on the angle of the complex voltage unbalance factor," *Energy Conversion, IEEE Transactions on*, vol. 16, no. 3, pp. 270–275, 2001.

[81] P. Pillay, P. Hofmann, and M. Manyage, "Derating of induction motors operating with a combination of unbalanced voltages and over or undervoltages," *Energy Conversion, IEEE Transactions on*, vol. 17, no. 4, pp. 485–491, 2002.

[82] Y. W. Li, D. Vilathgamuwa, and P. C. Loh, "A grid-interfacing power quality compensator for three-phase three-wire microgrid applications," *Power Electronics, IEEE Transactions on*, vol. 21, no. 4, pp. 1021–1031, 2006.

[83] Y. Li, D. Vilathgamuwa, and P. C. Loh, "Microgrid power quality enhancement using a three-phase four-wire grid-interfacing compensator," *Industry Applications, IEEE Transactions on*, vol. 41, no. 6, pp. 1707–1719, 2005.

[84] M. Hojo, Y. Iwase, T. Funabashi, and Y. Ueda, "A method of three-phase balancing in microgrid by photovoltaic generation systems," in *Power Electronics and Motion Control Conference, 2008. EPE-PEMC 2008. 13th*, 2008, pp. 2487–2491.

[85] C. Hochgraf and R. Lasseter, "Statcom controls for operation with unbalanced voltages," *Power Delivery, IEEE Transactions on*, vol. 13, no. 2, pp. 538–544, 1998.

[86] B. Blazic and I. Papic, "Improved d-statcom control for operation with unbalanced currents and voltages," *Power Delivery, IEEE Transactions on*, vol. 21, no. 1, pp. 225–233, 2006.

[87] K. Li, J. Liu, Z. Wang, and B. Wei, "Strategies and operating point optimization of statcom control for voltage unbalance mitigation in three-phase three-wire systems," *Power Delivery, IEEE Transactions on*, vol. 22, no. 1, pp. 413–422, 2007.

[88] Q. Song and W. Liu, "Control of a cascade statcom with star configuration under unbalanced conditions," *Power Electronics, IEEE Transactions on*, vol. 24, no. 1, pp. 45–58, 2009.

[89] G. Escobar, A. Stankovic07, and P. Mattavelli, "An adaptive controller in stationary reference frame for d-statcom in unbalanced operation," *Industrial Electronics, IEEE Transactions on*, vol. 51, no. 2, pp. 401–409, 2004.

[90] A. Leon, J. Mauricio, J. Solsona, and A. Gomez-Exposito, "Software sensor-based statcom control under unbalanced conditions," *Power Delivery, IEEE Transactions on*, vol. 24, no. 3, pp. 1623–1632, 2009.

[91] "Ieee recommended practices and requirements for harmonic control in electrical power systems," *IEEE Std 519-1992*, pp. 1–101, 1993.

[92] N. Flourentzou, V. Agelidis, and G. Demetriades, "VSC-based HVDC power transmission systems: An overview," *IEEE Trans. Power Electron.*, vol. 24, no. 3, pp. 592 –602, Mar. 2009.

[93] K. Eriksson, "Operational experience of hvdc lighttm," in *Seventh International Conference on AC-DC Power Transmission*, Nov. 2001, pp. 205 – 210.

[94] L. Weimers, "Hvdc light: A new technology for a better environment," *IEEE Power Engineering Review*, vol. 18, no. 8, pp. 19 –20, Aug. 1998.

[95] L. Xu, L. Fan, and Z. Miao, "System identification based vsc-hvdc dc voltage controller design," in *North American Power Symposium, 2012 IEEE*, sept. 2012.

[96] ——, "Modeling and simulation of multi-terminal hvdc for wind power delivery," in *Power Electronics and Machines in Wind Applications, 2012. PEMWA 2012. IEEE*, july 2012.

[97] L. Xu, L. Yao, and M. Bazargan, "Dc grid management of a multi-terminal hvdc transmission system for large offshore wind farms," in *Sustainable Power Generation and Supply, 2009. SUPERGEN '09. International Conference on*, 2009, pp. 1–7.

[98] M. Liserre, R. Teodorescu, and F. Blaabjerg, "Stability of photovoltaic and wind turbine grid-connected inverters for a large set of grid impedance values," *IEEE Trans. Power Electron.*, vol. 21, no. 1, pp. 263 – 272, Jan. 2006.

[99] J. Dannehl, C. Wessels, and F. Fuchs, "Limitations of voltage-oriented pi current control of grid-connected PWM rectifiers with LCL filters," *IEEE Trans. Ind. Electron.*, vol. 56, no. 2, pp. 380 –388, Feb. 2009.

[100] M. Cespedes and J. Sun, "Modeling and mitigation of harmonic resonance between wind turbines and the grid," in *IEEE Energy Conversion Congress and Exposition*, Sep. 2011, pp. 2109 –2116.

[101] J. Sun, "Impedance-based stability criterion for grid-connected inverters," *IEEE Trans. Power Electron.*, vol. 26, no. 11, pp. 3075 –3078, Nov. 2011.

[102] S. Casoria, *VSC-Based HVDC Transmission System (Detailed Model)*. Natick, MA: The MathWork, Jan. 2010.

[103] J. Liang, T. Jing, O. Gomis-Bellmunt, J. Ekanayake, and N. Jenkins, "Operation and control of multiterminal hvdc transmission for offshore wind farms," *Power Delivery, IEEE Transactions on*, vol. 26, no. 4, pp. 2596 –2604, oct. 2011.

[104] L. Xu and L. Fan, "Impedance-based resonance analysis in a vsc-hvdc system," *Power Delivery, IEEE Transactions on*, vol. 28, no. 4, pp. 2209–2216, 2013.

[105] MathWorks, "Electrical power systems simulation - simpowersystems - simulink," http://www.mathworks.com/products/simpower/index.html.

[106] L.-A. Dessaint, K. Al-Haddad, H. Le-Huy, G. Sybille, and P. Brunelle, "A power system simulation tool based on simulink," *Industrial Electronics, IEEE Transactions on*, vol. 46, no. 6, pp. 1252–1254, 1999.

[107] M. Faruque, Y. Zhang, and V. Dinavahi, "Detailed modeling of cigre hvdc benchmark system using pscad/emtdc and psb/simulink," *Power Delivery, IEEE Transactions on*, vol. 21, no. 1, pp. 378–387, 2006.

[108] N. Prabhu and K. R. Padiyar, "Investigation of subsynchronous resonance with vsc-based hvdc transmission systems," *Power Delivery, IEEE Transactions on*, vol. 24, no. 1, pp. 433–440, 2009.

[109] A. Moharana and P. Dash, "Input-output linearization and robust sliding-mode controller for the vsc-hvdc transmission link," *Power Delivery, IEEE Transactions on*, vol. 25, no. 3, pp. 1952–1961, 2010.

[110] G. Kalcon, G. Adam, O. Anaya-Lara, S. Lo, and K. Uhlen, "Small-signal stability analysis of multi-terminal vsc-based dc transmission systems," *Power Systems, IEEE Transactions on*, vol. 27, no. 4, pp. 1818–1830, 2012.

[111] A. Tabesh and R. Iravani, "On the application of the complex torque coefficients method to the analysis of torsional dynamics," *IEEE Trans. Energy Convers.*, vol. 20, no. 2, pp. 268–275, Jun. 2005.

[112] L. Fan and Z. Miao, "Nyquist-stability-criterion-based SSR explanation for type-3 wind generators," *IEEE Trans. Energy Convers.*, vol. 17, no. 3, pp. 807–809, Sep. 2012.

[113] Z. Miao, "Impedance-model-based SSR analysis for type 3 wind generator and series-compensated network," *IEEE Trans. Energy Convers.*, vol. 27, no. 4, pp. 984 –991, Dec. 2012.

[114] S. Ogasawara and H. Akagi, "Analysis of variation of neutral point potential in neutral-point-clamped voltage source pwm inverters," in *Industry Applications Society Annual Meeting, 1993., Conference Record of the 1993 IEEE*, 1993, pp. 965–970 vol.2.

[115] M. Saeedifard and R. Iravani, "Dynamic performance of a modular multilevel back-to-back hvdc system," *Power Delivery, IEEE Transactions on*, vol. 25, no. 4, pp. 2903 –2912, oct. 2010.

[116] S. Sudhoff, K. Corzine, S. Glover, H. Hegner, and H. Robey, "Dc link stabilized field oriented control of electric propulsion systems," *IEEE Trans. Energy Convers.*, vol. 13, no. 1, pp. 27–33, Mar. 1998.

[117] X. Liu and A. Forsyth, "Active stabilisation of a PMSM drive system for aerospace applications," in *IEEE Power Electronics Specialists Conference*, Jun. 2008, pp. 283 –289.

[118] O. Wallmark, S. Lundberg, and M. Bongiorno, "Input admittance expressions for field-oriented controlled salient PMSM drives," *IEEE Trans. Power Electron.*, vol. 27, no. 3, pp. 1514 –1520, Mar. 2012.

[119] S. Allebrod, R. Hamerski, and R. Marquardt, "New transformerless, scalable modular multilevel converters for hvdc-transmission," in *Power Electronics Specialists Conference, 2008. PESC 2008. IEEE*, 2008, pp. 174–179.

[120] S. Vesti, T. Suntio, J. A. Oliver, R. Prieto, and J. A. Cobos, "Impedance-based stability and transient-performance assessment applying maximum peak criteria," *IEEE Trans. Power Electron.*, vol. 28, no. 5, pp. 2099 –2104, May 2013.

147

APPENDICES

Appendix A List of Abbreviations

ac   alternate current

CIGRÉ   International Council on Large Electric Systems

D-STATCOM   Distribution Static Compensator

dc   direct current

DERs   Distributed Energy Resources

DFIG   Doubly-Fed Induction Generator

DOD   Depth of Discharge

DPC   Direct Power Control

EMTDC   Electro-Magnetic Transients for DC

FFT   Fast-Fourier Transformation

FPGA   Field-Programmable Gate Array

GSVSC   Grid Side Voltage Source Converter

HC   Harmonic Current

HVDC   High Voltage Direct Current

IEEE   Institute of Electrical and Electronics Engineers

IGBT   Insulated-Gate Bipolar Transistor

KCL   Kirchhoff's Current Law

KVL   Kirchhoff's Voltage Law

LCC   Line-Commutated Converters

149

LCC-HVDC	Line-Commutated Converters based High Voltage Direct Current
MATLAB	Matrix Laboratory
MHVDC	Multi-terminal HVDC
MMC	Modular Multilevel Converter
MPPT	Maximum Power Point Tracking
PCC	Point of Common Coupling
PES	Power and Energy Society
PI	Proportional-Integral
PLL	Phase Lock Loop
PMSM	Permanent-Magnet Synchronous Motor
PQ	Active power/Reactive power
PR	Proportional-Resonant
PSCAD	Power Systems Computer Aided Design
PSPICE	Personal Simulation Program with Integrated Circuit Emphasis
PV	Photovoltaic
PWM	Pulse Width Modulation
RHP	Right-Half-Plane
RL	Resistor-Inductor
RLC	Resistor-Inductor-Capacitor

Appendix A (Continued)

RMS	Root Mean Square
SISO	Single Input Single Output
SIT	System Identification Toolbox
SMC	Sliding Mode Control
SOC	State of Charge
STATCOM	Static Synchronous Compensator
THD	Total Harmonic Distortion
UC	Unbalanced Current
Vf	Voltage/frequency
VSC	Voltage-Source Converters
VSC-HVDC	Voltage-Source Converters based High Voltage Direct Current
WFVSC	Wind Farm side voltage Source Converter

Appendix B Reuse Permissions of Published Papers for Chapters 3, 4, 6, 7, 8

Copyright Clearance Center **RightsLink®**

Home | Account Info | Help

IEEE
Requesting permission to reuse content from an IEEE publication

Title: Control of a battery system to improve operation of a microgrid

Conference Proceedings: Power and Energy Society General Meeting, 2012 IEEE

Author: Ling Xu; Zhixin Miao; Lingling Fan

Publisher: IEEE

Date: 22-26 July 2012

Copyright © 2012, IEEE

Logged in as:
Ling Xu
Account #:
3000702209

LOGOUT

Thesis / Dissertation Reuse

The IEEE does not require individuals working on a thesis to obtain a formal reuse license, however, you may print out this statement to be used as a permission grant:

Requirements to be followed when using any portion (e.g., figure, graph, table, or textual material) of an IEEE copyrighted paper in a thesis:

1) In the case of textual material (e.g., using short quotes or referring to the work within these papers) users must give full credit to the original source (author, paper, publication) followed by the IEEE copyright line © 2011 IEEE.
2) In the case of illustrations or tabular material, we require that the copyright line © [Year of original publication] IEEE appear prominently with each reprinted figure and/or table.
3) If a substantial portion of the original paper is to be used, and if you are not the senior author, also obtain the senior author's approval.

Requirements to be followed when using an entire IEEE copyrighted paper in a thesis:

1) The following IEEE copyright/ credit notice should be placed prominently in the references: © [year of original publication] IEEE. Reprinted, with permission, from [author names, paper title, IEEE publication title, and month/year of publication]
2) Only the accepted version of an IEEE copyrighted paper can be used when posting the paper or your thesis on-line.
3) In placing the thesis on the author's university website, please display the following message in a prominent place on the website: In reference to IEEE copyrighted material which is used with permission in this thesis, the IEEE does not endorse any of [university/educational entity's name goes here]'s products or services. Internal or personal use of this material is permitted. If interested in reprinting/republishing IEEE copyrighted material for advertising or promotional purposes or for creating new collective works for resale or redistribution, please go to http://www.ieee.org/publications_standards/publications/rights/rights_link.html to learn how to obtain a License from RightsLink.

If applicable, University Microfilms and/or ProQuest Library, or the Archives of Canada may supply single copies of the dissertation.

BACK | CLOSE WINDOW

Appendix B (Continued)

RightsLink®

Home   Account Info   Help

IEEE Requesting permission to reuse content from an IEEE publication

Title: Coordinated control of a solar and battery system in a microgrid

Conference Proceedings: Transmission and Distribution Conference and Exposition (T&D), 2012 IEEE PES

Author: Ling Xu; Zhixin Miao; Lingling Fan

Publisher: IEEE

Date: 7-10 May 2012

Copyright © 2012, IEEE

Logged in as:
Ling Xu
Account #:
3000702209

LOGOUT

Thesis / Dissertation Reuse

The IEEE does not require individuals working on a thesis to obtain a formal reuse license, however, you may print out this statement to be used as a permission grant:

Requirements to be followed when using any portion (e.g., figure, graph, table, or textual material) of an IEEE copyrighted paper in a thesis:

1) In the case of textual material (e.g., using short quotes or referring to the work within these papers) users must give full credit to the original source (author, paper, publication) followed by the IEEE copyright line © 2011 IEEE.
2) In the case of illustrations or tabular material, we require that the copyright line © [Year of original publication] IEEE appear prominently with each reprinted figure and/or table.
3) If a substantial portion of the original paper is to be used, and if you are not the senior author, also obtain the senior author's approval.

Requirements to be followed when using an entire IEEE copyrighted paper in a thesis:

1) The following IEEE copyright/ credit notice should be placed prominently in the references: © [year of original publication] IEEE. Reprinted, with permission, from [author names, paper title, IEEE publication title, and month/year of publication]
2) Only the accepted version of an IEEE copyrighted paper can be used when posting the paper or your thesis on-line.
3) In placing the thesis on the author's university website, please display the following message in a prominent place on the website: In reference to IEEE copyrighted material which is used with permission in this thesis, the IEEE does not endorse any of [university/educational entity's name goes here]'s products or services. Internal or personal use of this material is permitted. If interested in reprinting/republishing IEEE copyrighted material for advertising or promotional purposes or for creating new collective works for resale or redistribution, please go to http://www.ieee.org /publications_standards/publications/rights/rights_link.html to learn how to obtain a License from RightsLink.

If applicable, University Microfilms and/or ProQuest Library, or the Archives of Canada may supply single copies of the dissertation.

BACK   CLOSE WINDOW

Appendix B (Continued)

RightsLink®

Title:	System identification based VSC-HVDC DC voltage controller design
Conference Proceedings:	North American Power Symposium (NAPS), 2012
Author:	Ling Xu; Lingling Fan
Publisher:	IEEE
Date:	9-11 Sept. 2012

Copyright © 2012, IEEE

Logged in as:
Ling Xu
Account #:
3000702209

IEEE Requesting permission to reuse content from an IEEE publication

Thesis / Dissertation Reuse

The IEEE does not require individuals working on a thesis to obtain a formal reuse license, however, you may print out this statement to be used as a permission grant:

Requirements to be followed when using any portion (e.g., figure, graph, table, or textual material) of an IEEE copyrighted paper in a thesis:

1) In the case of textual material (e.g., using short quotes or referring to the work within these papers) users must give full credit to the original source (author, paper, publication) followed by the IEEE copyright line © 2011 IEEE.
2) In the case of illustrations or tabular material, we require that the copyright line © [Year of original publication] IEEE appear prominently with each reprinted figure and/or table.
3) If a substantial portion of the original paper is to be used, and if you are not the senior author, also obtain the senior author's approval.

Requirements to be followed when using an entire IEEE copyrighted paper in a thesis:

1) The following IEEE copyright/ credit notice should be placed prominently in the references: © [year of original publication] IEEE. Reprinted, with permission, from [author names, paper title, IEEE publication title, and month/year of publication]
2) Only the accepted version of an IEEE copyrighted paper can be used when posting the paper or your thesis on-line.
3) In placing the thesis on the author's university website, please display the following message in a prominent place on the website: In reference to IEEE copyrighted material which is used with permission in this thesis, the IEEE does not endorse any of [university/educational entity's name goes here]'s products or services. Internal or personal use of this material is permitted. If interested in reprinting/republishing IEEE copyrighted material for advertising or promotional purposes or for creating new collective works for resale or redistribution, please go to http://www.ieee.org/publications_standards/publications/rights/rights_link.html to learn how to obtain a License from RightsLink.

If applicable, University Microfilms and/or ProQuest Library, or the Archives of Canada may supply single copies of the dissertation.

[BACK] [CLOSE WINDOW]

154

Appendix B (Continued)

Appendix B (Continued)

ABOUT THE AUTHOR

Ling Xu was born in 1984 in Wuhan, Hubei, China. He obtained his Bachelor degree in Electrical Engineering from Huazhong University of Science and Technology, Wuhan, China in 2007 and his Master's degree from University of Alabama in 2009. He received his Ph.D. degree in Electrical Engineering from the University of South Florida in December, 2013. His research interests include modeling and control of voltage source converter systems and real-time digital simulation.